Dissertation zur Erlangung des Doktorgrades
der Fakultät für Chemie und Pharmazie
der Ludwig-Maximilians-Universität München

Structural analysis of human UFMylation and ribosome quality control pathways

Ivan Rumenov Penchev

aus

Sofia, Bulgarien

2025

Erklärung

Diese Dissertation wurde im Sinne von §7 der Promotionsordnung vom 28. November 2011 von Prof. Dr. Roland Beckmann betreut.

Eidesstattliche Versicherung

Diese Dissertation wurde eigenständig und ohne unerlaubte Hilfe erarbeitet.

München, September 12, 2025

Ivan Penchev

Dissertation eingereicht am: 16.09.2025
1. Gutachter: Prof. Dr. Roland Beckmann
2. Gutachter: Prof. Dr. Karl-Peter Hopfner
Mündliche Prüfung am: 24.10.2025

Contents

List of Figures

List of Publications

Publication 1

UFM1 E3 ligase promotes recycling of 60S ribosomal subunits from the ER
Paul A. DaRosa†, **Ivan Penchev†**, Samantha C. Gumbin, Francesco Scavone, Magda Wąchalska, Joao A. Paulo, Alban Ordureau, Joshua J. Peter, Yogesh Kulathu, J. Wade Harper, Thomas Becker, Roland Beckmann*, Ron R. Kopito*
Nature. 2024 Mar 14;627(8003):445-52.

Publication 2

UFMylation orchestrates spatiotemporal coordination of RQC at the ER
Ivan Penchev†, Samantha Gumbin†, Francesco Scavone, Otto Berninghausen, Thomas Becker, Ron Kopito*, Roland Beckmann*
Science Advances. 2025 May 2;11(18):eadv0435.

† - authors contributed equally, * - corresponding author(s)

Contribution report

Publication 1: UFM1 E3 ligase promotes recycling of 60S ribosomal subunits from the ER

This work explored the mechanistic role of UFMylation of the 60S ribosomal subunit protein uL24. While uL24 was previously identified as the main target of UFMylation, how UFMylation occurs and what its exact function is was unclear. In addition, the downstream response to UFMylation was unknown. Using proximity labeling, the UFM1 E3 ligase complex itself was identified as a possible "reader" of UFMylation, and its persistent association with 60S subunits was revealed via sucrose gradient centrifugation. Affinity purification of 3xFLAG-tagged UFM1 and UFL1 from HEK293 cells was performed to purify the E3 complex bound to the large subunit, and was complemented by in vitro reconstitution of the UFMylation reaction on 60S. Cryo-EM analysis of these samples revealed the architecture of the 60S-bound trimeric E3, which forms a C-shaped clamp that envelops the 60S from the tRNA binding sites all the way to the ribosome tunnel exit. In addition, sequential states of the UFMylation reaction were identified, thus allowing the construction of a working model for the pathway, in which UFL1 initially binds with its C-terminal region to SEC61-bound 60S subunits, then recruits DDRGK1 and CDK5RAP3. Following assembly, uL24 UFMylation occurs, which positions a large α-helix of DDRGK1 towards the tunnel exit, dislodging the large subunit from the translocon. This showcased UFMylation as a general recycling mechanism of terminated 60S subunits from the translocon. My contribution to this work includes generation of 3xFLAG-UFM1 and 3xFLAG-UFL1 expressing cell lines, affinity purification of UFM1 and UFL1 samples, cryo-EM data analysis, model building of the UFM1 E3 ligase bound to the large ribosomal subunit, as well as preparation of the manuscript and figures.

Publication 2: UFMylation orchestrates spatiotemporal regulation of RQC at the ER

This study focused on the role of UFMylation in RQC at the ER. Following up from the paper described above, the structure of the UFM1 E3 ligase and its function in recycling 60S subunits offered a plausible role of UFMylation in RQC as well. At the same time, the structure posed a logical conundrum, as binding of UFL1 requires the absence of tRNA, whereas the RQC pathway requires a peptidyl-tRNA to initiate binding of NEMF. This left uncertainties in regard to the sequence of events and the method of crosstalk between the two pathways. In order to answer these questions, affinity purification of 3xFLAG-UFL1

from HEK293 cells treated with the translation stall-inducing antibiotic anisomycin was performed. Cryo-EM analysis of this sample unveiled the ER-RQC complex, comprising of the UFMylation and RQC machinery simultaneously bound on a single 60S subunit. This is facilitated by an alternate conformation of UFL1's C-terminal region, which is flipped out the tRNA binding sites and towards the central protuberance to permit simultaneous cohabitation with NEMF and tRNA. Mutational analysis of a stabilizing UFL1-NEMF interaction revealed it as the coordinator between the two proteins, and, by extension, the two pathways. Additional ER-RQC structural states allowed better understanding of the sequence of events, where NEMF-mediated CAT-tailing occurs first, followed by UFMylation, which allows LTN1 to access and ubiquitinate the nascent chain. Biochemical data investigating NEMF and LTN1 association to the 60S in the absence of UFMylation confirmed this order of events, and deUFMylation was additionally revealed to be a prerequisite for efficient nascent chain degradation. My contribution to this work consists of affinity purification of the UFL1 sample, cryo-EM data analysis, model building, manuscript writing and and preparation of figures.

Summary

The vast majority of cellular functions are performed by proteins. Protein synthesis, also known as translation, is carried out by the ribosome. It is imperative that translation be as robust as possible, as incorrectly synthesized proteins could potentially lose their function, gain a new function that could have detrimental effects on the cell, or even form toxic aggregates due to misfolding. All of these outcomes can lead to disease in an organism, which is why translation is monitored by a number of pathways to ensure that it is carried out correctly and that any incorrectly synthesized proteins are disposed of. The ribosome quality control (RQC) pathway is one such failsafe. When ribosomes encounter a "roadblock" during translation, translation stalls. Stalled ribosomes not only halt their own translation, but also that of ribosomes trailing behind them, as those collide with the stalled ribosomes. Stalled ribosomes can be split into small 40S and large 60S ribosomal subunits. The large subunit of a split stalled ribosome still carries a transfer RNA (tRNA) bound to an incomplete nascent chain (a peptidyl-tRNA). This 60S-peptidyl-tRNA complex is recognized by the RQC component NEMF, which in turn recruits the E3 ligase LTN1, which ubiquitinates the nascent chain and targets it for degradation. NEMF is also capable of templateless addition of alanines to the nascent chain, a process also known as CAT-tailing. Following ubiquitination of the nascent chain, the endonuclease ANKZF1 cleaves the tRNA, releasing the nascent chain from the large subunit, allowing for its degradation by the proteasome.

One area of RQC that remains particularly enigmatic is endoplasmic reticulum (ER) specific RQC (ER-RQC). Ribosome stalling at the ER leads to the nascent chain being trapped in the SEC translocon, making it inaccessible for ubiquitination via LTN1. Recent studies on ER-RQC have revealed that the ubiquitin-like modification UFM1 plays an essential role, with UFMylation of the large ribosomal subunit uL24 being necessary for nascent chain degradation. However, the underlying mechanisms remain unclear. The works presented in this thesis focus on ribosome UFMylation and the downstream responses that it elicits. Cryo-EM was used to determine the structure of the trimeric UFM1 E3 ligase ($E3^{UFM1}$), showing that it has a unique role as both "writer" and "reader" of its own modification. Structural snapshots of the UFMylation reaction combined with release assays confirm that the $E3^{UFM1}$ itself serves to disassociate 60S subunits from the SEC translocon as a general recycling mechanism. However, the E3 ligase's initially uncovered binding mode is incompatible with the RQC machinery, as it requires the absence of tRNA, whereas NEMF exclusively recognizes peptidyl-tRNA bound 60S. Structural analysis of

UFMylation under stalling conditions uncovered an alternate binding mode of the $E3^{UFM1}$ component UFL1, in which it can coexist with NEMF on the same 60S, as well as further structural snapshots that showcase the temporal sequence of events in ER-RQC. Taken together, the results showcase UFMylation as a translocon-dissociation mechanism for the large ribosomal subunit, pulling double duty both in traditional termination as well as in ER-RQC via different binding modes of the E3 component UFL1.

Chapter 1

Introduction

1.1 Cryo-electron microscopy

The complexity of biological machineries in combination with their microscopic sizes, which are often below the nanometer range, makes understanding their mechanistic intricacies exceedingly complex, which in turn necessitates methods to solve their three-dimensional structures. While X-ray crystallography has been the go-to method for structural studies of biomolecules for decades, cryo-electron microscopy has been gaining increasing traction, with the last decade having seen a "cryo-EM resolution revolution", elevating the method to new heights in achievable resolution, ease of use, and overall accessibility, making it the tool of choice for the majority of structural research nowadays. Cryo-EM circumvents certain pitfalls of X-ray crystallography, foregoing the need for sample crystallization, requiring much less material, and allowing for analysis of larger, more dynamic, and nonhomogeneous samples, which allows for the sampling of multiple states of a structure in the same dataset.

1.1.1 The electron microscope

Originally, microscopy methods used a light source for imaging. However, the achievable resolution of a conventional light microscope is ultimately limited to a resolution of about 200 nm by the diffraction limit of light (Hon. 1882). Electron microscopes instead use electrons for imaging, which have the advantage of having very short wavelengths, and thus are capable of achieving a higher theoretical resolution limit. Despite this fundamental difference, the electron microscope functions in a similar manner to a light microscope - electrons emitted from a source pass through a condenser lens system that focuses them onto the sample. Electrons interacting with the sample are scattered at different angles and then reach the objective lens, which produces an initial magnified image. An intermediate and projector lens system can then magnify the image further, allowing the system to reach multiple thousand-fold orders of magnification (Orlova and Saibil 2011).

1.1.2 Sample Preparation for EM

While electrons provide a potentially higher resolution compared to light, the electron beam's path must be kept in a vacuum to prevent unwanted scattering by materials other than the sample. This requires that the sample itself be solid. Additionally, biological tissue quickly undergoes radiation damage when continuously exposed to high-energy electrons, necessitating special sample preparation techniques. The go-to techique nowadays is vitrification. As biological material is natively found in an aqueous environment, any treatment that dehydrates the sample can potentially damage it or alter its structure. While low temperatures significantly reduce damage to the sample (Glaeser 1971; Knapek and Dubochet 1980) , freezing under normal conditions would form crystalline ice, which itself is damaging to biological matter and can interfere with measurements. However, if water is cooled rapidly enough, it instead forms a crystal-free solid known as amorphous or vitreous ice. Vitrification of water and aqueous solutions was demonstrated in the early 80s and has since become the standard method for sample preparation of biological matter in high-resolution EM (Dubochet and McDowall 1981; Dubochet et al. 1988).

1.1.3 Image formation in Cryo-EM

Transmission-electron microscopy (TEM), where image formation is achieved by detection of electrons passing through the sample, is the basis of cryo-EM. Electrons passing through the sample can either do so with or without transferring energy (inelastic or elastic scattering, respectively). Inelastic scattering leads to sample damage, which ends up being a limiting factor for high resolution imaging. There are two contributing factors to image contrast in TEM: amplitude and phase contrast.

Amplitude contrast occurs due to the attenuation of amplitude of the electron wave as it passes through the object, where electrons are absorbed or scattered beyond the objective lens. While this can play a large role in the presence of heavy atoms, i.e. for negative-stained samples, biological samples are composed of light atoms and thus only minimally absorb electrons. For this reason, amplitude contrast plays a negligible role in contrast formation. Due to the similar scattering strength of atoms comprising biological matter, the amplitude contrast can be assumed to be constant and described by an amplitude contrast ratio (Zhu et al. 1997).

All scattered electrons also experience a phase shift upon their interaction with the sample compared to unscattered electrons. Interference between scattered and unscattered electrons emerging from the sample is what gives rise to phase contrast. Similar to amplitude contrast, phase contrast also remains rather low for biomolecules. However, phase contrast can be enhanced by measuring at a defocus due to an increase in scattering-induced phase shift (Erickson and Klug 1971; Adrian et al. 1984).

Another limiting factor to contrast can be microscope imperfections such as spherical aberration, which leads to reduced focusing of electrons passing through the objective lens further from its center. Combined with defocus, this leads to corruption of the image due to loss of information in certain points. The effect of defocus and spherical aber-

ration can be quantified in frequency space via the contrast transfer function (CTF), $CTF = sin[(\pi * C_s * \lambda^3 * f^4)/2 - \pi * z * \lambda * f^2]$ where z is the defocus, λ the wavelength, C_s is the spherical aberration, and f the spatial frequency of the object (Wade 1992). The CTF describes the contribution of scattered electrons to the amplitude upon interference with unscattered electrons, which can be positive, zero, or negative in an oscillating manner. As this is phase shift dependent, change of defocus modulates how every frequency contributes towards the image. In practical terms, the CTF describes that low defocus values retain high frequency and thus high resolution information at the cost of low resolution, whereas high defocus sacrifices high resolution details for low resolution data. In order to recover as much of the original information as possible, imaging is done over a range of defocus so as to cover both low and high frequencies. It has been shown that the CTF gets increasingly attenuated at higher frequencies, owing to a multitude of factors, such as beam incoherence and astigmatism, charging effects, and inelastic scattering due to chromatic aberration and thick ice (Henderson 1992), with the cumulative effect being described via an envelope function (Wade 1992). A physical manifestation of the CTF are Thon rings, which can allow the estimation of the information contained in an image (Thon 1966). The Thon rings represent the power spectrum (equivalent to the square of the CTF) of an image and can be used to computationally estimate the CTF parameters, which then allows for recovery of the lost information via deconvolution (Zhu et al. 1997; Mindell and Grigorieff 2003).

It is important to note that the electron beam source as well as the imaging method also contribute to the image quality. Spatial and temporal coherence of the electron beam are prerequisites for high resolution imaging. The field emission gun (FEG) provides the highest degree of coherence compared to alternatives such as tungsten or LaB_6 filaments (Crewe et al. 1968; Zhou and Chiu 1993). While the FEG is now the usual choice for high resolution imaging, tungsten and LaB_6 nevertheless remain in use in lower end microscopes for screening purposes.

The importance of the imaging method is due to a couple of reasons. First, resolution is limited by the pixel size of a detector via the so-called Nyquist frequency, equal to $f_{Nyquist} = 1/2 * pixelsize$, owing to the fact that the shortest detectable wavelength needs to be sampled at least twice. Second, detectors themselves can additionally corrupt the signal, either via introducing instrumentation noise or inaccurately recording certain frequencies. These defects can be described via the Detective Quantum Efficiency (DQE) and Modulation Transfer Function (MTF) respectively, and these two detector properties can be used to estimate a detector's imaging capabilities (McMullan, Faruqi, and Henderson 2016). Historically, TEM data was initially recorded on photographic film, which requires digitization for analysis and is not automatable. Charge-coupled device (CCD) detectors emerged as an alternative to film (Mochel and Mochel 1986), offering immediate access to images without the need of developing and digitizing film, allowing for quicker quality assessment. In spite of this, film usage remained prevalent due to its higher DQE at high electron voltages, and thus higher achievable resolution. A major advance in cryo-EM and a contributing factor to the so-called resolution revolution was the implementation of the direct electron detector (DED). Direct detectors were shown to combine the benefits

of superior MTF and DQE together with higher throughput and automation capabilities (McMullan et al. 2009; Milazzo et al. 2010), and their applicability for cryo-EM was proven soon thereafter (Bammes et al. 2012). The application of direct detectors began to yield higher resolution structures from low amounts of data compared to prior methods (Bai et al. 2013; Li et al. 2013). Nowadays, DEDs allow for resolutions close to 1 Å, where every atom can potentially be resolved separately (Zhang et al. 2020; Yip et al. 2020).

1.1.4 Cryo-EM single particle analysis pipeline

Advances in cryo-electron single particle analysis (SPA) have led to a high degree of automation. Advanced algorithms building upon the basic principles of TEM now allow users to routinely reach resolutions below three Ångstrom. Below is a brief overview of the general steps in a modern SPA image processing pipeline.

Beam induced motion correction and CTF estimation

Averaging methods allow the user to obtain superior singal-to-noise ratio (SNR) compared to analyzing single images by aligning structured features present in multiple images (Markham et al. 1964; Frank, Verschoor, and Boublik 1981). Using modern detectors, a micrograph generally consists of a large number of frames (often referred to as a movie) that can be averaged. However, continued exposure to the electron beam progressively damages the sample. Furthermore, movement caused by the incident electron beam could cause blurring (Brilot et al. 2012). Motion correction techniques compensate for this by weighting the frequencies of individual frames. As beam induced damage increases in later frames, high frequencies in those frames are weighted lower compared to earlier frames, a process known as dose weighting. Motion correction algorithms are typically used on the movie stacks following collection (Zheng et al. 2017), but individual motion of particles can also be corrected in later stages of analysis (Scheres 2014). Motion-corrected micrographs are then used to estimate the CTF based on their power spectrum (Zhu et al. 1997; Rohou and Grigorieff 2015; Zhang 2016). Motion correction and CTF estimation generally require minimal user input aside from setting up parameters based on the instrumentation and collection settings and can thus be performed on the fly during data collection.

Particle picking

Selecting appropriate particles from micrographs is an essential task for achieving high resolution reconstruction down the line. Particle picking was initially a manual process, requiring selection of particles in every micrograph by hand. Manual picking is extremely labor-intensive and user-biased, making it unsuitable for accurate and reproducible data extraction and analysis of increasing volumes of data. This led to the development of picking algorithms that can identify particles automatically given an input reference or via identification of certain features, facilitating automatic picking from larger datasets given

prior knowledge of the particles (Zhu et al. 2004; Tang et al. 2007; Scheres 2015). Fully automated picking algorithms were later developed (Zivanov et al. 2018; Wagner et al. 2019; Bepler et al. 2019; Tegunov and Cramer 2019), making particle picking much more robust. Nevertheless, picking remains a difficult part of processing, and it is common practice to try different picking algorithms to see what yields the best results for a particular dataset or particle type. New algorithms utilizing latest advances in neural networks and deep learning are constantly being developed (Dhakal et al. 2025).

2D classification

Following particle picking, the selected particles are typically averaged in 2D classes, with particles of similar shape and orientation being clustered together. This provides high resolution 2D references, which can be used to filter out potential structural heterogeneity in the sample, as well as eliminate contaminant or false positive junk particles. Popular 2D algorithms are cryoSPARC's stochastic gradient descent (SGD) and RELION's expectation maximization algorithms (Scheres 2012; Punjani et al. 2017).

Ab-initio 3D structure determination

Images collected via TEM are a two-dimensional representation of three-dimensional objects. While this inevitably leads to loss of the object's three-dimensional features, this can be circumvented by collecting images in different orientations, then aligning the orientations in three dimensional space in order to recover the three dimensional structure. A general method for three-dimensional (3D) reconstruction employing the Fourier slice theorem was demonstrated in the late 60s (De Rosier and Klug 1968), which has served as a basis for future 3D reconstruction methods.

Provided that a prior 3D template of a structure is not available, a 3D reconstruction must be done ab initio. This can be an extremely computationally intensive task, as one must consider the orientation of particles in three dimensions as well as their position in the image plane. A solution to this problem is the combination of branch-and-bound and stochastic gradient descent algorithms used by cryoSPARC. The branch and bound algorithm begins with coarse estimation of particle poses, followed by iteratively finer adjustments to more quickly estimate correct orientations, whereas stochastic gradient descent samples random subsets of images in each iteration, allowing to reach a correct structure quicker and be less likely to get stuck in a local minimum compared to traditional gradient descent algorithms (Punjani et al. 2017). .This allows not only efficient ab initio reconstruction, but also heterogenous reconstruction without a reference, which can serve as an extra step in cleaning up junk particles. Neural network-based ab initio reconstruction methods such as cryoDRGN2 are now also gaining momentum, allowing for direct high resolution reconstruction of heterogenous states (Zhong et al. 2021b).

High Resolution refinement

Once a reference has been generated, either ab initio or by using a known structure as input, the structure can be refined up to a high resolution. The refinement process consists of finding the optimal alignment of particles along the reference model. This can be a very difficult and computationally intensive task and is usually the bottleneck in SPA processing. Refinement algorithms generally employ maximum likelihood estimation (MLE) methods, where the parameters of a probability function are optimized to give the most likely result given the data present (Scheres 2012; Sigworth et al. 2010). It is notable that at higher resolutions, higher order CTF aberrations as well as anisotropy can become a limiting factor. These can be corrected after obtaining a high resolution structure, in a process known as CTF refinement (Zivanov, Nakane, and Scheres 2020). The effects of CTF refinement vary on a case to case basis, and can range from marginal to significant improvements in the resolution, but it is generally beneficial to refine CTF parameters when aiming for higher resolutions.
A contentious topic in cryo-EM is the measure of resolution. Whereas in traditional microscopy resolution is defined as the shortest distance at which two separate points can still be distinguished as such, in EM resolution is rather a measure of the highest frequency that provides reliable information, i.e. the information is not overwhelmed by noise (Penczek 2010). Resolution is typically estimated via the Fourier Shell Correlation (FSC), where the dataset is split into two independent reconstructions and a cross-correlation function is calculated between the two. For low frequencies, the cross-correlation is usually close to one, falling off at higher frequencies. The resolution is then given by the frequency where the cross-correlation first falls to a certain cut-off, typically 0.143 (Rosenthal and Henderson 2003). It is important to note that resolution can vary across parts of a 3D reconstruction, which is why algorithms have been developed to estimate local rather than overall resolution (Kucukelbir, Sigworth, and Tagare 2014; Vilas et al. 2018; Vilas et al. 2020). Ultimately, however, resolution remains a subjective topic and manual inspection of a reconstruction and its features is the best way to determine how reliable it is.

3D classification

The resolution of a reconstruction can often suffer due to heterogeneity in the data, either conformational or compositional. While this is tolerable up to an extent, it is inevitably going to affect reconstruction quality at higher resolutions. Furthermore, different structures or different conformations of the same structure within the data can provide additional information in regards to the biological process being studied. It is thus imperative that data is sorted properly. While one can often distinguish between two entirely different molecules at the 2D sorting stage, similar structures or different conformations first become apparent in 3D, making classification at this point an important part of SPA. There exist multitudes of algorithms for 3D classification, such as Relion's 3D classification (Scheres 2016), heterogenous refinement and 3D variability analysis in cryoSPARC (Punjani et al. 2017; Punjani and Fleet 2021), and cryoDRGN (Zhong et al. 2021a). There has

also been a recent focus on analyzing dynamics within one state, with algorithms such as cryoDRGN (Zhong et al. 2021a), 3DFlex (Punjani and Fleet 2023), DynaMIGHT (Schwab et al. 2024), and Zernike3D (Herreros et al. 2023) aiming to estimate dynamics of flexible regions and estimate an improved consensus reconstruction. 3D classification is generally the most user-involved step of processing, with multiple steps and attempts with different algorithms being necessary to get the most out of the data, as there is no "one size fits all" solution.

Model building

Once a final reconstruction has been obtained, a molecular model needs to be produced in order to study molecular interactions. This can be done de novo, but it is very labor-intensive, and it is usually common practice to rather fit a model into the reconstruction, provided one already exists. Otherwise, structure prediction tools based on homology such as Phyre (Kelley and Sternberg 2009) and SwissModel (Schwede et al. 2003) can be used to generate starting models that can then be finalized by the user. Recently, the machine learning algorithm employed by AlphaFold2 (Jumper et al. 2021) has been capable of predicting structures for a large majority of proteins, allowing the use of highly accurate complete initial models and making protein model building significantly less labor-intensive. Efforts are now made to employ similar approaches to nucleic acid modeling (Krishna et al. 2024; Abramson et al. 2024), although these have not been as accurate so far, due to the relative lack of DNA and RNA structures. Another emerging approach to model building is the development of automated algorithms that can identify and build proteins or nucleic acids (Terwilliger et al. 2018; He et al. 2022; Jamali et al. 2024; Su et al. 2024), although their performance is so far limited to high-resolution reconstructions (generally below 3-4 Å). Nevertheless, improvements and newer algorithms are likely to make model building more accessible and significantly less time-intensive.

1.2 Protein translation and the ribosome

Protein synthesis is carried out by ribosomes, cellular components capable of translating messenger RNA (mRNA) into fully functional proteins. The ribosome itself is an RNA-protein complex with a size ranging from between 2 Megadalton (MDa) in bacteria to 3-4 MDa in eukaryotes. Despite the difference in complexity between species, ribosomes share a universally conserved core, consisting of 34 proteins and 3 rRNA species, and have two subunits each, the large subunit (LSU) and the small subunit (SSU). The ribosome and its subunits are also commonly referred to by their sedimentation coefficients in Svedberg (S), with prokaryotic ribosomes having 30S for the SSU, 50S for the LSU, and 70S for the entire ribosome, and eukaryotic ones 40S, 60S, and 80S, respectively. (Melnikov et al. 2012; Wilson and Cate 2012). The ribosomal inventory of higher eukaryotes such as *H. sapiens* extends to four rRNAs and a total of 80 proteins (Anger et al. 2013). Eukaryotic rRNA additionally contains insertions known as expansion segments (ESs), which do not

significantly impact the base ribosomal structure, but rather serve as protrusions in certain regions, which are able to act as platforms for certain ribosome-associated factors. The full function and significance of many ESs have yet to be fully characterized (Hariharan, Ghosh, and Palakodeti 2023).
Similarly to their structure, the base functionality of ribosomes remains conserved between species. The process of protein synthesis is called translation, consisting of four major steps - initiation, elongation, termination, and recycling.

Initiation

The first step of the translation cycle consists of assembling and priming the complete ribosome for translation. This process is governed by a subset of proteins known as initiation factors (IFs). Prokaryotes only require three IFs (reviewed in (Rodnina 2018)), whereas eukaryotic initiation employs around a dozen. Eukaryotic initiation begins with the formation of the ternary complex (TC), consisting of GTP-bound eIF2 and an initiator methionine-tRNA (Met-tRNA$_i$). The TC then forms the so-called 43S pre-initiation complex (PIC) together with the 40S subunit and the factors eIF1, eIF1A, eIF3, and eIF5. The mRNA is brought to the PIC via the cap-binding complex eIF4F, forming the 48S initiation complex (IC). The mRNA is scanned for the start AUG codon, recognition of which leads to a conformational rearrangement and gradual release of initiation factors, culminating in joining with the 60S, a process which is dependent on eIF5B and eIF1A. Comprehensive reviews of the eukaryotic initiation process can be found here: (Merrick and Pavitt 2018; Hashem and Frank 2018; Brito Querido, Díaz-López, and Ramakrishnan 2024).

Elongation

Elongation is a cyclic process during which a complete protein is synthesized from singular amino acids. Following initiation, the Met-tRNA$_i$ is located in the peptidyl-tRNA binding site (P-site). The first step in elongation is decoding, during which aminoacyl-tRNAs (aa-tRNAs) are delivered to the aminoacyl-tRNA binding site (A-site) as a trimeric complex with eEF1A and GTP (Dreher, Uhlenbeck, and Browning 1999). Recognition of the correct tRNA via codon-anticodon pairing triggers GTP hydrolysis by eEF1A, leading to its release from the ribosome (Browne and Proud 2002). The tRNA is then completely accommodated into the A-site, a step accompanied by small rearrangements of the 40S known as rolling (Budkevich et al. 2014). Correct positioning of the A-site tRNA into the peptidyl-transferase center (PTC) enables peptide bond formation, where the amino acid (or nascent chain for subsequent cycles) is transferred from P-site tRNA onto the A-site one. This is followed by rearrangement of the A-and P-site tRNAs into A/P and P/E hybrid conformations, respectively, facilitated by swiveling of the head of the SSU (Ratje et al. 2010). This state is recognized by eEF2, which translocates the hybrid tRNAs to the P and exit (E) sites. Subsequent release of eEF2 leaves the ribosome in a so called POST state, where the next tRNA can bind to the A-site (Moazed and Noller 1989; Ferguson

et al. 2015; Milicevic et al. 2024). Although the main steps of elongation are relatively straightforward and conserved between prokaryotes and eukaryotes, the conformational dynamics in higher species are more complex, featuring a multitude of intermediate states that are an ongoing subject of structural studies (Milicevic et al. 2024; Behrmann et al. 2015; Flis et al. 2018), with an increasing focus on *in-situ* visualization (Hoffmann et al. 2022; Gemmer et al. 2023; Rickgauer et al. 2024; Cheng et al. 2025).

Termination and recycling

The elongation cycle repeats until the ribosome reaches one of three stop codons - UAG, UAA, or UGA. Stop codons are recognized not by a complimentary tRNA anticodon, but instead by a trimeric release factor complex consisting of eRF1, eRF3, and GTP (Zhouravleva et al. 1995; Preis et al. 2014). Recognition of the stop codon by eRF1 leads to eRF3-dependent GTP hydrolysis and subsequent dissociation of eRF3, which then positions a conserved release factor GGQ motif of eRF1 in the PTC, inducing peptide release from the tRNA (Alkalaeva et al. 2006; Matheisl et al. 2015; Brown et al. 2015). The terminated ribosome is then recognized by the recycling factor ABCE1, which binds eRF1 and splits the ribosome into its two subunits (Pisarev et al. 2010; Shoemaker and Green 2011). ABCE1 itself stays on the split SSU, preventing premature LSU reassociation and priming the SSU for another round of initiation, thus closing out the translation cycle (Young et al. 2015; Heuer et al. 2017; Kratzat et al. 2021).

1.2.1 Translational surveillance mechanisms

The correct synthesis of proteins is essential to cellular homeostasis, as incorrectly or incompletely synthesized proteins can lose their functionality, become toxic to the cell, or form aggregates. It is therefore imperative that errors in translation are recognized and taken care of as soon as possible. The ribosome is surveilled by a multitude of pathways that recognize translational defects and resolve them. Translational aberrations can occur due to errors in the mRNA, such as the lack of a stop codon or the presence of a premature one. The former case is recognized by the non-stop decay (NSD) pathway, whereas the latter is handled by nonsense-mediated decay (NMD). Additionally, roadblocks in translation can cause elongation stalling, which, depending on the duration and severity of the stall, can trigger no-go decay (NGD).

Nonense-mediated decay (NMD)

In NMD, premature termination often occurs in the presence of the exon-junction complex (EJC) located downstream of the termination event, which serves as a platform for NMD components Upf2 and Upf3 (Le Hir et al. 2001). On the ribosome, the SMG1-Upf1-eRF1-eRF3 (SURF) complex is formed at the stop codon, and interaction between SURF and Upf2-Upf3-EJC induces SMG1-dependent phosphorylation of Upf1, which in turn triggers downstream events leading to mRNA degradation (Kashima et al. 2006; Chamieh et al.

2008; Huntzinger et al. 2008; Loh, Jonas, and Izaurralde 2013). The protein products of the premature stop codon-containing mRNAs seem to be targeted for degradation in a Upf1-dependent manner, but the exact mechanism of targeting and the machinery involved remains unclear (Kuroha, Tatematsu, and Inada 2009; Udy and Bradley 2022; Inglis et al. 2023).

Non-stop decay (NSD) and no-go decay (NGD)

Although the substrates of NSD and NGD are different, both pathways ultimately converge to elicit similar rescue responses by the quality control machinery. The absence of a stop codon in NSD ultimately leads to a situation where elongation cannot proceed due to the absence of a codon in the A-site. Ribosomes stuck without a codon in the A-site are recognized by Pelota (Dom34 in yeast) and HBS1, which are related to the termination factors eRF1 and eRF3, respectively. Recruitment of ABCE1 by Pelota-HBS1 leads to ribosomal splitting and subsequent mRNA degradation. (Doma and Parker 2006; Pisareva et al. 2011; Tsuboi et al. 2012; Becker et al. 2012; Shao et al. 2016). Stalling in NGD can occur due to mRNA secondary structures, absence of tRNAs, long stretches of rare codons, as well as translation into poly(A) stretches. A stalled ribosome causes a roadblock on the mRNA, leading to the eventual collision of the subsequent ribosome trailing behind. This forms a collided disome, which serves as a signal for triggering the RQC pathway as well as mRNA decay (Simms, Yan, and Zaher 2017). Collisions are recognized by ZNF598 (Hel2 in yeast), an E3 ubiquitin ligase that modifies ribosomal proteins uS10 and eS10 (or uS10 and uS3 in yeast). ZNF598's modification activity is dependent on the ribosomal protein RACK1, which is presumably involved in the formation of an interface on stalled disomes that can then be recognized by ZNF598 (Sundaramoorthy et al. 2017; Matsuo et al. 2017; Juszkiewicz et al. 2018; Garzia et al. 2017; Ikeuchi et al. 2019). K63-polyubiquitination of uS10 leads to the recruitment of the RQC trigger (RQT) complex, consisting of ASCC3, ASCC2, and TRIP4 (Slh1, Cue3, and Rqt4 in yeast), which is responsible for disassembly of the leading stalled ribosome (Matsuo et al. 2017; Hashimoto et al. 2020; Juszkiewicz et al. 2020). Structural insights into the RQT complex in yeast suggest that it exerts a pulling force onto the mRNA, which, in conjunction with a swiveling of the 40S head of the lead ribosome, leads to its destabilization and eventual splitting, as the trailing ribosome is forced to wedge into it (Best et al. 2023).
mRNA degradation in NSD/NGD has been proposed to require endonucleolytic cleavage, followed by exonucleolytic degradation via Xrn1 and the Ski-exosome complex (Doma and Parker 2006; Tsuboi et al. 2012). Cue2 has recently been identified as the yeast endonuclease involved in this process, and it been suggested that it could function as an alternative to Xrn1-mediated decay as opposed to an upstream process (D'Orazio et al. 2019). Other work has instead placed it downstream of RQT-mediated splitting, prior to Xrn1 decay (Tomomatsu et al. 2023). Investigation of the *C.elegans* homolog NONU-1 also suggests partial redundancy, hinting at the presence of other endonucleases involved in the process (Glover et al. 2020). The *H. sapiens* homolog N4BP2 has remained largely unstudied thus far. Overall, translation-dependent mRNA degradation appears to be governed by a

number of potentially redundant mechanisms, with the exact relationship between them remaining to be further elucidated.

1.2.2 Ribosome quality control

While degradation of the aberrant mRNA ensures that no more faulty proteins will be produced from it, it is also necessary to get rid of any product already synthesized. Both NSD and NGD result in ribosome rescue, where, unlike in canonical translational termination, the nascent chain remains bound to the large 60S subunit via the P-site tRNA. This complex is specifically targeted via the RQC pathway, which clears the large subunit by targeting the incomplete nascent chain for degradation (Fig. 1.1).

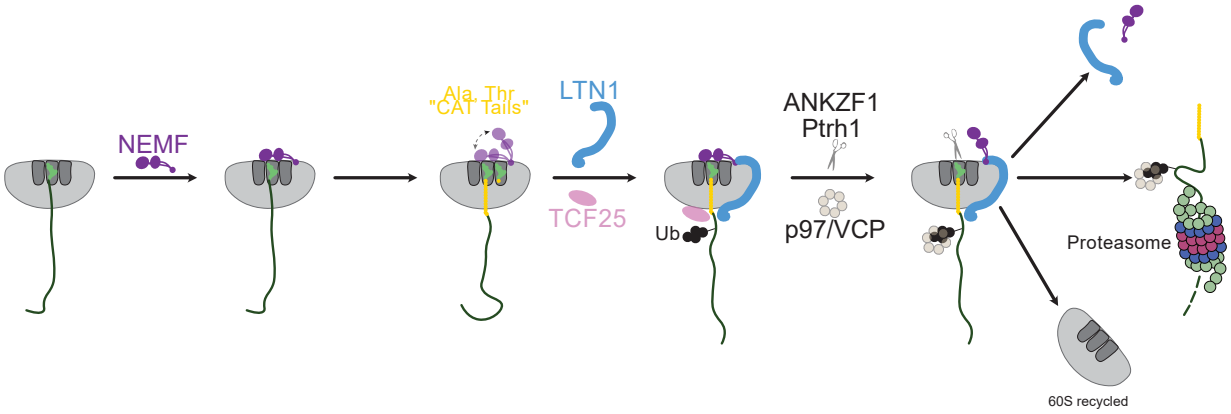

Figure 1.1: Ribosome quality control-mediated nascent chain clearance. Split 60S subunits containing a peptidyl-tRNA are recognized by NEMF/Rqc2, which conducts CAT-tailing. NEMF recruits the E3 ligase LTN1, which ubiquitinates the nascent chain. TCF25/Rqc1 ensures K48-polyubiquitination specificity. tRNA cleavage via ANKZF1 or hydrolysis via Ptrh1 leads to nascent chain release, yielding an empty 60S. The nascent chain is extracted via p97/VCP and degraded by the proteasome.

Initiation of RQC and templateless translation via NEMF

Recognition of P-tRNA-60S complexes and subsequent initiation of RQC is carried out by NEMF. NEMF is a well-conserved protein, having orthologs in both yeast (Rqc2, also known as Tae2) and bacteria (RqcH, also known as FbpA) (Burroughs and Aravind 2014; Filbeck et al. 2022). Initial studies in yeast revealed Rqc2 to be a part of the RQC complex together with Rqc1, Ltn1, and Cdc48, acting as a monitor for translational stress (Brandman et al. 2012; Defenouillère et al. 2013). Structural studies revealed that NEMF/Rqc2 recognize and bind specifically to 60S subunits with exposed tRNA, and that binding is mutually exclusive with 40S subunit binding (Lyumkis et al. 2014; Shen et al. 2015; Shao

et al. 2015). Intriguingly, Rqc2 was shown to additionally be capable of reading tRNA anticodons, specifically alanine and threonine, and extending the nascent chain without the need for an mRNA template or elongation factors, a process dubbed "CAT-tailing" (Shen et al. 2015). Subsequent analyses of RqcH and NEMF revealed a similar templateless translation (TLT) function, albeit specific for alanine only, with the alanine tails themselves being able to act as degrons that signal for the degradation of the nascent chain (Lytvynenko et al. 2019; Thrun et al. 2021). Insights into the templateless translation cycle were obtained via structural investigation of RQC in yeast and bacteria. In both cases, Rqc2/RqcH were shown to conduct TLT beginning with initiation occurring on P-tRNA-60S, followed by delivery of tRNA to the A-site, peptide bond transfer to the A-site tRNA, translocation of the P-site tRNA to the E-site and subsequent release, followed by translocation of the A-site tRNA into the P-site. In addition, peptidyl-transfer in yeast depends on the initiation factor eIF5a, whereas in bacteria the factor RqcP appears to promote A to P-site tRNA translocation by stabilizing the P-site-bound conformation (Crowe-McAuliffe et al. 2021; Tesina et al. 2023). Anticodon selection in yeast was shown to be governed by Rqc2's NFACT-N binding pocket. It selects for a pyrimidine at position 36, due to steric constraints excluding purine accommodation, and has a strict preference for a G in position 35, governed by specific hydrogen bonding with D98 and R99 of Rqc2. These constraints correspond to alanine and threonine anticodons (Tesina et al. 2023). How TLT is carried out and how alanine is specifically selected for NEMF in humans is yet unclear. Termination of TLT also remains somewhat nebulous. Release of tRNA from 60S has been shown to be governed by the endonuclease ANKZF1 (Vms1 in yeast) and tRNA hydrolase Ptrh1 (Izawa et al. 2017; Kuroha et al. 2018; Verma et al. 2018; Zurita Rendón et al. 2018), but what signals for TLT to end and the tRNA to then be released is unclear.

LTN1-mediated nascent chain ubiquitination

Aside from mediating templateless translation, NEMF/Rqc2 also recruit the E3 ubiquitin ligase LTN1/Listerin (Ltn1 in yeast). Initially identified in yeast as a regulator of protein levels of non-stop mRNA reporters and in mice as genetically linked to neurodegenereration (Wilson, Meaux, and Van Hoof 2007; Chu et al. 2009), Ltn1 was later shown to ubiquitinate non-stop nascent chains following ribosomal stalling (Bengtson and Joazeiro 2010), before its identification as a component of the aforementioned RQC complex (Brandman et al. 2012; Defenouillère et al. 2013). *In vitro* analysis of LTN1's activity showed its explicit preference for tRNA-NC-60S complexes, with binding occuring preferentially on nascent chain-bound 60S but not empty 60S, and ubiquitination activity preferentially targeting stalled 60S but not unsplit 80S (Shao, Malsburg, and Hegde 2013). While LTN1 can associate with the 60S subunit on its own, this association is competing with 40S reassociation. However, binding of NEMF prevents reassociation and stabilizes LTN1 on the 60S, serving to recruit it to stalled large subunits (Shao et al. 2015). LTN1's base structure is mostly conserved between human and yeast, consisting of an N-terminal domain that interacts with NEMF/Rqc2's M domain at the sarcin-ricin loop (SRL) of the ribosome, followed by a sequence of flexible HEAT repeats, an RWD domain that further stabilizes the ribosomal

interaction, and the C-terminal catalytic RING domain, which is poised at the ribosome tunnel exit, allowing it to modify the exiting nascent chain (Shen et al. 2015; Tesina et al. 2023; Shao, Malsburg, and Hegde 2013). Since ubiquitination almost exclusively modifies lysines, in the absence of an easily accessible lysine for LTN1, TLT via NEMF allows the nascent chain to be pushed out further to expose a suitable one (Kostova et al. 2017). As such, NEMF and LTN1 work in concert to ensure efficient degradation of nascent chains arising from stalled ribosomes via a combination of templateless translation and nascent chain ubiquitination.
Less is known about the third component of the RQC complex, Rqc1 (TCF25 in humans). Despite being used as bait in yeast structural studies, Rqc1 was not visualized together with the remaining components (Shen et al. 2015; Tesina et al. 2023). Together with Ltn1, Rqc1 is required for recruitment of Cdc48 (p97/VCP in human) (Defenouillère et al. 2016), which extracts the nascent chain and sends it to the proteasome for degradation (Verma et al. 2013). *In vitro* data on the human Rqc1 homolog TCF25 suggests that it is important for K48-specific polyubiquitination of the nascent chain (Kuroha et al. 2018).

1.2.3 Ribosome quality control at the endoplasmic reticulum

While the last decade has shed light on RQC, the main focus has been on translation in the cytosol, where the nascent chain is freely accessible to tunnel exit-binding proteins, which includes LTN1 and TCF25/Rqc1. However, ribosomes targeted to the endoplasmic reticulum (ER) have their nascent chains sequestered by the Sec61 translocon complex during translation-coupled ER-translocation (reviewed in (Itskanov and Park 2023)). This raises the question whether RQC surveys ER-translation, and, if so, how this occurs, or whether a separate pathway disposes of stall-derived nascent chains. *In vitro* analysis of LTN1's activity suggested that it is capable of targeting ER-inserted nascent chains, but the exact conditions for this to occur remained unclear, as access to the nascent chain via LTN1's RING domain would require partial backsliding out of the translocon (Malsburg, Shao, and Hegde 2015). A separate pathway, UFMylation, was later implicated in ER protein degradation and subsequently uncovered to function in tandem with the RQC complex in ER-specific stalling.

UFMylation and its role in ER-RQC

Ubiquitin-like proteins (UBLs) have a similar size and β-grasp fold to that of ubiquitin, albeit with an often divergent amino-acid sequence. As with ubiquitin, proteins are modified via a cascade of activating (E1), conjugating (E2), and ligating (E3) enzymes, with the distinction that while ubiquitin has a vast array of modification targets and E2-E3 proteins, UBLs tend to have more specific modification targets and a smaller group of enzymes in their respective pathway (Veen and Ploegh 2012). Ubiquitin-fold modifier 1 (UFM1) is a UBL initially discovered in human cells together with its E1 protein Uba5 and it's E2 Ufc1. The UFMylation system was found to be present in most eukaryotes with the exception of yeast (Komatsu et al. 2004). The deconjugating proteases UFSP1 and UFSP2

were discovered shortly thereafter (Kang et al. 2007), as well as the E3 ligase UFL1 which peculiarly lacked a RING or HECT domain that is present in ubiquitin E3 ligases. In addition, two proteins, DDRGK1 (also known as UFBP1) and CDK5RAP3 (also known as LZAP), were implicated in forming a complex together with UFL1, with DDRGK1 being tethered to the ER via its N-terminus, leading to ER-specific accumulation of the UFL1-CDK5RAP3-DDRGK1 complex (Tatsumi et al. 2010; Wu et al. 2010; Kwon et al. 2010). UFMylation is linked to a number of diseases, including but not limited to heart conditions (Azfer et al. 2006), cancer (Kwon et al. 2010), and neuropathies (Martin et al. 2015; Hamilton et al. 2017), but its cellular role remained elusive until two independent studies identified uL24 (also known as RPL26) to be the main modification target (Walczak et al. 2019; Wang et al. 2020). UFMylation was linked to the C-terminal region of uL24, which is conserved in higher eukaryotes but not in yeast, specifically K132 and K134. In addition, the trigger for UFMylation was shown to be translocation-associated ribosome stalling, leading to a quality control mechanism that degrades ER-stalled proteins independent of ER-associated protein decay (ERAD). The exact degradation pathway remains a matter of debate, with evidence both for and against lysosomal degradation, and an increasingly large link between UFMylation and the RQC pathway (Wang et al. 2020; Scavone et al. 2023). UFMylation has been shown to be necessary for ER-RQC, specifically for degradation of arrested peptides, but not templateless translation (Scavone et al. 2023). Recent analysis of UFL1's activity has also revealed that it is not capable of efficient ligation activity on its own, but rather forms an active E3 complex upon interaction with DDRGK1 via both proteins' pseudo-winged helix (pWH) domains, which promotes aminolysis of UFM1-bound UFC1, similarily to RING E3 ligases. Together with UFSP2's association with the membrane-tethered protein ODR4 (Walczak et al. 2019), this finding restricts the UFMylation cycle strictly to the ER. At the same time, CDK5RAP3 was shown to not be necessary for UFMylation, instead leading to reduced di- and tri-UFMylation without affecting mono-UFMylation, suggesting that it plays a regulatory role instead (Peter et al. 2022).

Chapter 2

Aims of this thesis

Understanding of the RQC system in the last decade has relied on multiple structural snapshots (Shen et al. 2015; Shao et al. 2015; Tesina et al. 2023). However, the overwhelming focus has been on elucidating the cytosolic mechanism and less so the endoplasmic reticulum-associated one. Thus, much less is known about ER-RQC compared to its cytosolic counterpart. Although UFMylation of uL24 was suggested to play an important role in this process (Walczak et al. 2019; Wang et al. 2020; Scavone et al. 2023), there have been no reported structures of the $E3^{UFM1}$ ligase (either on or off the ribosome) or uL24-bound UFM1 thus far. This gap in knowledge has presented a roadblock in unraveling how this modification can play a role in ER stress and stalled protein degradation. Furthermore, the direct downstream reader of UFMylation remains enigmatic, despite an increasing amount of research focused on delineating the pathway. Understanding how and when the ribosome is UFMylated as well as how and what response UFMylation signals for would close a significant gap in understanding the role of this modification. Similarly to previous studies on cytosolic RQC, cryo-EM once again presents itself as a powerful tool for to answering these questions, providing the opportunity to not only visualize UFMylation of the 60S subunit, but to also capture states prior to or following modification, thus gaining insight into the $E3^{UFM1}$ ligase's activity and potential downstream readers of the modification.

Chapter 3

Discussion

Consistent with its position at the core of protein biogenesis, the ribosome is a target of multiple regulatory pathways that govern protein homeostasis. Monitoring the translation cycle allows the cell to swiftly catch any aberrations, which in turn allows it to respond promptly. RQC is one of the central responders to ribosome stalling, targeting incomplete proteins for degradation. As previously outlined, this work focused on investigating the role of UFMylation at the ribosome and its relation to RQC at the endoplasmic reticulum. The results present the first structural characterization of the trimeric $E3^{UFM1}$ complex bound to the ribosome, as well as mechanistic details of UFMylation's role in ribosome recycling in canonical translation and ribosome rescue upon stalling. This sheds light on the cellular context of the pathway while simultaneously raising new questions with regard to its relationship to certain processes, as outlined below.

UFMylation as a translocon detachment pathway for 60S subunits

A central question this work set out to answer was what the precise role of UFMylation of 60S subunits is. Prior data primarily associated this modification with ER-related quality control pathways, with a large focus on ER-RQC in particular. The first study presented in this work revealed that the $E3^{UFM1}$ ligase plays a dual role as both "writer" and "reader" of its own modification, a somewhat unique feature amongst ubiquitin-like modifications. Furthermore, it was revealed that the pathway plays a more general role than initially thought, functioning in recycling of translocon-bound 60S subunits from the ER. This incidentally answers a decades-old question as to how the ribosome is released from the translocon. Ribosomes were already shown to associate with the endoplasmic reticulum upon their discovery (Palade 1955). The signal hypothesis explained how specific peptides are cotranslationally targeted to the ER while still being synthesized in the cytosol (Blobel and Sabatini 1971). The large subunit was characterized as the ER-binding component long before the characterization of the translocon (Sabatini, Tashiro, and Palade 1966), with the ribosome-membrane interaction having a close to nanomolar affinity (Borgese et al. 1974). Up to this point, however, there has been no clear answer to how this interaction is disrupted upon finishing translocation and termination of ER-associated translation, de-

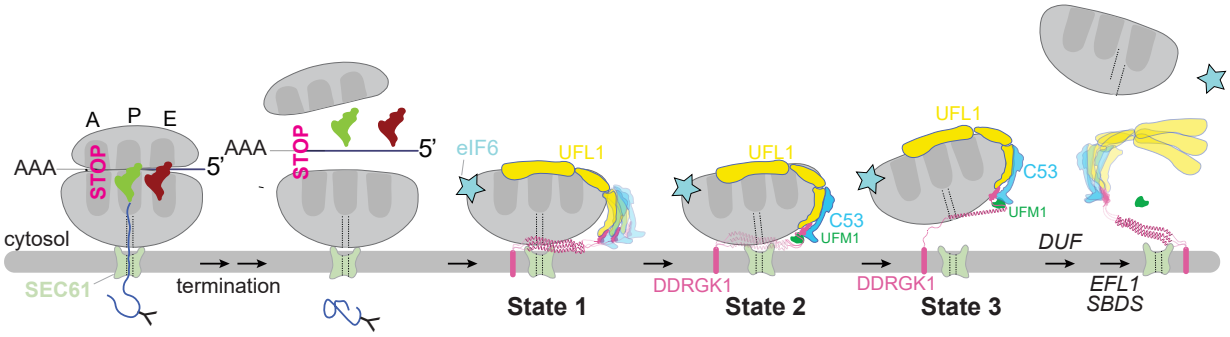

Figure 3.1: Molecular model for UFMylation-dependent 60S subunit recycling. Following termination, the empty translocon-bound 60S subunit is recognized via UFL1, which in turns recruits DDRGK1 and CDK5RAP3. uL24 UFMylation and positioning of DDRGK1 leads to translocon detachment. DeUFMylation releases the 60S from the $E3^{UFM1}$ complex, allowing downstream processes to take place. Image adapted from (DaRosa et al. 2024).

spite a release factor having been proposed to exist almost fifty years ago (Blobel 1976). As such, UFMylation presents itself to be the first known bona fide ER-specific ribosome recycling pathway, with formation of the stable 60S-$E3^{UFM1}$ complex driving translocon dissociation (Fig 3.1). DeUFMylation then governs cytosolic release of the 60S, allowing EFL1 and SBDS to prepare it for 80S reassembly by evicting eIF6 (Weis et al. 2015).

Nevertheless, it does not appear that UFMylation is the end-all be-all of ribosome recycling at the ER. Although UFMylation stimulates translocon dissociation, loss of the pathway does not completely abrogate the release of 60S subunits. This suggests that a parallel pathway could exist, providing a degree of redundancy. This is underscored by the absence of UFMylation in yeast, where this parallel pathway could play a primary role instead. Thus, an open question remains as to what this pathway could be.

UFMylation in ER-RQC

The characterization of the structure and function of the UFMylation machinery provides a plausible role for the pathway in ER-RQC: exposing the translocon-inserted nascent chain via 60S-Sec61 dissociation. This observation initially presented a conundrum, as the binding sites of the $E3^{UFM1}$ ligase and P-tRNA/NEMF would be incompatible on the same ribosome. This was reconciled by the discovery of the alternate conformation of UFL1, which is observed in the double E3 ER-RQC complex. The direct interaction between NEMF's NFACT-C and UFL1's loop domains showcases how the two machineries crosstalk with each other, and the additional states provide a plausible model for the sequence of events, beginning with CAT-tailing, followed by UFMylation that allows nascent chain ubiquitination by LTN1, and culminating in deUFMylation-dependent release from the ER (Fig 3.2).

Despite the extensive characterization of the UFL1-NEMF interaction and its significance, a second direct interaction, occurring between UFL1's CTD and a part of NEMF's

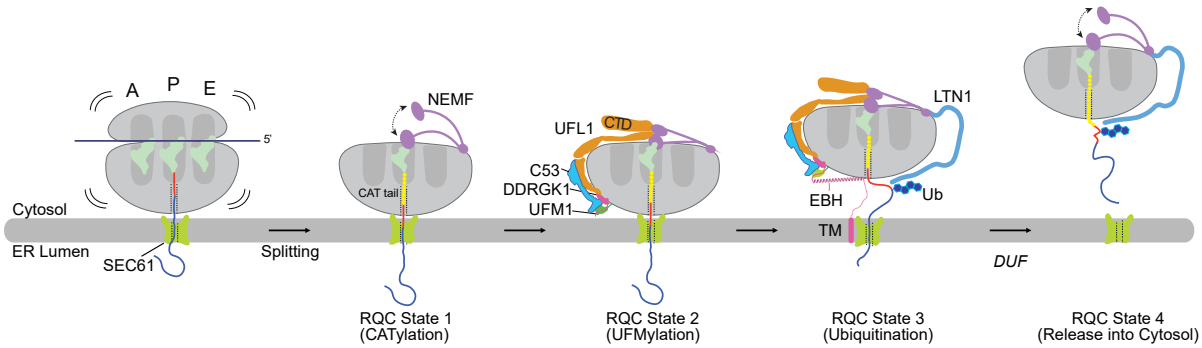

Figure 3.2: Molecular model for ER-RQC. Following splitting, stalled 60S RNCs are recognized by NEMF, which conducts CAT-tailing. This is followed by binding of the $E3^{UFM1}$ ligase and UFMylation of uL24, which exposes the nascent chain, allowing for LTN1 binding and ubiquitination. DeUFMylation releases the 60S-RQC complex into the cytosol. Adapted from (Penchev et al. 2025).

unstructured region (labeled as the CTD interacting motif, CIM), remains unexplored. As this region of NEMF has not been visualized under other conditions, it is tempting to speculate that it could act in recruiting the UFMylation machinery to stalled 60S. As UFL1 appears to be the first binder of the $E3^{UFM1}$ complex to both empty and ER-RQC 60S, it could very well be dependent on recruitment in some manner. While the NEMF CIM may serve to recruit it in its ER-RQC compatible conformation, the UFL1 PTC loop, which cannot bind in the presence of a P-tRNA, could possibly engage in the recycling conformation. The PTC loop plays an important role in UFMylation, with its deletion leading to reduced levels of uL24-UFM1, although to what extent this applies for both recycling and ER-RQC remains to be established. It would be interesting to see how loss of the CIM could affect UFMylation, and whether loss of both the PTC and CIM has a compounding effect. It is worth noting that constitutive loss of NEMF did not appear to hamper UFMylation in cells. In fact, there was an overall increase that could be a compensatory adaptation. A possible further avenue of research would be to test how expression levels of the UFMylation machinery are affected by loss of RQC and whether loss of the CIM leads to a similar response. Overall, while the cooperation between the two pathways is now clear, the intricacies appear to be more elaborate and would require some further exploration.

Interplay between UFMylation and membrane protein biogenesis machinery

The recent discovery and structural characterization of the multi-pass translocon (MPT) also raises the question of how ER-RQC would function for stalled multi-pass peptides (McGilvray et al. 2020; Sundaram et al. 2022; Smalinskaitė et al. 2022). While UFMylation of uL24 seems possible in the presence of the MPT from a structural point of view, DDRGK1 clashes severely both with components of the MPT and the nascent chain itself,

which could prevent UFMylation's dislodging activity. A deciding factor for whether or not UFMylation-dependent dissociation is possible in this case could be the positioning mechanism of DDRGK1. If the helix is slipped straight towards the ribosome tunnel exit and in the process pushes SEC61 away, then the presence of the MPT would likely prevent this from occurring. On the other hand, if positioning occurs with a ratcheting mechanism instead, where DDRGK1's long helix serves as a lever which pulls the ribosome away from the ER prior to positioning itself, this would not be hampered by the presence of the aforementioned proteins.

In a similar fashion, UFMylation appears to be incompatible with the presence of the olygosaccharyltransferase (OST) complex. As such, it would be important to determine how stalled peptides would be targeted in the presence of OST, whether UFMylation plays a role, or whether an alternate pathway takes care of such stalls. Previous studies have found that SEC61 can be found both on its own and together with OST in microsomes, but it was unclear whether these are two separate populations or whether OST association is transient (Pfeffer et al. 2014). If the former is true, OST's presence could dictate if UFMylation or another pathway takes over ribosome dissociation. Cryo-electron tomography analysis of translation at the ER previously identified a large portion of translocons as either OST or MPT-bound, with the core translocon appearing to be a rather small population in comparison (around 10%) (Gemmer et al. 2023). However, at least in the context of multi-pass protein biogenesis, OST appears to transiently bind only when glycosylation is necessary, which would support the latter case (Sundaram et al. 2022). Assuming a model where translocon-associated complexes bind transiently, it is likely that the accessory proteins eventually dissociate from SEC61, allowing UFMylation to occur. It is worth nothing that the tomography study focused on active translation, where OST and MPT would play active roles in translocation, which would explain their strong translocon association, whereas upon termination or splitting they could be dissociated. Measuring kinetics and binding affinities of the various translocon-associated complexes as well as that of the $E3^{UFM1}$ ligase could provide an answer to many of these questions. It would also be interesting to investigate the 60S-$E3^{UFM1}$ complex *in situ* in order to determine what translocon compositions allow it to bind, modify, and dissociate 60S subunits.

The relationship between UFMylation and ER stress, ER-phagy, and the unfolded protein response

A long-known hallmark of defects in UFMylation has been increased ER stress and activation of the unfolded protein response (UPR) (Cai et al. 2015; Lemaire et al. 2011; Zhang et al. 2012). The underlying mechanism behind this response, however, remained unclear until the delineation of the $E3^{UFM1}$ ligase's function. Based on the discoveries around UFMylation's role in ER-RQC, the pathway can now be positioned as a sort of "first responder" in translation-associated ER stress, assisting in the removal of incomplete nascent chains before they can be released into the lumen. Keeping faulty proteins from ending up in the ER would prevent UPR signaling, keeping downstream stress responses in check. This would contrast UFMylation with ERAD, which instead monitors proteins

already sent to the ER (Hwang and Qi 2018), thus creating a level of redundancy in ER protein quality control - UFMylation prevents release of stall-derived nascent chains into the ER, while ERAD or ER-phagy takes care of those that slip through and end up being released, thus maintaining proteostasis.
It is worth noting that CDK5RAP3 itself has been implicated in ER-phagy (Stephani et al. 2020), which would suggest UFMylation pulling double duty in co- and post-translational quality control. In their work, Stephani and colleagues suggest that UFM1 regulates CDK5RAP3's binding to ATG8-like proteins by competing with them, but loses its inhibitory role upon uL24 modification. With the structure of the $E3^{UFM1}$ ligase in mind, this seems even more plausible. While the disordered region of CDK5RAP3, which contains the ATG8 interacting motifs, remains unresolved in our works, it is clearly positioned away from the ribosome, thus exposing it to its potential binding partners. The binding of the E3 ligase could serve as the first step of phagosome formation by activating CDK5RAP3. It would be interesting to see how this process continues, and whether perhaps phagosomes begin forming upon deUFMylation-dependent E3 disassembly.

DeUFMylation: The final frontier

The majority of work presented here, the structural data in particular, focused on UFMylation and its consequences, with deUFMylation only briefly explored. It is clear from the biochemical data that deUFMylation plays an important role in both recycling and ER-RQC. The crystal structures of the 2 deconjugases UFSP1 and UFSP2 are known (Ha et al. 2008, 2011), and their distinct roles were recently delineated, with UFSP1 being involved in UFM1 maturation, whereas UFSP2 acts in removing the modification (Millrine et al. 2022). There are, however, no structural studies showcasing UFSP2 acting on a modified substrate. Such data would be essential in understanding potential triggers signaling for the removal of UFM1. In addition, UFSP2 acts in complex with the membrane-tethered ODR4 (Millrine et al. 2022; Chen et al. 2014), although it is unclear whether this only serves to recruit it to the ER or whether there is some regulatory effect involved as well. With all of this in mind, resolving the deUFMylation reaction remains an interesting avenue for further research.

Acknowledgements

When I first decided I wanted to do a PhD, I was not quite sure I was cut out for it. In all honesty, I still have my doubts every now and then, but I somehow made it to the finish line regardless. The journey was long, yet, in retrospect, much more pleasant than I initially thought it would be. This is in large part due to the people who accompanied me on the way, who I'd like to thank for that.

First and foremost, of course, I would like to thank Roland for the opportunity to work in his lab and for his supervision throughout the years. He took me into his lab despite the ongoing global pandemic five years ago, something not every PI was willing to do at the time with all the uncertainty in the world. His optimism towards science was certainly infectious at times and was a large contributing factor to any breakthroughs. I would also like to express my thanks to Prof. Dr. Karl-Peter Hopfner for agreeing to be a part of my thesis committee as well as second advisor, and as well rest of my thesis committee: Prof. Dr. Julian Stingele, Prof. Dr. Danny Nedialkova, Prof. Dr. Klaus Förstemann, and Dr. Gregor Witte. I would like to thank IMPRS-ML for the opportunity to be part of an amazing PhD program, as well as my TAC members Prof. Dr. Klaus Förstemann and Prof. Dr. Konstantin Sparrer for their input throughout the years.

As science has progressed, it has become increasingly more difficult to master everything yourself, which is why I'm thankful for having had excellent collaborators to work with. I'd like to express my thanks to Prof. Dr. Ron Kopito and his team: Paul, Samantha, and Francesco for the wonderful collaborative work throughout the years. It is no exaggeration to say that a lot of the work here would not have been possible without them.

I'd next like to thank everybody in the lab for making this journey a pleasant and fruitful one. Be it help with experiments, fixing up servers, grilling, or playing beer pong, you all contributed in one way or another! Thomas, many thanks for all the various help throughout the years, be it fixing up manuscripts or moving furniture, as well as all the music talk! Leona, thank you for making the IT work only half as painful as it would have been otherwise, and Kathi, thank you for making sure the technology lasted as long as it did! Many thanks go out to our technician team - Andrea, Joanna, and Alicia, for keeping the lab afloat, and thanks to Birgitta for teaching me how to not destroy everything. The same goes out to the microscopy team - Otto, Susi, and Charlotte, for turning my samples into great data. I'd also like to thank my mentors in the lab - Lukas, Robert, and Matthias, for helping me understand what I'm actually doing, all the way from my time as a rotation student. Many thanks also go out to Timo for his assistance with everything

and anything in the lab. Next, I'd like to thank Timur for all his help with modeling, gradients, and random trivia, as well as always keeping the lab morale high, be it with his endless baking, barbecue organization, or just daily games. The same goes out to Cristian, Hanna, and Shuangshuang - many thanks for all the science and beyond! Thanks to our newer additions to the lab - Martin, Hendrik, and Kohei, for the various discussions, be it science, coffee, or chess. And, of course, thanks to Gudrun for fighting German university bureaucracy in my stead!
Last, but certainly not least, I'd like to thank my family for their support throughout the years. Thank you so much for making all of this possible.

Article

UFM1 E3 ligase promotes recycling of 60S ribosomal subunits from the ER

https://doi.org/10.1038/s41586-024-07073-0

Received: 13 March 2023

Accepted: 15 January 2024

Published online: 21 February 2024

Check for updates

Paul A. DaRosa[1,6], Ivan Penchev[2,6], Samantha C. Gumbin[1], Francesco Scavone[1], Magda Wąchalska[1], Joao A. Paulo[3], Alban Ordureau[3,5], Joshua J. Peter[4], Yogesh Kulathu[4], J. Wade Harper[3], Thomas Becker[2], Roland Beckmann[2]✉ & Ron R. Kopito[1]✉

Reversible modification of target proteins by ubiquitin and ubiquitin-like proteins (UBLs) is widely used by eukaryotic cells to control protein fate and cell behaviour[1]. UFM1 is a UBL that predominantly modifies a single lysine residue on a single ribosomal protein, uL24 (also called RPL26), on ribosomes at the cytoplasmic surface of the endoplasmic reticulum (ER)[2,3]. UFM1 conjugation (UFMylation) facilitates the rescue of 60S ribosomal subunits (60S) that are released after ribosome-associated quality-control-mediated splitting of ribosomes that stall during co-translational translocation of secretory proteins into the ER[3,4]. Neither the molecular mechanism by which the UFMylation machinery achieves such precise target selection nor how this ribosomal modification promotes 60S rescue is known. Here we show that ribosome UFMylation in vivo occurs on free 60S and we present sequential cryo-electron microscopy snapshots of the heterotrimeric UFM1 E3 ligase (E3(UFM1)) engaging its substrate uL24. E3(UFM1) binds the L1 stalk, empty transfer RNA-binding sites and the peptidyl transferase centre through carboxy-terminal domains of UFL1, which results in uL24 modification more than 150 Å away. After catalysing UFM1 transfer, E3(UFM1) remains stably bound to its product, UFMylated 60S, forming a C-shaped clamp that extends all the way around the 60S from the transfer RNA-binding sites to the polypeptide tunnel exit. Our structural and biochemical analyses suggest a role for E3(UFM1) in post-termination release and recycling of the large ribosomal subunit from the ER membrane.

UFM1, like other UBLs, is conjugated to its targets by a canonical E1–E2–E3 enzymatic cascade, whereby the E3 ligase specifies target selection[5]. E3(UFM1) is a scaffold-type ligase that is composed of a stoichiometric assembly of three subunits: UFL1, DDRGK1 (also known as UFBP1 or C20orf116) and CDK5RAP3. None of these subunits share common motifs or homologies with other ubiquitin or UBL E3 ligases[6]. Two of the subunits, UFL1 and DDRGK1, are composed predominantly of predicted winged helix (WH) motifs and constitute the minimal E3 ligase catalytic unit[6,7]. CDK5RAP3 is not essential for E3 ligase activity in vitro but seems to function as a substrate adaptor or selectivity factor that constrains E3(UFM1) ligase activity to mono-UFMylate the ribosomal protein uL24 on amino acid residue K134 (ref. 6). A transmembrane domain on DDRGK1 tethers E3(UFM1) to the ER membrane to restrict E3(UFM1) activity to ER-docked ribosomes[2]. Accordingly, UFMylation is strongly linked to the maintenance of protein homeostasis in the ER[8,9].

Although the function of uL24 on the ribosome is not completely understood, its localization at the polypeptide tunnel exit on 60S places the site of UFM1 modification at a strategic position to influence the interaction between ER-bound ribosomes and the SEC61 translocon[2]. UFMylation of uL24 is increased after ER-specific ribosome stalling[3,4] and is essential for ribosome-associated quality-control (RQC)-dependent degradation of partially translocated, nascent 'arrest peptides' (ER–APs) that obstruct both the ribosome exit tunnel and the SEC61 translocon following the splitting of ribosomes[4]. These data led us to propose that uL24 UFMylation weakens the junction between post-termination 60S subunits and SEC61 translocons, thereby allowing the cytosolic ubiquitin–proteasome system (UPS) machinery to access ER–APs that are otherwise occluded by the tight ribosome–translocon junction[4]. A key feature of this model is the existence of an unidentified UFMylation 'reader' that recognizes the uL24-conjugated UFM1 moiety and induces a conformational change that disrupts the tight interaction between SEC61 and terminated 60S.

Association of E3(UFM1) with UFMylated 60S

To identify potential UFMylation readers in the ER membrane, we used proximity labelling with miniTurbo (mT)[10] fused to the amino terminus of UFM1 (mT–UFM1) knocked into the endogenous *UFM1* locus (Extended Data Fig. 1a). Control experiments confirmed that the predominant cellular target of mT–UFM1 is uL24 and that adduct formation was abrogated in E1 knockout ($UBA5^{KO}$) cells (Extended Data Fig. 1b–d) and was substantially enhanced in cells lacking the

[1]Department of Biology, Stanford University, Stanford, CA, USA. [2]Department of Biochemistry, Gene Center, University of Munich, Munich, Germany. [3]Department of Cell Biology, Harvard Medical School, Boston, MA, USA. [4]Medical Research Council Protein Phosphorylation and Ubiquitylation Unit (MRC-PPU), School of Life Sciences, University of Dundee, Dundee, UK. [5]Present address: Cell Biology Program, Sloan Kettering Institute, Memorial Sloan Kettering Cancer Center, New York, NY, USA. [6]These authors contributed equally: Paul A. DaRosa, Ivan Penchev. ✉e-mail: beckmann@genzentrum.lmu.de; kopito@stanford.edu

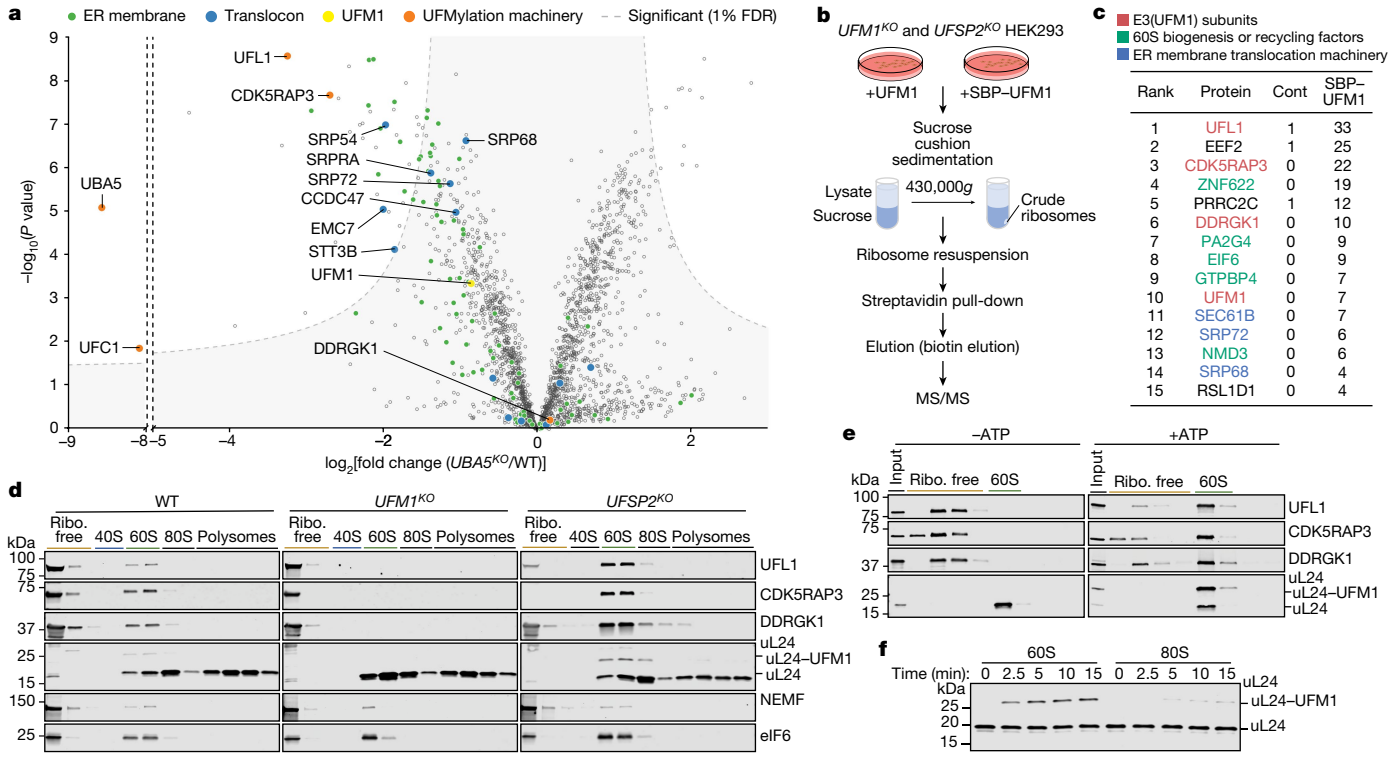

Rank	Protein	Cont	SBP–UFM1
1	UFL1	1	33
2	EEF2	1	25
3	CDK5RAP3	0	22
4	ZNF622	0	19
5	PRRC2C	1	12
6	DDRGK1	0	10
7	PA2G4	0	9
8	EIF6	0	9
9	GTPBP4	0	7
10	UFM1	0	7
11	SEC61B	0	7
12	SRP72	0	6
13	NMD3	0	6
14	SRP68	0	4
15	RSL1D1	0	4

Fig. 1 | E3(UFM1) forms a long-lived complex with UFMylated 60S. a, Volcano plot of proteins proximal to UFM1 conjugates identified by tandem mass tag (TMT) MS^3 spectroscopy in wild-type (WT) and *UBA5*^{KO} U2OS cells. UFM1 conjugates are highly enriched in ER membrane components, particularly those associated with protein translocation and insertion and UFM1 conjugation. Grey area denotes significant boundaries (two-tailed Student's *t*-test [S0 = 0.585], corrected for multiple comparisons by permutation-based false discovery rate (FDR) [1%]). **b**,**c**, Experimental workflow (**b**) and table (**c**) summarizing MS/MS analysis of affinity-captured UFMylated ribosomes. The table shows proteins that were enriched by >10-fold over control (Cont) and had at least 4 spectral counts. **d**, Sucrose gradient sedimentation analysis of membrane fractions from K562 cells of the indicated genotypes immunoblotted with the indicated antibodies. Ribo., ribosome. **e**, Sucrose gradient sedimentation analysis of purified 60S, UFMylated by purified UFMylation components (E1, E2, E3 and UFM1) in vitro in the presence or absence of ATP as indicated. **f**, 60S is the preferred substrate of UFMylation. Purified 60S or salt-washed 80S ribosomes were incubated for the indicated times with purified UFMylation components and analysed by immunoblotting for uL24. Blots and MS experiments are representative of at least two independent replicates with similar results (see the section 'Reproducibility and statistics' in the Methods for details). Source data are available in Supplementary Tables 1 and 2 (**a** and **c**) and Supplementary Fig. 1 (**d**–**f**).

ER-membrane-tethered deUFMylase UFSP2 (refs. 2,11) (Extended Data Fig. 1b). Furthermore, uL24 modification with mT–UFM1 was stimulated by inducing ribosome collisions with substoichiometric concentrations of anisomycin, and mT–UFM1-modified uL24 co-sedimented with ribosomes (Extended Data Fig. 1c). Thus, mT–UFM1 mimics the biochemical properties of untagged UFM1, which made it a suitable probe to analyse the UFM1 proximitome. Because the steady-state level of UFM1 conjugates in cells is low compared with that of free UFM1 (ref. 2), we used a workflow that enables statistically robust, direct comparison of total mT–UFM1-proximal proteins captured from wild-type cells with those identified in UFMylation-deficient *UBA5*^{KO} cells (Extended Data Fig. 1a). This approach was validated in control experiments, which showed that biotin modification of the UFMylation E2 enzyme UFC1, which forms thioester and peptidyl adducts with UFM1 (ref. 12), was completely abrogated in *UBA5*^{KO} cells (Extended Data Fig. 1d) and in the full dataset (Fig. 1a). In total, we quantified 2,213 streptavidin-enriched proteins (Supplementary Table 1), of which 54 (2.4%) were significantly and strongly (more than twofold) affected after UBA5 deletion (Fig. 1a and Supplementary Table 1). Significant hits were enriched for ER-membrane-localized proteins, including components of the translocation, ER-targeting and N-glycosylation machinery (Fig. 1a). This result is consistent with restriction of UFM1 conjugation to 60S subunits docked at ER membrane translocons[2]. Although the proximity labelling approach failed to identify new ER-membrane proteins that could be considered as plausible candidates for a UFM1 reader, we noted that E3(UFM1) subunits ranked among the most highly enriched (>8-fold) and significant ($P < 10^{-9}$) proteins, which suggested that the membrane-tethered E3(UFM1) itself could potentially function as a reader for UFMylated ribosomes at the ER membrane. Indeed, all three E3(UFM1) subunits were strongly enriched in tandem mass spectrometry (MS/MS) analyses of streptavidin-binding peptide (SBP)–UFM1 affinity-captured material from *UFSP2*^{KO} cells (Fig. 1b,c and Extended Data Fig. 1e), which strongly suggested that this E3 enzyme complex remains bound to 60S after catalysing UFM1 transfer to uL24. The strong enrichment for proteins involved in 60S recycling and biogenesis (eIF6, ZNF622, PA2G4, GTPBP4 and NMD3) is consistent with the known role of UFMylation in the recycling of 60S subunits following collision-induced stalling of ribosomes engaged in co-translational translocation at the ER[3,4], and with data from genome-wide co-essentiality network analysis (Extended Data Fig. 2a,b).

To understand this persistent interaction of E3(UFM1) with UFMylated 60S, the product of the conjugation reaction it catalyses, we analysed the distribution of UFMylated uL24 and E3(UFM1) subunits on sucrose density gradients of whole cell lysates (Extended Data Fig. 1f–h) and membrane fractions (Fig. 1d and Extended Data Fig. 1i,j) from K562 cells. UFMylated uL24 and E3(UFM1) co-sedimented with 60S fractions from wild-type cells (Fig. 1d, left, and Extended Data Fig. 1f–h), a result consistent with prolonged association between E3(UFM1) and UFMylated ribosomes. The finding that eIF6 and NEMF—proteins that bind to the subunit interface on free 60S ribosomes[13–17]—co-sedimented with UFMylated uL24 and E3(UFM1) (Fig. 1d and Extended Data Fig. 1g, quantified in Extended Data Fig. 1h) suggests that in cells, E3(UFM1)

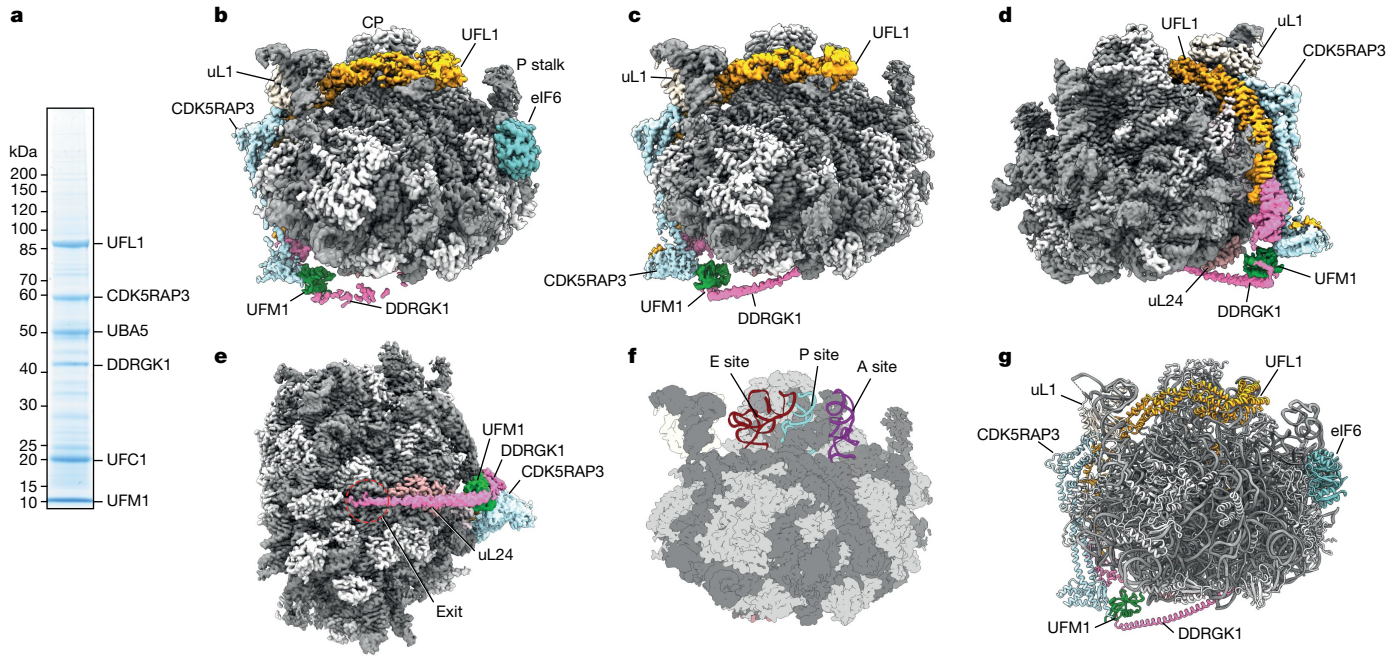

Fig. 2 | Structural analysis of the 60S–UFM1–E3(UFM1) complex. a, Coomassie-stained Nu-PAGE gel of Flag–UFM1 pull-down showing enrichment of E3(UFM1) subunits. **b**, Cryo-EM density map of the native 60S–UFM1–E3(UFM1) complex isolated from cells. Map shown from the intersubunit interface side as the crown view. The non-ribosomal extra density for 60S–UFM1–E3(UFM1) spans from the tunnel exit, over uL24, towards the L1 stalk, and over the tRNA-binding sites. CP, central protuberance. **c**–**e**, Cryo-EM density map of 60S–UFM1–E3(UFM1) complex reconstituted with purified components (in vitro) shown at the same angle as in **b** (**c**), as the back view (**d**; rotated about 180° from **b**) and as the bottom view (**e**; rotated about 90° from **d**) near the tunnel exit (exit; red dashed circle). The in vitro map recapitulates the densities seen from cellular pull-downs. **f**, Positions of A, P and E sites with tRNAs superimposed to a model for the 60S subunit shown at the same angle as the densities in **b** and **c**. rRNA is shown in dark grey, ribosomal proteins in light grey. Protein Data Bank (PDB) identifiers: 6Z6M for E-tRNA; 5MC6 for A-tRNA and P-tRNAs and 60S. **g**, Molecular model of the 60S–UFM1–E3(UFM1) complex derived from the density map in **c**. All cryo-EM maps are shown after post-processing using DeepEMhancer software. For clarity, the density for the E3(UFM1) complex is shown at lower contour levels compared with the 60S. Source data are available in Supplementary Fig. 1 for **a**.

and UFMylated uL24 associate predominantly with free 60S. The loss of E3(UFM1) association with ribosomes in *UFM1*^{KO} cells (Fig. 1d, middle) suggests that this ligase binds more persistently to UFMylated than to unmodified 60S. Conversely, inducing ribosome collisions with anisomycin (Extended Data Fig. 1k,l) or inactivating UFSP2, manipulations that increase the fraction of UFMylated 60S (Fig. 1d, right), resulted in proportionately increased association of E3(UFM1) subunits with 60S. Moreover, all three E3(UFM1) subunits co-sedimented with 60S following in vitro UFMylation reconstitution with purified, soluble, recombinant E1, E2 and E3 (ref. 6) (Fig. 1e) in the presence, but not in the absence of ATP. Together, these results confirm that uL24 UFMylation is both necessary and sufficient for persistent association of E3(UFM1) with 60S. When purified salt-washed 60S or 80S were added to an in vitro UFMylation assay, 60S ribosomes were more rapidly modified than 80S (Fig. 1f), even in the presence of a twofold excess of 80S (Extended Data Fig. 1m). By contrast, 80S ribosomes were less efficiently UFMylated in the cell-free assay (Extended Data Fig. 1n). Overall, these data reveal that uL24 on free 60S subunits is the preferred substrate of UFMylation.

Architecture of the 60S–E3(UFM1) complex

As expected from the preceding analysis, 3×Flag-tagged UFM1 (Flag–UFM1) affinity-captured material was heavily enriched for 60S ribosomal proteins and all three E3(UFM1) subunits (Fig. 2a). Single-particle cryo-electron microscopy (cryo-EM) analysis of this material (Extended Data Fig. 3a) identified 60S with an extraribosomal density that could be assigned to eIF6 (Fig. 2b). Several classes contained additional continuous density that was assigned to UFM1 (near uL24) and the E3(UFM1) complex, with the best-resolved 60S class refined to 3.1 Å (Fig. 2b, Extended Data Fig. 4a and Extended Data Table 1). Cryo-EM analysis of in vitro UFMylated 60S (Extended Data Fig. 3b) produced an essentially identical three-dimensional (3D) reconstruction (lacking eIF6) of the 60S–UFM1–E3(UFM1) complex at a higher resolution of 2.9 Å (Fig. 2c–e and Extended Data Fig. 4a). The region around uL24 and the tunnel exit exhibited even higher local resolution, ranging from 2.3 Å for the ribosomal core to 3–7 Å for the UFM1–E3(UFM1) complex (Extended Data Fig. 4b,c). In both native and in vitro-reconstituted complexes, E3(UFM1) adopted the same elongated clamp-like configuration, spanning from the tunnel exit (Fig. 2d,e) to the empty transfer RNA (tRNA)-binding sites (Fig. 2f). These data, in combination with AlphaFold 2 (ref. 18) and AlphaFold-Multimer[19] structure predictions, enabled us to build a near-complete molecular model of 60S–UFM1–E3(UFM1) (Fig. 2g, Extended Data Figs. 5a–c and 6 and Extended Data Table 1).

Molecular model of the 60S–E3(UFM1) complex

The 60S–UFM1–E3(UFM1) molecular model revealed the overall structure and interactions of E3(UFM1) and suggested how it can read the UFM1 modification on 60S (Fig. 3a,b). Although the local resolution of UFM1 is relatively low, it is positioned over its substrate uL24 near its known conjugation site at K134 (refs. 2,3) (Fig. 3b and Extended Data Fig. 6c). Notably, UFM1 is not in direct contact with UFL1 but instead with DDRGK1 and CDK5RAP3, which in turn form an intricate interaction network and a well-ordered complex with UFL1 (Fig. 3a,b and Extended Data Fig. 6b).

In this E3(UFM1) complex, UFL1 serves as a central scaffold that consists of a predicted short N-terminal α-helix followed by one partial winged-helix (pWH), five WH motifs, a bipartite coiled-coil (CC) domain

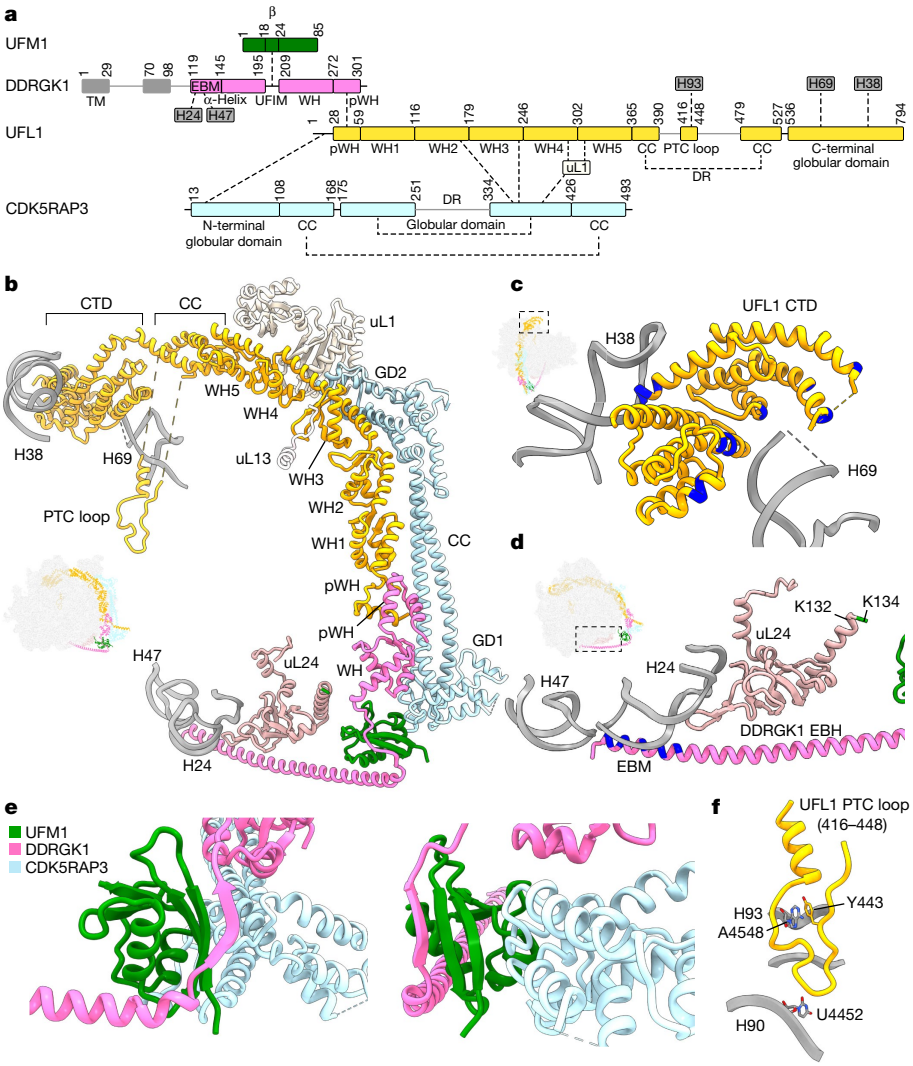

Fig. 3 | Organization of the E3(UFM1) complex bound to UFMylated 60S. **a**, Schematic representation of the domain organization of the E3(UFM1) complex and interactions among the components of the E3 complex, UFM1 and the 60S subunit. TM, transmembrane domain. **b**, Overview of the 60S-bound UFM1–E3(UFM1) molecular model. **c**, Position of the UFL1 CTD between H38 and H69 with positively charged residues close to the rRNA highlighted in blue. **d**, Position of the DDRGK1 EBH close to the tunnel exit; the UFMylation target lysine on uL24, K134 and positively charged residues at the tip of the DDRGK1 EBM are highlighted green and blue, respectively. **e**, Interaction of DDRGK1 and CDK5RAP3 with UFM1. Left, predicted β-augmentation of the UFIM motif and the preceding three turns of the EBH of DDRGK1 with UFM1. Right, alternative view showing proximity and limited interactions with CDK5RAP3. **f**, Structured PTC loop of UFL1 (D416–V448) near the PTC within the disordered region (UFL1(N391–F479)). In **b**–**d**, thumbnails indicate the overall orientation of the complex.

with a disordered region that reaches into the peptidyl transferase centre (PTC) and bridges the two helices and a C-terminal globular domain (Fig. 3a–c and Extended Data Fig. 6a,b). DDRGK1 contains an N-terminal transmembrane domain and a flexible linker region (residues 1–118) that were not visualized in our reconstructions. The remainder of DDRGK1 consists of a long α-helix (amino acids 119–195) connected through a short linker (amino acids 196–208) to a WH motif and a pWH. The latter complements the N-terminal pWH domain of UFL1 to form a composite WH, thereby linking these two subunits to form the backbone of the minimal E3 ligase complex[6]. The CDK5RAP3 subunit of E3(UFM1) packs against the UFL1–DDRGK1 backbone through a long CC domain flanked by two globular domains, GD1 and GD2. GD1 is predicted by AlphaFold-Multimer to contact the N-terminal α-helix of UFL1, whereas GD2 interacts with WH2 and WH3 of UFL1, together giving rise to an overall C-shaped appearance of E3(UFM1) (Fig. 3b).

The interaction of E3(UFM1) with 60S is multimodal, with contributions from all three subunits. The C-terminal globular domain of UFL1 is sandwiched between 28S ribosomal RNA (rRNA) helices H38 and H69 probably through complementary charges (Fig. 3c). These helices constitute functionally important sites in the active 80S ribosome, namely the A site finger (H38), which coordinates the A site tRNAs, and the main intersubunit bridge B2A (between H69 and 18S rRNA helix h44). As a result, the C-terminal domains of UFL1 occlude all three tRNA-binding sites (Fig. 2e,f). In addition, a small helix and loop (PTC loop) of the UFL1 disordered region are positioned in the P site near the PTC where the conformation of the PTC base U4452 (U2506 of *Escherichia coli*) is remodelled (Fig. 3b,f) and the Y443 aromatic ring of UFL1 is stacked on A4548 (A2602 in *E. coli*) (Extended Data Fig. 6d). This binding mode of E3(UFM1) is therefore mutually exclusive with any tRNA binding. The most intimate interaction of UFL1 with 60S occurs near the E site and with the ribosomal L1 stalk, where WH4 and WH5 of UFL1 and GD2 of CDK5RAP3 share extensive contacts that stabilize this otherwise flexible element (Fig. 3b). The WH backbone, composed of the C-terminal WH domains of DDRGK1 and UFL1 and the CC region of CDK5RAP3, reaches towards uL24 (Fig. 3b), displacing the tip of the rRNA segment H25ES7 and the C-terminal α-helix of uL13, both of

which form contacts with UFL1. From uL24, the long α-helix of DDRGK1 (exit-binding helix (EBH)) stretches all the way to the tunnel exit. Its positively charged N-terminal end (designated as the exit-binding motif (EBM); Fig. 3a,d) is positioned on rRNA H47 and H24 (Fig. 3b,d), which are part of the binding site for exit-site factors such as SRP, SRP receptor (SR) and SEC61 (refs. 20,21). Across from uL24, the short linker of DDRGK1 (amino acids 196–208) between the EBH (amino acids 119–195) and the WH domain (amino acids 209–272) contains a conserved UFM1-interacting motif[22] (UFIM; Extended Data Fig. 5d) that is predicted by AlphaFold-Multimer to interact with UFM1 through β-augmentation (Fig. 3a,b,e and Extended Data Figs. 5e,f and 6c). Although the cryo-EM density map displayed an overall lower local resolution in this region (about 7–8 Å; Extended Data Fig. 4b), and we cannot exclude a different mode of interaction, the AlphaFold model is supported by good agreement with the corresponding density in our map (Extended Data Fig. 6c) by its similarity to the β-augmented interaction of UBA5 with UFM1 (ref. 23) (Extended Data Fig. 5g) and by site-directed mutagenesis results (see below). Together, these data suggest a model whereby uL24-conjugated UFM1 forms the nexus of an intimate interaction network that allows E3(UFM1) to read the 60S modification.

The mono-UFMylated 60S particles observed in our native cryo-EM structures from the UFM1 pull-down assays clearly represent a state of the 60S devoid of peptidyl-tRNA or nascent chains as occurring during (cytoplasmic) RQC. Furthermore, the positioning of the EBM of DDRGK1 at the universal binding site of the tunnel exit is likely to preclude binding of SEC61. This result, together with the presence of eIF6 in the native structure, indicates that the observed particle represents a post-termination 60S subunit after dissociation from SEC61.

The UFL1 C terminus initiates 60S engagement

Flag–UFL1 pull-downs were also strongly enriched for all three subunits of E3(UFM1) (Fig. 4a). Single-particle cryo-EM analyses of this material exhibited substantially higher heterogeneity than with Flag–UFM1 pull-downs, the most notable feature of which was the presence of the SEC61 complex at the tunnel exit in a subset of particles (Fig. 4b and Extended Data Figs. 4, 7 and 8). 3D classification of the Flag–UFL1-captured particles revealed three distinct states of E3(UFM1)–60S interaction, with the most populated state, state 3 (Fig. 4b), being largely indistinguishable from the post-UFMylation state observed in Flag–UFM1 pull-downs and in vitro UFMylated 60S, but at a higher local resolution for many regions of the E3 ligase (Fig. 4b and Extended Data Figs. 4 and 7). One feature of the UFL1-captured 60S was a weak extra density in the peptide exit tunnel, which might represent a nascent polypeptide chain or an exit-tunnel-binding factor. Notably, states 1 and 2 were bound to SEC61 and exhibited more restricted interaction surfaces with E3(UFM1). We propose that states 1 and 2 represent SEC61-bound states that exist before and after UFM1 conjugation, respectively. In the state 1 complex, we observed density only for the UFL1 C-terminal domain (CTD; CC, WH4 and WH5) occupying the tRNA-binding sites and the UFL1–CDK5RAP3 region protruding from the ribosome near the L1 stalk (Fig. 4b). No density was observed for UFM1 or the rest of E3(UFM1) in the uL24 region, and rRNA H25ES7 was in its canonical position. By contrast, in state 2, we observed uL24 already UFMylated and E3(UFM1) almost fully accommodated as in state 3; however, the N-terminal EBH of DDRGK1 was not visible and SEC61 was still present at the tunnel exit (Fig. 4b).

As the C-terminal region of UFL1, including the PTC loop, is present in all three states, we suggest that the first step of 60S recognition by E3(UFM1) is the binding of the UFL1 C-terminal regions to the L1 stalk and/or to a tRNA-free intersubunit surface. UFMylation of uL24 then eventually leads to rigid positioning of the DDRGK1 N terminus, including the EBH at the tunnel exit. This positioning seems to be mutually exclusive with SEC61 binding (Extended Data Fig. 9a,b). Moreover, we never observed the EBH together with SEC61 in the same particle.

To test the role of the C terminus of UFL1 in initiating engagement of E3(UFM1) with 60S, we evaluated the impact of replacing endogenous UFL1 with UFL1 variants harbouring progressive C-terminal UFL1 truncations on uL24 UFMylation (Fig. 4c and Extended Data Fig. 5i). Deletion of the globular CTD alone (UFL1(1–532); ΔCTD) still supported detectable, albeit reduced UFMylation. By contrast, further deletion of the CTD-proximal CC helix, together with part of the adjoining disordered domain (UFL1(1–410)), caused almost complete abrogation of UFMylation, as did a more extensive truncation (UFL1(1–116)). These results confirm the importance of the precise packing of the CTD between 28S rRNA helices H38 and H69 (Fig. 3c) and suggest a role for the CC domain and potentially the disordered regions, including the PTC loop, in stabilizing the initial encounter between E3(UFM1) and 60S. These results differ from a previous study[6], in which 60S UFMylation, reconstituted in vitro, was unaffected by the Δ411–794 deletion. This discrepancy probably reflects either kinetic or stoichiometric differences between these two experimental methods or perhaps the influence of factors specific to the cellular environment that are absent in the cell-free reconstitutions. The importance of the UFL1 C terminus in targeting the E3 to ribosomes in the cell may provide an explanation for the preference for 60S as this region is not accessible in 80S ribosomes.

uL24 UFMylation displaces SEC61 from 60S

To test the role of EBM and UFIM in UFMylation, we expressed wild-type DDRGK1 or variants that disrupt either the EBM (Δ119–145; ΔEBM) (Fig. 3a,d and Extended Data Fig. 5h) or the UFIM (UFIM(mt); F196V, V198A and E201P) in *DDRGK1*^{KO} cells (Fig. 3a,e and Extended Data Fig. 5f). Deleting the EBM slightly increased uL24 UFMylation (Fig. 4d, left), but had no discernible effect on co-sedimentation of E3(UFM1) with 60S (Extended Data Fig. 9c,d). By contrast, UFIM disruption completely abrogated the stable E3(UFM1)–ribosome association while enhancing uL24 UFMylation (Fig. 4d, left, and Extended Data Fig. 9c,d). The increased uL24 UFMylation observed in cells expressing UFIM(mt) probably reflects enhanced dissociation of the mutant E3 from its UFMylated 60S product, which allows the mutant enzyme to modify more ribosomes. This interpretation is reinforced by the observation that a substantial fraction (around 50%) of UFMylated uL24 in UFIM(mt)-expressing cells was associated with cytosolic ribosomes compared with wild-type HEK293 cells or *DDRGK1*^{KO} cells rescued with wild-type DDRGK1 or DDRGK1(ΔEBM), in which the majority of UFMylated uL24 is on ER-bound ribosomes (Fig. 4d, right). These data support the conclusion that β-augmentation between UFM1 and DDRGK1 is strictly required for persistent binding of E3(UFM1) to its UFMylated product on 60S and suggest that this interaction facilitates positioning of the EBM near the tunnel exit to promote dissociation of SEC61 from ribosomes. In addition to the steric clash of SEC61 with the DDRGK1 EBM (Extended Data Fig. 9a,b), E3(UFM1) as observed in state 3, would clash with the ER membrane phospholipid bilayer, as visualized in cryo-electron tomography maps of mammalian ER-membrane-bound 80S ribosomes[24] (Extended Data Fig. 9e,f). Accommodation of the state 3 E3(UFM1) therefore requires re-orientation of 60S with respect to the ER membrane by a backward tilt that is likely to further destabilize the ribosome–SEC61 interaction.

We next directly tested the role of UFMylation in promoting SEC61–60S dissociation. We used co-sedimentation of detergent-solubilized SEC61 with ribosomal subunits following forced termination with puromycin (Fig. 4e and Extended Data Fig. 9g) or run-off translation in the presence of harringtonine (Fig. 4f and Extended Data Fig. 9h,i) to monitor the effect of disrupting UFMylation on translocon–ribosome dissociation kinetics. In wild-type cells, SEC61 dissociated from ribosomes with a half-time of about 1 and 15 min following treatment with puromycin or harringtonine, respectively. By contrast, the rate of SEC61 dissociation was substantially reduced in UFMylation-defective *UFC1*^{KO} cells (Fig. 4e,f and Extended Data Fig. 9g,h) and *UFM1*^{KO}

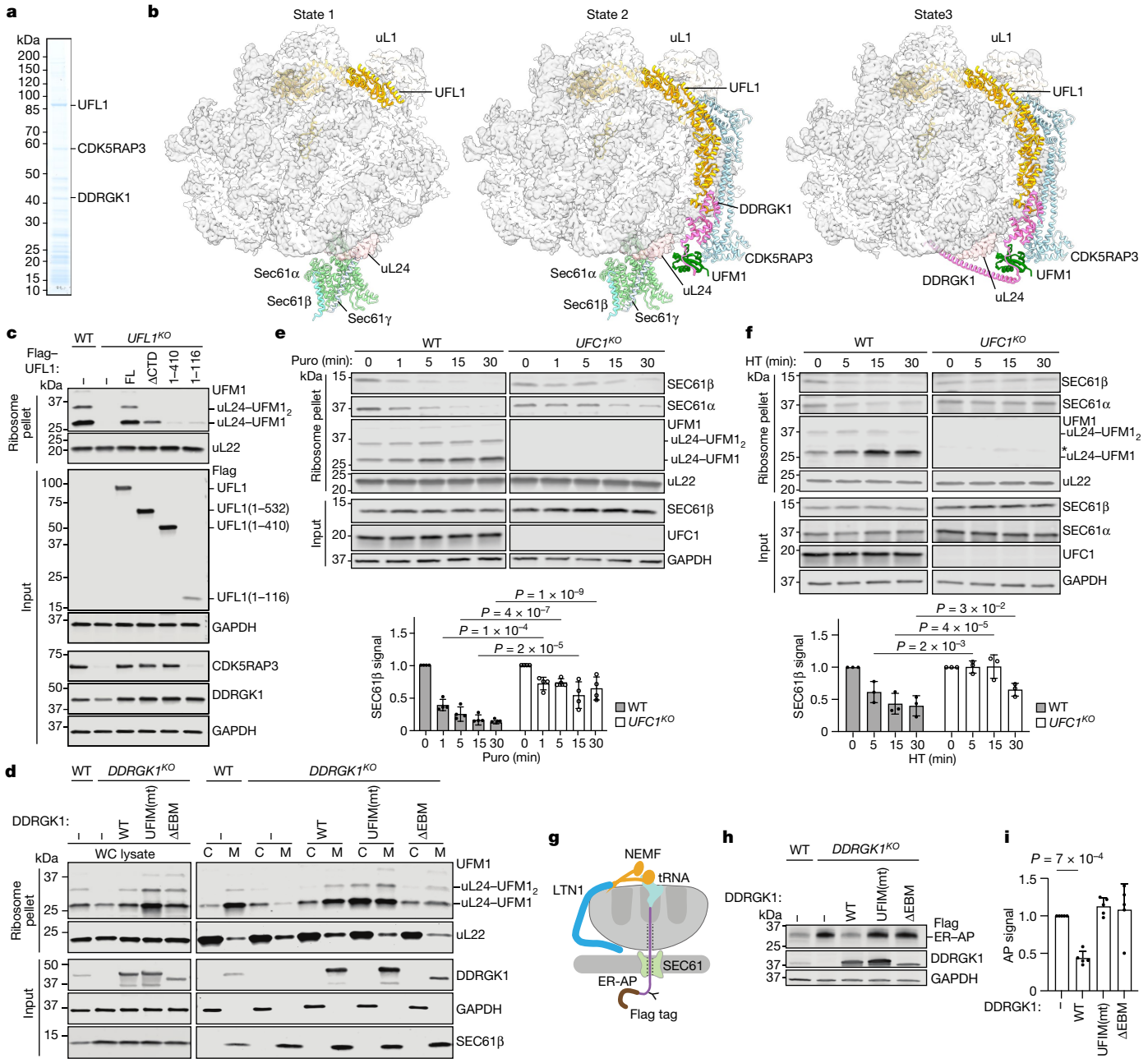

Fig. 4 | Sequential E3(UFM1) binding and UFMylation of 60S promotes SEC61 displacement. a, Coomassie-stained NuPAGE gel of Flag–UFL1 pull-down. **b**, Cryo-EM models of 60S–E3(UFM1) states from Flag–UFL1 pull-downs. **c**, Immunoblot analysis of WT or *UFL1*^{KO} HEK293 cells expressing Flag-tagged full-length (FL) or C-terminally truncated UFL1 mutants, immunoblotted for the indicated proteins. **d**, Immunoblot analysis of ribosome pellets or inputs from whole cell lysates (WC) or cytosolic (C) and membrane (M) fractions derived from *DDRGK1*^{KO} HEK293 cells expressing WT DDRGK1, UFIM(mt) or ΔEBM mutants. **e**,**f**, Dissociation of 60S from the translocon following puromycin (Puro)-induced (**e**) or run-off translation termination in the presence of harringtonine (HT) (**f**) in *UFC1*^{KO} cells. Top, immunoblot analysis of ribosome pellets or inputs from WT and *UFC1*^{KO} HEK293 cells treated with the indicated compounds. The asterisk in **f** indicates a nonspecific band. Bottom, quantification of SEC61β band intensities in ribosome pellets. Data show the mean ± s.d. and *P* values relative to untreated from indicated comparisons derived from two-way analysis of variance (ANOVA) followed by uncorrected Fisher's least significant difference (LSD) tests. $n = 4$ (**e**) and $n = 3$ (**f**) biological replicates. **g**, Schematic of restricted access of LTN1 to glycosylated, Flag-tagged ER–AP on SEC61-docked 60S generated from splitting stalled ER ribosomes. **h**, Rescue of ER–AP degradation in *DDRGK1*^{KO} cells transfected with WT, but not mutant (UFIM(mt) and ΔEBM) DDRGK1. **i**, Quantification of ER–AP intensities from data as in **h**. Data show mean GAPDH-normalized fold change ± s.d. relative to unrescued *DDRGK1*^{KO} cells and *P* value from the indicated comparison derived from one-way ANOVA of $n = 5$ biological replicates. Source data are available in Supplementary Figs. 2 (**a**,**c**–**e**) and 3 (**f**,**h**) and Supplementary Tables 6, 7 and 9 (for **e**, **f** and **i**, respectively). For *P* values and data replication descriptions, see the section 'Reproducibility and statistics' in the Methods.

cells (Extended Data Fig. 9i), with very little dissociation occurring even after 30 min. These data support the conclusion that UFM1 conjugation is required for the timely dissociation of 60S subunits from translocons following termination.

To assess the importance of ribosome dissociation in ER RQC, we asked whether the EBM and UFIM of DDRGK1 are functionally required for the degradation of an AP from an ER-targeted reporter (SS^{VgV}K20)[4] containing a polylysine (K20) tract to mimic 'nonstop' translation into

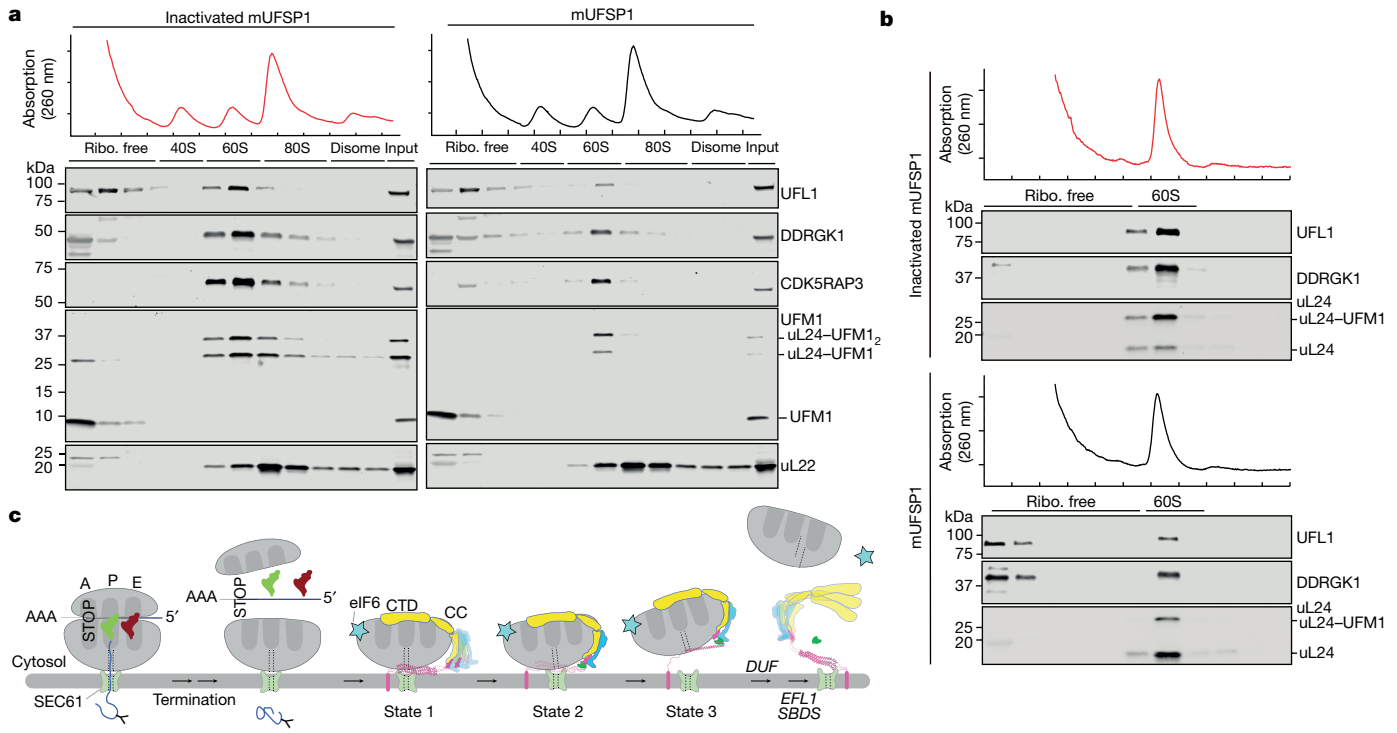

Fig. 5 | DeUFMylation promotes the dissociation of 60S and E3(UFM1). **a**, Lysates of *UFSP2*^{KO} K562 cells were treated with active (black) or NEM-inactivated (red) mouse UFSP1 (mUFSP1) and subjected to sucrose density gradient sedimentation fractionation (top) followed by immunoblotting with the indicated antibodies (bottom). **b**, Purified 60S was UFMylated in vitro with purified components and treated with recombinant mUFSP1 and analysed as in **a**. Data in **a** and **b** were replicated at least twice in independent experiments with similar results (for details, see the section 'Reproducibility and statistics' section in the Methods). Source data are available in Supplementary Fig. 4. **c**, Model of the sequential interaction of SEC61-bound 60S with E3(UFM1).

a poly(A). Ribosomes translating this reporter initiate co-translational ER translocation of the nascent chain through SEC61, but stall when they encounter the downstream K20 tract[4]. Collision-induced splitting of the stalled ribosome produced an ER-docked 60S–tRNA–AP (ER–AP) complex, whereas the presence of an N-glycan confirmed that the arrested nascent chain spanned from the P site through SEC61 into the ER lumen (Fig. 4g). We previously reported[4] that uL24 UFMylation of these 60S–tRNA–AP complexes is essential for the UPS to degrade these SEC61-obstructing and 60S-obstructing ER–APs. This led us to propose that recognition of the UFM1 mark by a UFM1 reader weakens the junction between 60S and the translocon, which then allows the cytosolic UPS machinery to access the ER–AP[4]. Here ER–AP stabilization observed after *DDRGK1* knockout was fully reversed by re-expression of wild-type DDRGK1 but not by expression of either UFIM(mt) or ΔEBM variants (Fig. 4h,i). Thus, formation of a stable 60S–UFM1–E3(UFM1) complex and precise positioning of the DDRGK1 EBM at the tunnel exit are essential for ER–AP degradation. This result supports the hypothesis that E3(UFM1) reads the UFM1 mark on 60S to destabilize the ribosome–SEC61 junction on ER-stalled 60S–tRNA–AP complexes. This in turn allows the UPS machinery to extract and degrade these partially translocated ER–APs.

DeUFMylation dissociates 60S and E3(UFM1)

We propose that hydrolysis of the isopeptide bond linking UFM1 to uL24 by UFSP2, an ER-tethered UFM1-specific hydrolase[2,11], enables the simultaneous release of 60S and recycling of UFM1 and E3(UFM1). Accordingly, genetic ablation of *UFSP2* leads to a substantial increase in UFMylation of membrane-associated uL24 (refs. 2,3) and to a corresponding increase in co-sedimentation of E3(UFM1) with 60S (Fig. 1d). The most direct test of the hypothesis that deUFMylation is necessary and sufficient to promote the release of UFMylated 60S from E3(UFM1) is to assess the effect of adding purified deUFMylase to the stability of E3(UFM1)–60S complexes in vitro. Because UFSP2 is unstable when separated from its oligomeric partner and membrane anchor ODR4 (ref. 2), we treated lysates of *UFSP2*^{KO} cells (Fig. 5a) or in vitro UFMylated, E3(UFM1)-bound 60S (Fig. 5b) with purified recombinant UFSP1, a cytosolic UFSP2 orthologue with similar substrate selectivity[11]. We then assessed E3(UFM1)–60S complex stability by sucrose gradient fractionation. Treatment with UFSP1, but not with N-ethylmaleimide (NEM)-inactivated UFSP1, substantially reduced both uL24 UFMylation and co-sedimentation of E3(UFM1) subunits with 60S (Fig. 5a,b). Thus, deUFMylation frees 60S ribosomes from the ER-anchored E3(UFM1) to release 60S subunits into the cytosol.

Conclusions

Our data revealed the elongated C-shaped structure of the heterotrimeric E3(UFM1) in a complex with 60S ribosomes. Notably, both our biochemical and structural data identified E3(UFM1) itself as the reader of its own 60S modification, which results in stable 60S association and ATP-driven disruption of the SEC61–60S junction. Here the UFM1 conjugate serves as the linchpin, coordinating E3(UFM1) binding through the DDRGK1 UFIM and concomitantly positioning the EBH of DDRGK1 such that it sterically clashes with (and therefore competes with) the trimeric SEC61 complex. The state 3 E3(UFM1)–60S interaction is also incompatible with larger translocon assemblies, such as the SEC61–OST complex[25] for secreted glycoproteins and the multipass membrane protein insertion SEC61–BOS–GEL complex[26–28]. The proposed SEC61–60S dissociation mechanism is likely to be multimodal and cooperative in a way that UFMylation not only stabilizes the DDRGK1 EBH at the tunnel exit but also forces the ribosome to tilt with respect to the membrane to further destabilize the translocon connection (Extended Data Fig. 9e,f). We propose a model that

explains the sequential engagement of E3(UFM1) with free 60S subunits that disrupts SEC61 binding and finally releases 60S subunits from the ER membrane after deUFMylation (Fig. 5c). The presence of eIF6 (Fig. 2b) on these newly released 60S subunits suggests that they are now primed for recycling by SBDS and EFL1 to enter another round of translation initiation.

Our data identified E3(UFM1) as a probable candidate for the long-sought 'detachment factor' first proposed in 1976 (ref. 29) to explain the exceedingly slow rate of release of terminated 60S subunits from microsomal membranes observed after translational termination in cell-free extracts[30]. There must also be UFM1-independent ways for post-termination 60S subunits to detach from ER translocons because mammalian cells can adapt to engineered deletion of UFM1 or its conjugation apparatus[2]. Moreover, some eukaryotic cells, notably those constituting the entire fungal kingdom, lack this UBL and its conjugation system[31,32], despite being able to support rapid recycling of 60S subunits from the ER[33].

UFMylation-dependent weakening of the 60S–translocon junction was previously inferred from our investigation of the epistatic relationship between UFMylation and the RQC machinery on ribosomes that stall during co-translational translocation of secretory proteins[4]. We propose that UFMylation therefore functions broadly to recycle translocon-engaged 60S subunits and translocons following either normal (Fig. 5c) or RQC-mediated termination. However, whether and how E3(UFM1) can engage ER RQC-derived 60S subunits with a bound peptidyl-tRNA, or even 80S ribosomes, remains to be elucidated.

It is unclear why eukaryotic cells have evolved such elaborate machinery to dissociate terminated 60S from the translocon. One possibility is that UFMylation prevents the initiation of non-secretory proteins on SEC61-docked 60S subunits by preventing eIF6 eviction. Normally, binding of eIF6 to the intersubunit interface of 60S subunits prevents 40S translation–initiation complexes from joining to form actively translating ribosomes. To allow the large subunit to enter a new translation cycle, eIF6 must be evicted by the GTPase EFL1 and its cofactor SBDS[34]. Because E3(UFM1) sterically clashes with the EFL1–SBDS binding site on 60S subunits[35] (Extended Data Fig. 2c), persistent E3(UFM1) association ensures that post-termination 60S subunits at the ER cannot re-engage in translation until they are released from the ER by deUFMylation (Fig. 5c). Although additional studies are needed to understand how these steps are coordinated, the essential relationship of the UFM1 pathway with the 60S licensing factors EFL1 and SBDS (Extended Data Fig. 2a,b) points to a fundamental, hitherto unappreciated role of this UBL in orchestrating ribosome recycling and quality control.

Online content

Any methods, additional references, Nature Portfolio reporting summaries, source data, extended data, supplementary information, acknowledgements, peer review information; details of author contributions and competing interests; and statements of data and code availability are available at https://doi.org/10.1038/s41586-024-07073-0.

1. Cappadocia, L. & Lima, C. D. Ubiquitin-like protein conjugation: structures, chemistry, and mechanism. *Chem. Rev.* **118**, 889–918 (2018).
2. Walczak, C. P. et al. Ribosomal protein RPL26 is the principal target of UFMylation. *Proc. Natl Acad. Sci. USA* **116**, 1299–1308 (2019).
3. Wang, L. et al. UFMylation of RPL26 links translocation-associated quality control to endoplasmic reticulum protein homeostasis. *Cell Res.* **30**, 5–20 (2020).
4. Scavone, F., Gumbin, S. C., DaRosa, P. A. & Kopito, R. R. RPL26/uL24 UFMylation is essential for ribosome-associated quality control at the endoplasmic reticulum. *Proc. Natl Acad. Sci. USA* **120**, e2220340120 (2023).
5. Millrine, D., Peter, J. J. & Kulathu, Y. A guide to UFMylation, an emerging posttranslational modification. *FEBS J.* **290**, 5040–5056 (2023).
6. Peter, J. J. et al. A non-canonical scaffold-type E3 ligase complex mediates protein UFMylation. *EMBO J.* **41**, e111015 (2022).
7. Ishimura, R. et al. Mechanistic insights into the roles of the UFM1 E3 ligase complex in ufmylation and ribosome-associated protein quality control. *Sci. Adv.* **9**, eadh3635 (2023).
8. Gerakis, Y., Quintero, M., Li, H. & Hetz, C. The UFMylation system in proteostasis and beyond. *Trends Cell Biol.* **29**, 974–986 (2019).
9. Xie, Z., Fang, Z. & Pan, Z. Ufl1/RCAD, a Ufm1 E3 ligase, has an intricate connection with ER stress. *Int. J. Biol. Macromol.* **135**, 760–767 (2019).
10. Branon, T. C. et al. Efficient proximity labeling in living cells and organisms with TurboID. *Nat. Biotechnol.* **36**, 880–887 (2018).
11. Kang, S. H. et al. Two novel ubiquitin-fold modifier 1 (Ufm1)-specific proteases, UfSP1 and UfSP2. *J. Biol. Chem.* **282**, 5256–5262 (2007).
12. Millrine, D. et al. Human UFSP1 is an active protease that regulates UFM1 maturation and UFMylation. *Cell Rep.* **40**, 111168 (2022).
13. Russell, D. W. & Spremulli, L. L. Mechanism of action of the wheat germ ribosome dissociation factor: interaction with the 60S subunit. *Arch. Biochem. Biophys.* **201**, 518–526 (1980).
14. Gartmann, M. et al. Mechanism of eIF6-mediated inhibition of ribosomal subunit joining. *J. Biol. Chem.* **285**, 14848–14851 (2010).
15. Lyumkis, D. et al. Structural basis for translational surveillance by the large ribosomal subunit-associated protein quality control complex. *Proc. Natl Acad. Sci. USA* **111**, 15981–15986 (2014).
16. Shao, S., Brown, A., Santhanam, B. & Hegde, R. S. Structure and assembly pathway of the ribosome quality control complex. *Mol. Cell* **57**, 433–444 (2015).
17. Shen, P. S. et al. Protein synthesis. Rqc2p and 60S ribosomal subunits mediate mRNA-independent elongation of nascent chains. *Science* **347**, 75–78 (2015).
18. Jumper, J. & Hassabis, D. Protein structure predictions to atomic accuracy with AlphaFold. *Nat. Methods* **19**, 11–12 (2022).
19. Evans, R. et al. Protein complex prediction with AlphaFold-Multimer. Preprint at *bioRxiv* https://doi.org/10.1101/2021.10.04.463034 (2022).
20. Halic, M. et al. Signal recognition particle receptor exposes the ribosomal translocon binding site. *Science* **312**, 745–747 (2006).
21. Beckmann, R. et al. Alignment of conduits for the nascent polypeptide chain in the ribosome–Sec61 complex. *Science* **278**, 2123–2126 (1997).
22. Habisov, S. et al. Structural and functional analysis of a novel interaction motif within UFM1-activating enzyme 5 (UBA5) required for binding to ubiquitin-like proteins and ufmylation. *J. Biol. Chem.* **291**, 9025–9041 (2016).
23. Padala, P. et al. Novel insights into the interaction of UBA5 with UFM1 via a UFM1-interacting sequence. *Sci. Rep.* https://doi.org/10.1038/s41598-017-00610-0 (2017).
24. Martinez-Sanchez, A. et al. Template-free detection and classification of membrane-bound complexes in cryo-electron tomograms. *Nat. Methods* **17**, 209–216 (2020).
25. Braunger, K. et al. Structural basis for coupling protein transport and N-glycosylation at the mammalian endoplasmic reticulum. *Science* **360**, 215–219 (2018).
26. McGilvray, P. T. et al. An ER translocon for multi-pass membrane protein biogenesis. *eLife* **9**, e56889 (2020).
27. Smalinskaitė, L., Kim, M. K., Lewis, A. J. O., Keenan, R. J. & Hegde, R. S. Mechanism of an intramembrane chaperone for multipass membrane proteins. *Nature* **611**, 161–166 (2022).
28. Sundaram, A. et al. Substrate-driven assembly of a translocon for multipass membrane proteins. *Nature* **611**, 167–172 (2022).
29. Blobel, G. Extraction from free ribosomes of a factor mediating ribosome detachment from rough microsomes. *Biochem. Biophys. Res. Commun.* **68**, 1–7 (1976).
30. Borgese, D., Blobel, G. & Sabatini, D. D. In vitro exchange of ribosomal subunits between free and membrane-bound ribosomes. *J. Mol. Biol.* **74**, 415–438 (1973).
31. Grau-Bové, X., Sebé-Pedrós, A. & Ruiz-Trillo, I. The eukaryotic ancestor had a complex ubiquitin signaling system of archaeal origin. *Mol. Biol. Evol.* **32**, 726–739 (2015).
32. Picchianti, L. et al. Shuffled ATG8 interacting motifs form an ancestral bridge between UFMylation and autophagy. *EMBO J.* **42**, e112053 (2023).
33. Jan, C. H., Williams, C. C. & Weissman, J. S. Principles of ER cotranslational translocation revealed by proximity-specific ribosome profiling. *Science* **346**, 1257521 (2014).
34. Jaako, P. et al. eIF6 rebinding dynamically couples ribosome maturation and translation. *Nat. Commun.* **13**, 1562 (2022).
35. Weis, F. et al. Mechanism of eIF6 release from the nascent 60S ribosomal subunit. *Nat. Struct. Mol. Biol.* **22**, 914–919 (2015).

Methods

Plasmids

Plasmids and DNA constructs were generated using standard PCR and site-directed mutagenesis techniques using Phusion polymerase (Thermo Fisher) and/or Q5 High Fidelity polymerase (NEB) and verified by sequencing. Lentiviral vectors for the expression of DDRGK1 and UFL1 were generated from a modified pLVX vector[36] with an *EF1a* promoter and a blasticidin selection marker. All lentivirus packaging vectors were obtained from Addgene. For cryo-EM pull-downs, 3×Flag N-terminally tagged UFM1 and C-terminally tagged UFL1 constructs were generated by PCR using Phusion polymerase (Thermo Fisher) and inserted into modified pcDNA5/FRT/TO vectors harbouring 3c cleavage sites.

Mammalian cell culture, lentivirus packaging, lentivirus infection and cell line generation

K562 (myelogenous leukaemia lymphoblast line from the American Type Culture Collection (ATCC)) were maintained in suspension between 2×10^5 and 1×10^6 cells per ml in RPMI medium supplemented with 2 mM glutamine and 10% FBS (Sigma-Aldrich). K562 cells stably expressing spCas9 were a gift from the Bassik Laboratory (Stanford University). HEK293 human embryonic kidney cells and HEK293T cells (ATCC) were grown and maintained in DMEM supplemented with 10% FBS (Sigma-Aldrich). All cell lines were grown in humidified incubators at 37 °C in 5% CO_2 and tested for mycoplasma bacteria by PCR using a kit from ABM according to the manufacturer's instructions.

UFL1^{KO} HEK293 cells were generated by CRISPR knock-in of a stop cassette and puromycin resistance gene in a donor plasmid co-transfected with a p×330 plasmid (Zhang Laboratory) carrying the sgRNA protospacer: CCAGCGGGCGCAGTTCGCCG. Cells were selected with puromycin starting about 3 days after transfection for around 5 days before single colony selection for clonal knockout lines. *UFL1* knockout was verified by western blotting. N-terminal mini-Turbo[10] *UFM1* knock-in cells were similarly generated in U2OS cells with wild-type, *UFSP2*^{KO} or *UBA5*^{KO} cells[2]. A p×330 plasmid with the protospacer sequence GAGCGGGAGAGAGTCAGGGT was co-transfected with a donor plasmid containing homology arms for UFM1 to insert the puromycin-resistance gene followed by a P2A skip sequence and the mini-Turbo tag directly following the endogenous *UFM1* start codon. Transfected cells were selected for puromycin resistance followed by clonal selection by limited dilution. Clonal lines with homozygous knock-in of the mini-Turbo tag were tested by western blots against UFM1 to ensure knock-in, competent conjugation to uL24 (for wild-type and *UFSP2*^{KO} backgrounds) and response to limited (200 nM) anisomycin treatments. Clones were further analysed for a lack of core glycosylated CD147 stabilization[2] and mini-Turbo activity.

Lentivirus used to produce stable cell lines and K562 knockout lines was generated through transfection of HEK293T cells with second-generation plasmids (pxPAX2, pMD2.G and pLVX expression vector) or third-generation plasmids (pRSV, pMDL, pVSVG and pMCB320 sgRNA expression vectors) using *Trans*IT-LT1 transfection reagent (Mirus) according to the manufacturer's instructions and grown for 72 h before collection of the viral supernatant. Supernatant (medium) containing the viral particles was collected and filtered through a 0.45 μm syringe filter and frozen at −80 °C until use. Infections of K562 cells were performed by spin transduction; cells were resuspended in viral supernatant containing 8 μg ml^{-1} polybrene and centrifuged at 1,000*g* for 2 h at 33 °C. Viral supernatant was removed and cells were resuspended in fresh RPMI (+10% FBS) and grown for about 72 h before selection with puromycin for CRISPR-mediated *UFSP2* or *UFM1* knockout lines. *UFSP2* and *UFM1* knockout K562 clonal lines were isolated by limited dilution. Stable UFL1–Flag-expressing HEK293 cells were generated through the lentiviral transduction of *UFL1*^{KO} cells (described above) by the dilution of lentiviral supernatant into the medium containing freshly trypsinized and plated cells (about 100,000) in the presence of 10 μg ml^{-1} polybrene. HEK293 cells were incubated with virus for 2–3 days before removing the viral supernatant and selection with blasticidin for stable UFL1–Flag-expressing cells.

HEK293 Flp-In TREx (Thermo Fisher) cells were grown to 50% confluency before transfection of 0.5 μg pcDNA5/FRT/TO vector containing N-terminally 3×Flag-tagged UFM1 or C-terminally 3×Flag-tagged UFL1 and 4.5 μg pOG44 (Thermo Fisher) by 20 μg polyethyleneimine. At 24 h following transfection, cells were split into 10 cm plates and selected using 10 μg ml^{-1} blasticidin and 150 μg ml^{-1} hygromycin B.

mT–UFM1 sample preparation and MS analysis

Five biological replicates of mT–UFM1 and *UBA5*^{KO} mT–UFM1 U2OS cells, and a single replicate of U2OS cells were prepared for mT-mediated proximity labelling experiments. Four 15 cm plates were grown for each replicate to 80–90% confluency. Cells were treated with 50 μM of biotin for 4 h, removed from the 37 °C incubator and washed 4 times with 15 ml ice cold 1× PBS, scraped from plates into 15 ml conical tubes and spun at 800*g* for 5 min to pellet cells. Cells were lysed in 350 μl RIPA buffer (50 mM Tris pH 7.5, 150 mM NaCl, 0.5% sodium deoxycholate, 0.1% SDS and 1% NP-40), incubated on ice for 15 min and centrifuged at 21,000*g* for 10 min. Clarified supernatant (lysate) was transferred to a new 1.5 ml microcentrifuge tube and frozen in liquid nitrogen for future sample preparation. Samples were thawed in cool water and placed directly on ice, buffer-exchanged into RIPA buffer using PD10 columns (GE Healthcare) according to the manufacturer's instructions to reduce residual biotin. Biotinylated proteins were then processed as previously described[37]. In brief, lysate was normalized and 3.4 mg was incubated with 30 μl Pierce magnetic streptavidin beads (Thermo Fisher, 88816) pre-equilibrated in RIPA buffer overnight rotating at 4 °C. Using a magnetic microcentrifuge holder, RIPA buffer was removed, and beads were washed twice with 1 ml of RIPA buffer, twice with 1 ml of 2% SDS in 50 mM HEPES, twice with 1 ml of 3 M urea in 50 mM HEPES, once with 1 ml of 0.1 M sodium bicarbonate, two more times with 1 ml RIPA buffer and twice with 1 ml of water. Captured protein was eluted from streptavidin beads by the addition of 100 μl of 1,1,1,3,3,3-hexafluoro-2-propanol (HFIP; Millipore Sigma, 52517) and incubation at room temperature for 5 min while mixing. HFIP eluate was transferred to a new tube, and the process was repeated for a total of 200 μl of HFIP eluate. Samples were dried in a SpeedVac and frozen dry for future processing. Samples were resuspended in 50 μl, 6 M urea and 100 mM EPPS, pH 8.5. Trypsin (1 μg) was added to samples and the digest was incubated at 37 °C for 6 h. Biotinylated peptides were captured using streptavidin beads and supernatant was collected for downstream processing. TMT labelling of each sample was performed by adding 5 μl of the 20 ng ml^{-1} stock of TMT reagent along with acetonitrile to achieve a final acetonitrile concentration of approximately 30% (v/v). Following incubation at room temperature for 1 h, the reaction was quenched with hydroxylamine to a final concentration of 0.5% (v/v) for 15 min. The TMT-labelled samples were pooled together at a 1:1 ratio. The sample was vacuum centrifuged to near dryness and subjected to C18 solid-phase extraction (Sep-Pak, Waters). The sample was then fractionated according to manufacturer's instructions using a high pH reversed-phase peptide fractionation kit (Thermo Fisher Scientific) for a final six fractions and subjected to C18 StageTip desalting before MS analysis.

MS data were collected using an Orbitrap Fusion Lumos mass spectrometer (Thermo Fisher Scientific) coupled to a Proxeon EASY-nLC1200 liquid chromatography pump (Thermo Fisher Scientific). Peptides were separated on a 100 μm inner diameter microcapillary column packed in-house with about 35 cm of Accucore150 resin (2.6 μm, 150 Å, Thermo Fisher Scientific) with a gradient consisting of 5–15% (0–70 min), 15–20% (70–85 min) acetonitrile and 0.1% formic acid over a total 95 min run at about 500 nl min^{-1}. For analysis, we loaded 1/3 of each fraction onto the column. Each analysis used

the Multi-Notch MS^3-based TMT method[38] to reduce ion interference compared with MS^2 quantification[39], combined with the FAIMS Pro Interface (using previously optimized 3 CV parameters for TMT multiplexed samples[40]) and combined with newly implemented Real Time Search analysis software[41,42]. The scan sequence began with a MS^1 spectrum (Orbitrap analysis; resolution of 120,000 at 200 Th; mass range of 400–1,600 *m/z*; automatic gain control (AGC) target of 8×10^5; and maximum injection time of 100 ms). Precursors for MS^2 analysis were selected using a cycle type of 1.25 s CV^{-1} method (FAIMS CV = −40/−60/−80). MS^2 analysis consisted of collision-induced dissociation (quadrupole ion trap analysis; rapid scan rate; AGC of 1.0×10^4; isolation window of 0.7 Th; normalized collision energy (NCE) of 35; maximum injection time of 35 ms). Monoisotopic peak assignment was used, and previously interrogated precursors were excluded using a dynamic window (150 s ± 10 ppm). Following acquisition of each MS^2 spectrum, a synchronous-precursor-selection API-MS^3 scan was collected on the top ten most intense ions *b* or *y* ions matched by the online search algorithm in the associated MS^2 spectrum[41,42]. MS^3 precursors were fragmented by high energy collision-induced dissociation and analysed using the Orbitrap (NCE of 65; AGC of 2.5×10^5; maximum injection time of 300 ms; and resolution of 50,000 at 200 Th).

Mass spectra were processed using a COMET-based in-house software pipeline. MS spectra were converted to mzXML using a modified version of ReAdW.exe. Database searching included all entries from the human UniProt database. This database was concatenated with one composed of all protein sequences in the reversed order. Searches were performed using a 50 ppm precursor ion tolerance and the product ion tolerance was set to 0.9 Da. Enzyme specificity was assigned as trypsin. TMT tags on lysine residues and peptide N termini (+229.163 Da) and carbamidomethylation of cysteine residues (+57.021 Da) were set as static modifications, whereas oxidation of methionine residues (+15.995 Da) was set as a variable modification. Peptide-spectrum matches (PSMs) were adjusted to a 1% FDR[43,44]. PSM filtering was performed using a linear discriminant analysis as previously described[45] while considering the following parameters: XCorr, peptide length, ΔCn, charge state, missed cleavages and mass accuracy of the precursor. For TMT-based reporter ion quantitation, we extracted the summed signal-to-noise ratio for each TMT channel and found the closest matching centroid to the expected mass of the TMT reporter ion (integration tolerance of 0.003 Da). Reporter ion intensities were adjusted to correct for the isotopic impurities of the different TMT reagents according to the manufacturer's specifications. Proteins were quantified by summing reporter ion signal-to-noise measurements across all matching PSMs, producing a 'summed signal-to-noise' measurement. PSMs with poor quality, MS^3 spectra with more than 5 TMT reporter ion channels missing or isolation specificity less than 0.7, or with TMT reporter summed signal-to-noise ratios that were less than 140 or had no MS^3 spectra were excluded from quantification. Protein or peptide quantification values were exported for further analysis in Microsoft Excel and Perseus (v.1.5.3.2)[46]. Supplementary Table 1 lists all quantified proteins and associated TMT reporter ratio-to-control channels used for quantitative analysis. Annotations for ER protein markers were assembled using the proteins that had scored with confidence 'very high' or 'high' from a previously published HeLa dataset[47] and additional entries from manually curated literature.

UFM1 pull-downs, sample processing and MS

UFSP2 and *UFM1* double-knockout cells were transfected with UFM1 (amino acids 1–83; control) or SBP-tagged UFM1 with a HC3 protease cleavage site and linker. At 24 h after transfection, cells were washed with PBS, collected and lysed in a buffer containing 20 mM Tris pH 7.5, 100 mM NaCl, 10 mM $MgCl_2$ and 1% decyl maltose neopentyl glycol (DMNG) supplemented with EDTA-free complete protease inhibitors (Roche), 0.5 mM TCEP, RNaseOUT (Thermo Fisher) and 1 mM phenylmethylsulfonyl fluoride (PMSF) on ice for 10 min. Lysate was clarified by centrifugation at 21,000*g* for 10 min at 4 °C three times. Clarified lysate was layered on top of 1 M sucrose cushion solution (20 mM Tris pH 7.5, 100 mM NaCl, 10 mM $MgCl_2$, 1 % DMNG and 1 M sucrose) for sucrose cushion sedimentation at 100,000 r.p.m. in a TLA100.2 rotor at 4 °C for 1 h. The resulting pellet, containing crude ribosomes, was resuspended in lysis buffer after briefly washing the pellet with cold lysis buffer lacking DMNG. Resuspension was carried out by mechanically breaking the pellet and transferring it to a microcentrifuge tube using a pipette (P200), followed by mixing at 4 °C and additional mixing at 37 °C. Insoluble material was pelleted at 21,000*g* at 4 °C, and the supernatant was incubated with Dynabeads MyOne Streptavidin T1 beads pre-equilibrated in lysis buffer for 4 h at 4 °C rotating end-over-end. The flowthrough (unbound supernatant) was discarded and beads were washed 5 times with lysis buffer with low DMNG (0.02%). Elution buffer (50 mM Tris about pH 7.5, 75 mM NaCl, 10 mM $MgCl_2$, 1 mM EGTA and 30 mM biotin) was added to the beads and the mixture was mixed at 37 °C for 30 min to elute proteins. Eluate was processed by trichloroacetic acid (TCA) precipitation for MS analysis (see below).

Proteins were extracted with 100% TCA to a final volume of 25% TCA and incubated overnight. The proteins were precipitated by centrifugation at 14,000 r.p.m. for 10 min. TCA precipitation was followed by 3 washes with 1 ml of ice-cold methanol. The precipitated pellet was dried in a SpeedVac and resuspended in 50 µl, 200 mM EPPS, pH 8.0, and 0.5 µg of LysC (Wako, 129-02541) and the sample was incubated at room temperature overnight while shaking. Then, 1 µg of trypsin was added and the digest was incubated at 37 °C for 6 h. The sample was acidified and desalted using a StageTip[48].

MS data were collected using a Exploris 480 mass spectrometer (Thermo Fisher Scientific) coupled with a Proxeon 1000 liquid chromatograph (Thermo Fisher Scientific). Peptides were separated on a 100 µm inner diameter microcapillary column packed with about 30 cm of Accucore C18 resin (2.6 µm, 150 Å, Thermo Fisher Scientific). We loaded about 1 µg onto the column.

Peptides were separated using a 1 h gradient of 0–28% acetonitrile in 0.125% formic acid with a flow rate of about 550 nl min^{-1}. The scan sequence began with an Orbitrap MS^1 spectrum with the following parameters: resolution of 60,000, scan range of 350–1,200 Th, AGC target of 300%, maximum injection time of 25 ms, RF lens setting of 40%, and centroid spectrum data type. We selected the top 20 precursors for MS^2 analysis, which consisted of high-energy collision dissociation with the following parameters: resolution of 30,000, AGC was set at standard, maximum injection time of 60 ms, isolation window of 1.2 Th, NCE of 28, and centroid spectrum data type. In addition, unassigned and singly charged species were excluded from MS^2 analysis and dynamic exclusion was set to 60 s.

Mass spectra were processed using a COMET-based in-house software pipeline. MS spectra were converted to mzXML using a modified version of ReAdW.exe. Database searching included all entries from the human UniProt database. This database was concatenated with one composed of all protein sequences in the reversed order. Searches were performed using a 50 ppm precursor ion tolerance and the product ion tolerance was set to 0.03 Da. Enzyme specificity was assigned as trypsin. Oxidation of methionine residues (+15.995 Da) was set as a variable modification. PSMs were adjusted to a 1% FDR[43,44]. PSM filtering was performed using a linear discriminant analysis, as previously described[45] while considering the following parameters: XCorr, peptide length, ΔCn, charge state, missed cleavages and mass accuracy of the precursor. Figure 1c displays proteins that have at least five spectral counts and is enriched at least tenfold over the untagged UFM1 control pull-down. Supplementary Table 2 shows all proteins identified in this pull-down.

Cell fractionation

Sequential detergent fractionations were performed as previously described[2]. In brief, K562 cells were collected, washed with PBS and

resuspended in permeabilization buffer (0.02% digitonin, 25 mM HEPES-KOH pH 7.5, 100 mM NaCl and 10 mM $MgCl_2$) supplemented with EDTA-free complete protease inhibitors (Roche), 0.5 mM TCEP, RNaseOUT (Thermo Fisher) and PMSF. Permeabilization was carried out for 5 min on ice before centrifugation for 5 min at 20,000*g* and 4 °C. The resulting supernatant was collected as the cytosolic fraction. The pellet was briefly washed by gently resuspending in an equal volume of 25 mM HEPES-KOH pH 7.5, 100 mM NaCl and 10 mM NaCl and centrifugation at 8,000*g* for 5 min at 4 °C. The supernatant was discarded and the pellet was subsequently resuspended in an equal volume of lysis buffer (25 mM HEPES-KOH pH 7.5, 100 mM NaCl, 10 mM $MgCl_2$ and 0.5% Triton X-100 or 1% DMNG for membrane polysome profiles and sucrose cushion sedimentation for E3-ribosome binding measurements), incubated for 5 min on ice and centrifuged at 20,000*g* for 5 min at 4 °C. The resulting supernatant contained the membrane fraction. HEK293 cells were processed with the same protocol above, but with reduced digitonin (reduced to 0.015%) in the initial permeabilization step.

Sucrose gradient sedimentation

K562 suspension cells were treated before polysome profiling. Cells were collected into 15 ml Falcon tubes on ice and supplemented with 200 μg ml^{-1} cycloheximide at the time of collection. Cell suspensions were centrifuged at 800*g* for 5 min at 4 °C, resuspended in PBS containing 100 μg ml^{-1} cycloheximide and centrifuged again at 800*g* for 5 min to wash cells. Cells were then lysed on ice in polysome lysis buffer containing 25 mM HEPES-KOH pH 7.5, 100 mM NaCl, 0.5 mM TCEP, 10 mM $MgCl_2$ and 1% DMNG supplemented with EDTA-free complete protease inhibitors (Roche), 0.5 mM TCEP, RNaseOUT (Thermo Fisher) and 1 mM PMSF. Lysate was mixed on ice for 10 min then spun to clarify at 21,000*g* for 10 min (at 4 °C) before layering onto a linear 10–50% sucrose gradient (buffered with 25 mM HEPES-KOH pH 7.5 and containing 100 mM NaCl, 10 mM $MgCl_2$ and 0.02% DMNG). For polysome profiles of in vitro UFMylation reactions and purified ribosome subunits, the same 10–50% gradients were generated in buffers without DMNG.

After samples were layered on gradients, centrifugation was carried out at 41,000 r.p.m. in a SW41Ti rotor at 4 °C for 90 or 110 min and fractionated using a piston fractionator (Biocomp) affixed with a Triax UV detector and flow cell. Collected fractions were stored on ice or frozen and stored at −80 °C until further processing. Sucrose gradient fractions were precipitated using TCA before analysis by immunoblotting. Sodium deoxycholate was added to each sample to a concentration of 0.02% before precipitation with a final concentration of ice-cold TCA of 10%. Samples were incubated at −20 °C for 1 h or overnight, protein was pelleted at 21,000*g* at 4 °C for 30 min and washed with ice cold acetone, and centrifuged again at 21,000*g* at 4 °C for 30 min. The supernatant was removed, the protein pellet was dried at room temperature overnight and resuspended in 1× Laemmli sample buffer for immunoblot analysis.

E3(UFM1)–ribosome co-sedimentation analysis

For UFL1–Flag replacement lines, cells stably expressing C-terminally tagged 3×Flag-tagged UFL1 (and variants thereof) were grown to around 80% confluency in 10 cm plates, washed 3 times with 5 ml of ice cold 1× PBS and collected by scraping into 10 ml of 1× PBS. Cells were pelleted at 800*g* for 5 min at 4 °C and the supernatant was discarded. Cells were then resuspended in 0.5 ml of sucrose cushion lysis buffer (25 mM HEPES-KOH pH 7.5, 100 mM NaCl, 10 mM $MgCl_2$ and 1% DMNG supplemented with 1 mM PMSF, 100 μg ml^{-1} cycloheximide, EDTA-free complete protease inhibitors (Roche), 0.5 mM TCEP and RNaseOUT) incubated on ice for 10 min and centrifuged for 10 min at 21,000*g* at 4 °C to clarify the lysate. The supernatant was collected and clarified again by centrifugation at 21,000*g* at 4 °C. Clarified lysate (400 μl) normalized for total protein concentration using a BCA assay was layered onto a sucrose cushion composed of 1 M sucrose, 25 mM HEPES-KOH pH 7.5, 100 mM NaCl, 10 mM $MgCl_2$ and 0.2% DMNG supplemented with 1 μg ml^{-1} cycloheximide, 0.5 mM TCEP and centrifuged at 100,000 r.p.m. in a TLA100.2 rotor for 1 h at 4 °C. The supernatant was removed and crude ribosome pellets were washed with 200 μl of sucrose cushion wash buffer (25 mM HEPES-KOH pH 7.5, 100 mM NaCl and 10 mM $MgCl_2$) before resuspension in 1× Laemmli sample buffer for immunoblot analysis.

DDRGK1^{KO} HEK293 cells were grown to about 80% confluency in 6-well plates and transfected with 2 μg pLVX plasmids containing C-terminally 3×Flag-tagged wild-type or mutant DDRGK1 with Lipofectamine 3000 (Thermo Fisher) according to the manufacturer's instructions. Cells were split 24 h later into 2 wells of a 6-well plate and transfected again with 2 μg of DNA as described above at 48 h after initial transfection. At 20 h later, cells were washed 3 times with 2 ml of 1× PBS supplemented with 100 μg ml^{-1} cycloheximide, scraped and collected into 1 ml of 1× PBS (with 100 μg ml^{-1} cycloheximide) and pelleted at 500*g* for 5 min at 4 °C. For measurements of E3 association, cells were treated with 200 nM anisomycin for 1 h to enhance the low-level E3–ribosome association in HEK293 cells, lysed in 175 μl of sucrose cushion lysis buffer and pelleted as described above using a sucrose cushion of 250 μl in a TLA100.1 rotor with 150 μl of cell lysate. Crude ribosome pellets were washed as above, but with 100 μl of wash buffer, and resuspended in 1× Laemmli sample buffer for immunoblot analysis. Pelleting of E3-associated ribosomes was performed three times (biological triplicate), and the mean and standard deviations (error bars) are depicted in Extended Data Fig. 1l.

For experiments in which wild-type or *DDRGK1*^{KO} HEK293 cells were fractionated before sucrose pelleting, the cells suspended in PBS were split in equal volumes for WC and fractionation samples before lysis. The WC cells were treated as described above. Fractionated samples were fractionated by sequential detergent extraction as described above. Equal volumes of each fraction or WC lysate were layered on top of the 1 M sucrose cushion as above, pelleted and analysed by immunoblot analysis.

Ribosome–translocon association analysis

HEK293 wild-type, *UFC1*^{KO} and *UFM1*^{KO} cells grown to about 80% confluency in 6-well plates were treated with 5 μg ml^{-1} puromycin or 3.75 μM harringtonine for the indicated time points. Cells were washed once with 1 ml of ice cold 1× PBS and collected by pipetting in 1.5 ml of 1× PBS. Cells from two wells were used for each condition. Cells were pelleted at 800*g* for 5 min at 4 °C and the supernatant was discarded. Cells were then resuspended in 0.5 ml of Triton lysis buffer (25 mM HEPES-KOH pH 7.5, 100 mM NaCl, 1% Triton X-100) supplemented with 1 mM PMSF, EDTA-free complete protease inhibitors (Roche) and 1 μM dithiothreitol (DTT), incubated on ice for 10 min and centrifuged for 10 min at 21,000*g* at 4 °C to clarify the lysate. Clarified lysate (500 μl) normalized for total protein concentration using a BCA assay was layered onto a sucrose cushion composed of 1 M sucrose, 25 mM HEPES-KOH pH 7.5, 100 mM NaCl, with 1 mM PMSF, EDTA-free complete protease inhibitors (Roche) and 1 μM DTT, and centrifuged at 100,000 r.p.m. in a TLA100.2 rotor for 1 h at 4 °C. The supernatant was removed and crude ribosome pellets were washed with 200 μl of ice-cold H_2O before resuspension in 1× Laemmli sample buffer for immunoblot analysis.

Preparation of salt-resistant 80S ribosomes

K562 cells at a density of about 1.5×10^6 cells per ml were treated with 2 μg ml^{-1} harringtonine for 30 min. Cells were pelleted at 1,000*g* for 5 min at 4 °C, resuspended in 35 ml of PBS (containing 100 μg ml^{-1} cycloheximide) and pelleted again at 1,000*g*. The wash was repeated and the cells were lysed in 1 ml of a Triton lysis buffer (20 mM HEPES-KOH pH 7.5, 250 mM KCl, 15 mM $MgCl_2$ and 1% Triton X-100 supplemented with 1 mM PMSF, 0.5 mM TCEP, EDTA-free complete protease inhibitors (Roche) and RNaseOUT) for 10 min on ice. Lysate was clarified at 8,000*g* for 10 min at 4 °C and layered onto a 10–50% sucrose gradient

and fractionated as described above. Fractions containing the 80S ribosomes were pooled and pelleted by sucrose cushion sedimentation as described above in a TLA100.2 rotor. Pelleted 80S ribosomes were resuspended in 25 mM HEPES-KOH pH 7.5, 50 mM KCl, 15 mM $MgCl_2$ and 0.5 mM TCEP for in vitro UFMylation reactions.

In vitro UFMylation

In vitro UFMylation of ribosomes was performed as previously described[6]. In brief, the purified UFMylation cascade was mixed and incubated with ribosomes with 1 µM UBA5, 1 µM UFC1, 2 µM UFM1, 100 nM UFL1–DDRGK1 complex, 200 nM CDK5RAP3 and 50 nM purified 60S ribosomes in 25 mM HEPES-KOH pH 7.5, 50 mM KCl and 15 mM $MgCl_2$. A 100 mM stock of ATP was made fresh in 50 mM HEPES-KOH pH 7.5, with the pH adjusted to about pH 7.0 with sodium bicarbonate, and added to a final concentration of 5 mM. Samples were then incubated at 35 °C for the indicated times and quenched by the addition of Laemmli sample buffer or placed on ice to halt the reaction before further analysis. Reactions performed on 60S in the presence of competing, salt-resistant 80S ribosomes were performed with a 2-fold molar excess of 80S over 60S ribosomes. In vitro UFMylation reactions used to prepare samples for cryo-EM were performed similarly as above with 0.5 µM UBA5, 1 µM UFC1, 21 µM UFM1, 250 nM UFL1–DDRGK1 complex, 300 nM CDK5RAP3 and 200 nM purified 60S ribosomes in 25 mM HEPES-KOH pH 7.5, 50 mM KCl and 10 mM $MgCl_2$ and 5 mM ATP and incubated for 15 min at 35 °C. UFMylated ribosomes were centrifuged at 21,000*g* for 5 min at 4 °C and plunge frozen on cryo-EM grids within about 1 h (see below).

AP accumulation assay

Rescue experiments were performed by subjecting *DDRGK1*^{KO} HEK293 cells to two rounds of transfection with 2 µg of rescue plasmids (that is, DDRGK1 WT, DDRGK1 UFIM(mt), DDRGK1 ΔEBM) for 72 h, similarly to the *DDRGK1*^{KO} rescue experiments described above. The ribosome stalling reporter SS^{VgV} (ref. 4) (0.5 µg of plasmid DNA) was co-transfected with DDRGK1 rescue plasmids at the same time as the second DDRGK1 transfection (24 h before cell collection). WC lysates were prepared in RIPA lysis buffer (50 mM Tris pH 7.6, 150 mM NaCl, 1% NP-40, 0.5% sodium deoxycholate and 0.1% SDS) with protease inhibitor cocktail (complete, EDTA-free protease inhibitor cocktail; Roche) and 1 mM PMSF. The total protein concentration was determined for each sample using a Pierce BCA Protein Assay kit (23225). Normalized samples were analysed by SDS–PAGE and Flag immunoblotting to detect AP produced by SS^{VgV}. Five biological replicates were performed; bar graphs in Fig. 4i show the mean and standard deviation and significance determined using Dunnett's one-way ANOVA.

Protein purification

Mouse UFSP1 was purified as previously described[49] from a pet28a vector with a C-terminal His tag using a step gradient of imidazole to elute from Ni-NTA agarose (Qiagen) followed by dialysis and subsequent concentration to 100 µM in 20 mM HEPES (pH 7.5), 100 mm NaCl and 2 mM DTT. Aliquots were frozen in liquid nitrogen and stored at −80 °C for future use. UFL1–DDRGK1, CDK5RAP3, UFC1, UBA5 and UFM1 were purified as previously described[6].

Affinity purification of UFM1 and UFL1-bound ribosomes for cryo-EM

HEK293 FlpIn TRex cells were grown to 50% confluency and protein expression of Flag–UFM1 or Flag–UFL1 was induced by tetracycline (1 µg ml^{-1}). At 22 h following induction, cells were collected and washed twice with PBS by centrifugation at 127*g* for 10 min. Cells were then resuspended in lysis buffer (150 mM potassium acetate, 20 mM HEPES pH 7.5, 5 mM $MgCl_2$, 5% glycerol, 3% GDN, 1 mM DTT, 0.5 mM NaF, 0.1 mM Na_3VO_4 and complete EDTA-free protease inhibitor (Roche)) and lysed by sonicating 4 × 10 s with 20 s on ice in between (Branson Sonifier 250). The lysate was clarified by centrifugation at 3,166*g* for 15 min and at 36,603*g* for 20 min then incubated with M2 anti-Flag agarose beads (Sigma-Aldrich) on a rotating wheel for 120 min at 4 °C. Beads were washed twice with washing buffer (150 mM potassium acetate, 20 mM HEPES pH 7.5, 5 mM $MgCl_2$, 0.1% GDN, 1 mM DTT, 0.5 mM NaF, 0.1 mM Na_3VO_4 and complete EDTA-free protease inhibitor (Roche)), then once more using final buffer (150 mM potassium acetate, 20 mM HEPES pH 7.5, 5 mM $MgCl_2$, 1 mM DTT and 0.1% GDN). Beads were transferred onto a 1 ml Mobicol (MoBiTec) and washed with 5 ml final buffer, then incubated with final buffer containing 40 µg 3C protease for 60 min at 4 °C. The eluate was collected by centrifugation and utilized further for single particle cryo-EM and NuPAGE gel electrophoresis.

Flag–UFL1 purification was performed similarly, with a couple of differences. The lysis buffer was supplemented with 1% digitonin instead of 3% GDN, and, following elution with 3C protease, the ribosomes were pelleted through a sucrose cushion (20 mM HEPES pH 7.5, 150 mM potassium acetate, 5 mM $MgCl_2$, 0.1% GDN and 1 M sucrose) by centrifugation at 100,000 r.p.m. for 1 h using a TLA 120.2 rotor, after which the pellet was resuspended in final buffer.

EM and image processing

For the Flag–UFM1 pull-down, 3.5 µl of sample was applied to Quantifoil R3/3 holey carbon grids with 2 nm continuous carbon coating, blotted for 3 s then plunge frozen in liquid ethane using a Vitrobot Mark IV. Data collection was performed at 300 keV using a Titan Krios equipped with a K2 Summit direct electron detector using Smart EPU software v.2.12.1 and v.3.3.1 (Thermo Fisher) at a pixel size of 1.045 Å and a defocus range of −0.5 to −3.5 µm. Gain correction, alignment, and summation of movie frames was performed using MotionCor2 (v.1.4.0)[50] (1.16 e^- per Å^2 dose per frame). Contrast transfer function (CTF) parameters were estimated using CTFFIND4 (v.1.13)[51] and GCTF (https://www2.mrc-lmb.cam.ac.uk/download/gctf/)[52]. The quality of the collected micrographs was manually assessed.

For the Flag–UFM1 dataset, a total of 11,658 micrographs were selected. Particle picking was performed using crYOLO (v.1.7.6)[53]. A total of 616,046 particles were picked, which then underwent two rounds of 2D classification in cryoSPARC (v.3.2)[54]. This produced a total of 83,447 high-quality 60S particles and a minor subset of 80S particles (<10,000 particles). Brief analysis of the 80S subset revealed these to be previously published inactive ribosomes featuring eEF2–SERBP1 and EBP1 (ref. 55) and were not processed further. The 60S was consensus refined in RELION (v.3.1.1)[56], followed by CTF refinement. 3D focused classification was performed using a soft mask, focusing on the regions harbouring non-ribosomal density for the E3(UFM1) complex (spanning from the A, P and E sites down to uL24 and continuing further towards the ribosomal exit tunnel). This revealed one stable class consisting of 14,144 particles (16.9% of all 60S particles) that was refined to an average resolution of 3.1 Å. A schematic representation of the refinement and particle sorting process is provided in Extended Data Fig. 3a.

For the Flag–UFL1 pull-down, 3.5 µl of sample was applied to Quantifoil R3/3 holey carbon grids with 2 nm continuous carbon coating, blotted for 3 s then plunge frozen in liquid ethane using a Vitrobot Mark IV. Data collection was performed at 300 keV using a Titan Krios equipped with a SelectrisX Energy Filter and a Falcon4i direct electron detector at a pixel size of 0.727 Å and a defocus range of −0.5 to −3 µm and 60 e^- per Å total dose. Gain correction, alignment and summation of movie frames was performed using MotionCor2 (ref. 50) with 20 EER frames grouped into one fraction, producing 60 fractions with 1 e^- per Å dose per fraction. CTF parameters were estimated using CTFFIND4 (ref. 51) and GCTF[52].

A total of 50,993 micrographs were selected. Particle picking was performed in RELION (v.4.0.1)[57], resulting in a total of 3,017,721 particles. 2D classification in RELION (v.4.0.1) using the VDAM algorithm produced a total of 1,247,589 ribosomal particles. 3D classification with a soft mask around the 40S ribosomal subunit revealed a number of

60S classes with non-ribosomal density, as well as inactive 80S–eEF2–SERBP1–EBP1 complexes[55]. The 60S particles were further classified with a mask focusing around the A and P sites, which further revealed a small subpopulation of 60S corresponding to a biogenesis intermediate harbouring LSG1, NMD3 and ZNF622 (ref. 58). The remaining particles were sorted with a mask focusing around the tunnel exit. This revealed three major classes: one with SEC61 bound to the exit, another featuring the α-helix of DDRGK1 extending towards the tunnel exit and a final one with EBP1 bound to the tunnel exit. The EBP1 population consisted of empty 60S subunits. The population featuring DDRGK1 was processed further with focused classification around the E3 complex used to sort out bad particles. This produced a 3 Å final reconstruction corresponding to the entire E3 similar to the ones obtained from the Flag–UFM1 and in vitro datasets, which was dubbed as state 3. For the SEC61-bound 60S, focused classification around H25ES7 and uL24 (around the expected location of UFM1) revealed two states: one with UFL1 partially bound (referred to as state 1) and a second one with the E3 complex bound and uL24 modified, but with the α-helix of DDRGK1 delocalized (state 2). A final round of classification was done for state 1 in cryoSPARC (v.4.2) using 3D classification with a focused mask around SEC61. The final particles produced a reconstruction of 3.27 Å. 3D variability analysis in cryoSPARC was used to sort out bad particles for state 2, and the final subset produced a resolution of 3.33 Å. CTF refinements and final refinements of all states were performed with RELION (v.4.0.1). A schematic representation of the refinement and particle sorting process is provided in Extended Data Fig. 7.

For in vitro UFMylated ribosomes, 2.5 µl of sample was applied to glow-discharged copper 200 mesh R1.2/1.3 ultrathin continuous carbon grids from Quantifoil, blotted for 3 s at 4 °C and 100% humidity, and plunge frozen in liquid ethane using a Vitrobot Mark IV (Thermo Fisher). Data collection was performed at the Stanford-SLAC Cryo-EM Center (S^2C^2) on a Titan Krios G3i at 300 kV equipped with a K3 detector with a pixel size of 0.86 Å per pixel, a defocus range of −0.8 to −2.0 µm and a dose per frame of 0.8 e^- per $Å^2$. Gain correction, alignment and summation of movie frames was performed using RELION (v.3.1.1) MotionCor implementation. CTF parameters were estimated using GCTF. A total of 10,692 micrographs were selected. 2D classification in cryoSPARC produced 846,919 ribosomal particles. Focused classification in RELION (v.3.1.1) around the 40S subunit to separate 80S and 60S revealed a 60S class with non-ribosomal density (for the E3(UFM1) complex), 60S classes with and without E-site tRNA bound and two classes representing empty 80S ribosomes. For the first 60S class, using a soft mask focusing on regions where non-ribosomal extra density was observed, one stable class consisting of 35,935 particles (4.6% of all particles) was isolated representing the stable 60S–UFM1-E3(UFM1) complex. This class was refined to an average resolution of 2.9 Å. A schematic representation of the refinement and particle sorting process is provided in Extended Data Fig. 3b.

All consensus refinement maps were post-processed using DeepEMhancer[59] and in some cases used for interpretation as indicated in the figure legends.

Model building and refinement

To generate a model for the 60S–UFM1–E3(UFM1) complex in the best resolved state (obtained from the UFL1-pull-down state 3 complex), a model for the human 60S (derived from 80S, PDB identifier 6Z6M)[55] was used as a template. First, the 60S subunit was rigid-body fitted into the density maps using ChimeraX[60] with the exception of the L1 stalk, which adopted a different conformation in the 60S–UFM1–E3(UFM1) complex. We therefore used the coordinates for the rRNA backbone of the L1 stalk from PDB code 8G5Y[61] as a starting point for modelling. Models for uL1 and eIF6 were used from the AlphaFold database (https://alphafold.ebi.ac.uk/) and real-space refined using Coot (v.0.9.8)[62]. The model of the complex formed by UFM1, DDRGK1, CDK5RAP3 and the N-terminal region of UFL1(1–389) was predicted using AlphaFold-Multimer[19] (Extended Data Fig. 5b) and a model for the UFL1 C-terminal region (480–794) was derived from AlphaFold 2 prediction[18].

The model of the E3(UFM1) complex was initially rigid-body fitted using the WH backbone of UFL1 and the GD2 and CC regions of CDK5RAP3 as a reference. The parts were then adjusted to fit into the density with Coot. For UFL1, the pWH and WH domains as well as parts of the CC regions could be fitted into the density map with high confidence, as a large number of aromatic and positively charged amino acid side chains were resolved below 3.5–4 Å in the corresponding regions (see Extended Data Fig. 4b for local resolution). For the CTD of UFL1, the local resolution of around 4 Å allowed us to fit the peptide backbone, whereas the region linking the CTD and the CC (M522–G532) as well as the distal region of the CTD (E722–E794) displayed lower local resolution (above 4.5 Å) and was therefore fitted as rigid-body only. For the disordered region bipartite CC domain of UFL1, we identified density accounting for a small helix and loop (residues 416–448) referred to as the 'PTC loop', which was fitted de novo. The conformation of the PTC rRNA bases U4452 and A4548 (stacks with Y443 of UFL1) was adjusted to account for the remodelling due to the PTC loop. No density was present for the rest of the disordered loop and only weak density was present for the N-terminal helix of UFL1 (M1–Q25) and the C-terminal tail of UFM1, suggestsing that these are flexible elements. These regions of E3(UFM1) were therefore omitted from the final model.

The GD2 of CDK5RAP3 and the adjacent parts of the CC helices were fitted by positioning several well-resolved bulky side chains. The overall local resolution in this region allowed for fitting a number of side chains with high confidence. The entire region below and adjacent to uL24, comprising UFM1, GD1 and adjacent CC helices of CDK5RAP3, displayed overall lower local resolution than the rest of the complex (between 4.5. and 7 Å) but still allowed clear assignment of secondary structure elements and thus rigid-body fitting of the respective AlphaFold models with only minor adjustments. The C-terminal pWH and WH domains of DDRGK1 were sufficiently resolved to fit bulkier side chains, particularly around the pWH interaction surface with the pWH of UFL1. The linker region of DDRGK1 between the C-terminal domain and long helical region (residues 196–208, the so called UFM1-interacting motif or UFIM) and β2 (18–24) of UFM1 were predicted to have a particularly interesting interaction in the form of a β-augmentation. In addition, the first three turns N-terminal of the UFIM that terminate the long α-helix projecting towards the tunnel exit were also predicted to be in close vicinity to UFM1 and interact with it. This structural detail was in agreement with our density with respect to general positioning despite the resolution being insufficient to verify interactions in molecular detail (Extended Data Fig. 6c).

rRNA was partially remodelled in regions interacting with the E3 ligase (H69, H38 and H25ES7). Here helices H69 and H38 could be fitted into the density map with high accuracy with the exception of the rRNA helix tips. Although we omitted the helix tip of H69, the one of H38 was modelled based on PDB 8GLP[61] and was fit into our density where applicable. The conformation of H25ES7 is altered in the presence of E3 ligase, however. Here resolution was insufficient for accurate modelling in state 3 (and state 2); therefore, the model was trimmed. In addition, we trimmed other regions of the rRNA, such as RNA loops and expansion segments, where the density was insufficient to enable accurate model placement. The C-terminal region of the ribosomal protein uL13 was fitted into the state 3 structure up to the last discernible amino acid (R195). Finally, for uL1, most amino acid side chains were resolved, allowing to fit an AlphaFold 2 model for uL1 with high confidence and refine it.

Models for partial 60S–E3(UFM1)-SEC61 complexes as described for state 1 and state 2 were derived from the state 3 model. Unambiguous identification of SEC61 was supported by the following results: (1) the presence of a typical micelle directly under the tunnel exit; (2) clear density at secondary structure resolution for the ribosome-interacting

C-terminal portion of the SEC61α subunit and for the SEC61γ subunit; and (3) visualization of the SEC61α ribosome-binding loop 8–9 and loop 6–7 adjacent to the tunnel exit (Extended Data Fig. 8). A model for the trimeric complex from dog in the closed state (PDB 6W6L[26]) was rigid-body fitted into the respective densities. The local resolution of SEC61α loops 6–7 and 8–9 was sufficient for fitting some of the bulkier side chains (Extended Data Fig. 8).

Following rigid-body fitting and real space refinement in Coot, the complete model was then refined using Phenix (v.1.12-4487)[63] and the Servalcat REFMAC5 pipeline[64]. Fine tuning of models (adjustment of rotamers, Ramachandran outliers and clashes) was performed using ISOLDE[65] in ChimeraX. At this point, we utilized the recently released model of the human 80S based on a 1.7 Å resolution map (PDB 8GLP[61]) to fine-tune the geometry of rRNA (phosphate-backbone conformation and sugar puckers) and ribosomal proteins of the core 80S ribosome. Model geometry was validated using Molprobity[66], and Phenix map to data cross-correlation was utilized to evaluate overall density fits. As a final step, for UFM1, the E3 ligase, as well as SEC61, occupancy of regions with insufficient side chain information in the final maps was set to zero. Model and density figures were generated in ChimeraX (v.1.6)[60,67].

DeUFMylation of ribosomes with UFSP1

DeUFMylation of ribosomes in *UFSP2*^{KO} K562 lysate and in vitro UFMylated 60S ribosomes was performed with UFSP1 or UFSP1 inactivated by NEM as follows. UFSP1 was incubated with or without a final concentration of 20 mM NEM on ice for 20 min. Buffer was then exchanged into 20 mM HEPES-KOH pH 7.5, 100 mM NaCl, 10 mM $MgCl_2$ and 1 mM TCEP using 0.5 ml Zeba 7 kDa (MWCO) 0.5 ml desalting columns (Thermo Fisher, 89882) according to the manufacturer's instructions. Clonal *UFSP2*^{KO} K562 cells were collected by centrifugation and washed twice with 10 ml of 1× PBS containing 100 μg ml^{-1} cycloheximide in a 15 ml Falcon tube by centrifuging at 655*g* for 4 min at 4 °C. Cells were lysed in 20 mM HEPES-KOH pH 7.5, 100 mM NaCl, 10 mM $MgCl_2$ and 0.5% Triton X-100 containing 1 mM PMSF, 2× RNaseOUT, 0.5 mM TCEP and 50 μg ml^{-1} cycloheximide for 10 min on ice, and clarified at 21,000*g* for 10 min at 4 °C. Lysate was then treated with 8 μM NEM-inactivated or active UFSP1 for 10 or 20 min at 37 °C while mixing, placed on ice to slow deUFMylation and immediately layered onto a 10–50% sucrose gradient for analysis by sucrose density sedimentation. A similar workflow was applied to in vitro prepared UFMylated ribosomes. UFMylated ribosomes were prepared as described above except that the reaction was quenched by addition of apyrase (Sigma Aldrich, A6237) at 5 U ml^{-1} and incubated on ice for 30 min. Active or inactivated UFSP1 was added to a final concentration of 8 μM and the sample was incubated at 37 °C for 20 min, placed on ice and immediately layered onto a 10–50% sucrose gradient for sucrose gradient sedimentation.

Co-essentiality network analysis

All essential UFMylation genes (*UFM1*, *UFC1*, *UBA5*, *DDRGK1*, *UFL1*, *CDK5RAP3*, *ODR4* and *UFSP1*) were used as input for the FIREWORKS interactive network tool[68] (https://mendillolab.shinyapps.io/fireworks/). UFM1 co-dependencies were obtained from the Broad Institute's DEPMAP portal (https://depmap.org/portal/) (23Q4 release).

Antibodies

The following antibodies were used in this article with the indicated dilutions: rabbit anti-UFM1, Abcam, ab109305, dilution, 1:1,000; mouse anti-UFSP2, Santa Cruz Biotechnology, sc-376084, dilution, 1:1,000; rabbit anti-UFC1, Abcam, ab189251, dilution, 1:2,000; rabbit anti-UBA5, Proteintech, 12093-1-AP, dilution, 1:2,000; rabbit anti-DDRGK1, Proteintech, 21445-1-AP, dilution, 1:1,000; rabbit anti-UFL1, Bethyl Laboratories, A303-456A, dilution, 1:2,000; rabbit anti-CDK5RAP3, Bethyl Laboratories, A300-870A, dilution, 1:2,000; rabbit anti-RPL26 (uL24), Abcam, ab59567, dilution, 1:3,000; mouse anti-RPL17 (C-8) (uL22), Santa Cruz Biotechnology, sc-515904, dilution, 1:2,000; rabbit anti-NEMF, Proteintech, 11840-1-AP, dilution, 1:2,000; rabbit anti-eIF6, Bethyl Laboratories, A303-029A, dilution, 1:2,000; mouse anti-Flag M2, Sigma-Aldrich F1804, dilution, 1:4,000; mouse anti-GAPDH clone D4C6R, Cell Signaling, 97166S, dilution, 1:5,000; rabbit anti-GAPDH clone 14C10, Cell Signaling, 2118, dilution, 1:5,000; IRDye 800CW streptavidin, LI-COR Biosciences, 925-32230, dilution, 1:5,000; rabbit anti-SEC61β, Gift from Hegde Laboratory, dilution, 1:2,000; rabbit anti-SEC61α, Gift from Hegde Laboratory, dilution, 1:1,000; anti-Mouse IgG, IRDye 800CW, LI-COR Biosciences, 926-32210, RRID: AB_621842, dilution, 1:20,000; anti-Mouse IgG, IRDye 680LT, LI-COR Biosciences, 926-68020, RRID: AB_10706161, dilution, 1:20,000; anti-Rabbit IgG, IRDye 800CW, LI-COR Biosciences, 926-32211, RRID: AB_621843, dilution, 1:20,000; anti-Rabbit IgG, IRDye 680LT, LI-COR Biosciences, 926-68021, RRID: AB_10706309, dilution, 1:20,000. Antibodies were validated as described in the Nature Portfolio Reporting Summary.

Statistics and reproducibility

All biochemical experiments, cell-based assays and in vitro assays, in part or in whole, were successfully reproduced at least twice. For experiments in which statistics are given, details on the statistical analyses or tests are given in the methods pertaining to each experiment and/or the appropriate legend. Below is a description of experimental replications for each main and Extended Data figure.

For experiments with statistics given, the following list gives the *P* values for statistical tests given in the indicated figures and the number of biological replicates (*n*): in Fig. 1a, *P* values are presented as the −log of the *P* values. Values for each protein are given in Supplementary Table 1. In Fig. 4e comparing SEC61β intensities in ribosome pellets from wild-type and *UFC1*^{KO} cells treated with puromycin to induce ribosome release from SEC61, *P* values were 1×10^{-4}, 4×10^{-7}, 2×10^{-5} and 1×10^{-9} for 1, 5, 15 and 30 min time points, respectively ($n = 4$). In Fig. 4f comparing SEC61β intensities in ribosome pellets from wild-type and *UFC1*^{KO} cells treated with harringtonine to induce ribosome release from SEC61, *P* values were 2×10^{-3}, 4×10^{-5} and 3×10^{-2} for 5, 15 and 30 min time points, respectively ($n = 3$). In Fig. 4i comparing ER–AP accumulation (signal) in *DDRGK1*^{KO} cells rescued with wild-type DDRGK1 or empty vector, the *P* value was 7×10^{-4} ($n = 5$). In Extended Data Fig. 9d comparing ribosome pellets of WT and UFIM(mt) rescued *DDRGK1*^{KO} cells, *P* values were 7×10^{-3} and 2×10^{-5} for UFL1 signals and CDK5RAP3 signals, respectively ($n = 3$). In Extended Data Fig. 9g comparing SEC61α intensities in ribosome pellets from wild-type and *UFC1*^{KO} cells treated with puromycin to induce ribosome release from SEC61, *P* values were 1×10^{-2}, 4×10^{-2}, 6×10^{-2} and 3×10^{-2} for 1, 5, 15 and 30 min time points, respectively ($n = 2$). In Extended Data Fig. 9h comparing SEC61α intensities in ribosome pellets from wild-type and *UFC1*^{KO} cells treated with harringtonine to induce ribosome release from SEC61, *P* values were 3×10^{-4}, 2×10^{-5} and 7×10^{-5} for 5, 15, and 30 min time points, respectively ($n = 3$). In Extended Data Fig. 9i comparing SEC61β intensities in ribosome pellets from WT and *UFM1*^{KO} cells treated with harringtonine to induce ribosome release from SEC61, *P* values were 5×10^{-3}, 1×10^{-2} and 2×10^{-3} for 5, 15, and 30 min time points, respectively ($n = 3$). Extended Data Fig. 9i comparing SEC61α intensities in ribosome pellets from WT and *UFM1*^{KO} cells treated with harringtonine to induce ribosome release from SEC61, *P* values were 3×10^{-2}, 1×10^{-2} and 1×10^{-3} for 5, 15, and 30 min time points, respectively ($n = 3$). The number of biological replicates for these experiments was chosen based on the effect size of the measurement and/or the expected variability or, in the case of Fig. 1a, the available TMT channels to maximize statistical robustness. All experimental data were included in the statistics; no replicates were excluded from the analyses.

The following details the robustness of experimental data for which no statistical analysis was performed. For the experiment in Fig. 1b,c, although this experiment as it is presented was performed only once under these exact conditions, other similar experiments were performed to test a number of the proteins seen in the identification list

by western blot and was replicated in a similar MS experiment (albeit with a different solubilizing detergent) that gave similar results. Furthermore, experiments in Fig. 1d,e and Extended Data Fig. 1k,i,m,n replicate the binding of the E3(UFM1) and this is underscored by the cryo-EM from cell pull-downs using Flag–UFM1 maps and models. MS of these Flag–UFM1 cryo-EM samples revealed similar results as Fig. 1c, but these data did not have a background control to exclude nonspecific proteins. Hence, the pull-down MS experiment in Fig. 1c and its findings can be considered replicated. The experiments in Fig. 1d were replicated in different parts during pilot experiments and during method optimization, and in different cell lines (HEK293 and/or U2OS with wild-type, *UFSP2*^{KO} and/or *UFM1*^{KO} cells) with no fewer than two observations of each protein probed in these similar experiments. All results were similar. The experiments in Fig. 1e and the related experiments performed in Extended Data Fig. 1m,n were performed twice, albeit with slightly different parameters (for example, for sucrose sedimentation conditions) and in highly similar experiments during the optimization of conditions. Experiments in Extended Data Fig. 1b–d were replicated multiple times in part or in whole during the development of the miniTurbo MS experiments with each observation being made at least twice. These observations are also made in the MS data in Fig. 1a and were also observed in other MS experiments not described in this article with statistical analyses and at least four replicates (that is, such is the case for Extended Data Fig. 1d,c). Each part of the experiment in Extended Data Fig. 1e was extensively replicated, with two replications of the eL36–SBP pull-down being performed and >5 replicates being performed for SBP–UFM1 pull-downs during MS sample optimization and early cryo-EM sample preparations. The qualitative observations in Extended Data Fig. 1g was replicated in K562 cells (as depicted) under similar conditions and replicated in part or in whole in HEK293 and U2OS cell lines. These observations are also present in Fig. 1d, but with better detection of modified uL22 after membrane ribosome extraction. The densitometry values of plots in Extended Data Fig. 1g,h are available as source data in Supplementary Table 3. Experiments in Extended Data Fig. 1i,k were performed with biological triplicates as shown; although the mean and s.d. are shown, a statistical test was not performed for these data. The data presented in Extended Data Fig. 1i,j are controls that only pertain to the experimental validity of the experiments in Fig. 1d and illustrate the purity of fractions used for those specific samples. The experiments performed in Figs. 2a and 4a pertain to specific samples as well; nonetheless these pull-downs and gels were replicated twice with similar conditions during different cryo-EM sample preparations. The data presented in Fig. 4c were replicated in whole twice. The experiment in Fig. 4d was replicated in part or in whole during multiple pilot experiments with each observation made at least twice. The experiments in Fig. 5a,b were replicated twice with similar experimental procedures; those in Fig. 5a,b are also highly complementary experiments. Hence, all experiments can be considered replicated at least twice.

Uncropped images, including replicate gels used in statistics, and densitometry data for all plots generated in the article are available as source data in Supplementary Figs. 1–6 and in Supplementary Tables 1–9, respectively. For more details, see the Supplementary Information. GraphPad Prism (v.10.1.0) was used for all plots made and statistics generated for immunoblot data. Densitometry was performed using Image Studio Lite (v.5.2.5).

Cryo-EM data collections from Flag–UFL1 pull-downs similar to the one shown in Fig. 4a were performed twice, but only the latter was used for this article. For the first dataset, 9,907 micrographs were collected, producing a total of 104,395 ribosomal particles. 2D and 3D classification of those particles resulted in similar particle ensembles as presented in this article, including states 1, 2 and 3 of the 60S–UFM1–E3(UFM1) complex. For the second dataset, 50,993 micrographs were selected, producing 1,247,589 ribosomal particles. This dataset largely reproduced the first dataset, but with more detail owing to the higher number of particles and therefore better resolution for each relevant class.

Cryo-EM data from the Flag–UFM1 pull-down (Fig. 2a) and the in vitro reconstituted 60S–UFM1–E3(UFM1) complex were only collected once. However, all datasets were processed using both RELION and CryoSPARC, respectively, always reproducing essentially the same results.

Reporting summary

Further information on research design is available in the Nature Portfolio Reporting Summary linked to this article.

Data availability

All relevant data are included in the manuscript and Supplementary Information. MS data files have been uploaded to the MassIVE proteomics database (https://massive.ucsd.edu/ProteoSAFe/static/massive.jsp) with the identifiers MSV000093510 and MSV000093721 for mt-UFM1 proximity and SBP-UFM1 pulldown experiments, respectively. The cryo-EM structural data generated in this study have been deposited in the Electron Microscopy Data Bank under the following accession codes: EMD-16903 for the 60S–UFM1–E3(UFM1) (obtained from the UFM1 pull-down); EMD-16908 for the 60S–E3(UFM1)–SEC61 complex in state 1 (PDB accession 8OJ8); EMD-16902 for the 60S–UFM1–E3(UFM1)–SEC61 complex in state 2 (PDB accession 8OJ0); EMD-16880 for the 60S–UFM1–E3(UFM1) complex in state 3 (states 1, 2 and 3 obtained from the UFL1 pull-down) (PDB accession 8OHD); and EMD-16905 for the in vitro reconstituted 60S–UFM1–E3(UFM1) complex (state 3 (PDB accession 8OJ5). The structures used for atomic model building of 60S–UFM1–E3(UFM1) and 60S–UFM1–E3(UFM1)–SEC61 complexes are available from Worldwide Protein Data Bank (wwPDB) with accession codes 8GLP, 8G5Y, 6Z6M and 6W6L.

36. Leto, D. E. et al. Genome-wide CRISPR analysis identifies substrate-specific conjugation modules in ER-associated degradation. *Mol. Cell* **73**, 377–389.e11 (2019).
37. An, H., Ordureau, A., Körner, M., Paulo, J. A. & Harper, J. W. Systematic quantitative analysis of ribosome inventory during nutrient stress. *Nature* **583**, 303–309 (2020).
38. McAlister, G. C. et al. Increasing the multiplexing capacity of TMTs using reporter ion isotopologues with isobaric masses. *Anal. Chem.* **84**, 7469–7478 (2012).
39. Paulo, J. A., O'Connell, J. D. & Gygi, S. P. A triple knockout (TKO) proteomics standard for diagnosing ion interference in isobaric labeling experiments. *J. Am. Soc. Mass. Spectrom.* **27**, 1620–1625 (2016).
40. Schweppe, D. K. et al. Characterization and optimization of multiplexed quantitative analyses using high-field asymmetric-waveform ion mobility mass spectrometry. *Anal. Chem.* **91**, 4010–4016 (2019).
41. Erickson, B. K. et al. Active instrument engagement combined with a real-time database search for improved performance of sample multiplexing workflows. *J. Proteome Res.* **18**, 1299–1306 (2019).
42. Schweppe, D. K. et al. Full-featured, real-time database searching platform enables fast and accurate multiplexed quantitative proteomics. *J. Proteome Res.* **19**, 2026–2034 (2020).
43. Elias, J. E. & Gygi, S. P. Target–decoy search strategy for increased confidence in large-scale protein identifications by mass spectrometry. *Nat. Methods* **4**, 207–214 (2007).
44. Elias, J. E. & Gygi, S. P. Target–decoy search strategy for mass spectrometry-based proteomics. *Methods Mol. Biol.* https://doi.org/10.1007/978-1-60761-444-9_5 (2010).
45. Huttlin, E. L. et al. A tissue-specific atlas of mouse protein phosphorylation and expression. *Cell* **143**, 1174–1189 (2010).
46. Tyanova, S. et al. The Perseus computational platform for comprehensive analysis of (prote)omics data. *Nat. Methods* **13**, 731–740 (2016).
47. Itzhak, D. N., Tyanova, S., Cox, J. & Borner, G. H. Global, quantitative and dynamic mapping of protein subcellular localization. *eLife* **5**, e16950 (2016).
48. Ishihama, Y., Rappsilber, J. & Mann, M. Modular stop and go extraction tips with stacked disks for parallel and multidimensional peptide fractionation in proteomics. *J. Proteome Res.* **5**, 988–994 (2006).
49. Ha, B. H. et al. Structural basis for Ufm1 processing by UfSP1. *J. Biol. Chem.* **283**, 14893–14900 (2008).
50. Zheng, S. Q. et al. MotionCor2: anisotropic correction of beam-induced motion for improved cryo-electron microscopy. *Nat. Methods* **14**, 331–332 (2017).
51. Rohou, A. & Grigorieff, N. CTFFIND4: fast and accurate defocus estimation from electron micrographs. *J. Struct. Biol.* **192**, 216–221 (2015).
52. Zhang, K. Gctf: real-time CTF determination and correction. *J. Struct. Biol.* **193**, 1–12 (2016).
53. Wagner, T. et al. SPHIRE-crYOLO is a fast and accurate fully automated particle picker for cryo-EM. *Commun Biol.* **2**, 218 (2019).
54. Punjani, A., Rubinstein, J. L., Fleet, D. J. & Brubaker, M. A. cryoSPARC: algorithms for rapid unsupervised cryo-EM structure determination. *Nat. Methods* **14**, 290–296 (2017).
55. Wells, J. N. et al. Structure and function of yeast Lso2 and human CCDC124 bound to hibernating ribosomes. *PLoS Biol.* **18**, e3000780 (2020).

56. Zivanov, J. et al. New tools for automated high-resolution cryo-EM structure determination in RELION-3. *eLife* **7**, e42166 (2018).
57. Kimanius, D., Dong, L., Sharov, G., Nakane, T. & Scheres, S. H. W. New tools for automated cryo-EM single-particle analysis in RELION-4.0. *Biochem. J.* **478**, 4169–4185 (2021).
58. Liang, X. et al. Structural snapshots of human pre-60S ribosomal particles before and after nuclear export. *Nat. Commun.* **11**, 3542 (2020).
59. Sanchez-Garcia, R. et al. DeepEMhancer: a deep learning solution for cryo-EM volume post-processing. *Commun. Biol.* **4**, 874 (2021).
60. Pettersen, E. F. et al. UCSF ChimeraX: structure visualization for researchers, educators, and developers. *Protein Sci.* **30**, 70–82 (2021).
61. Holm, M. et al. mRNA decoding in human is kinetically and structurally distinct from bacteria. *Nature* **617**, 200–207 (2023).
62. Emsley, P. & Cowtan, K. Coot: model-building tools for molecular graphics. *Acta Crystallogr. D Biol. Crystallogr.* **60**, 2126–2132 (2004).
63. Liebschner, D. et al. Macromolecular structure determination using X-rays, neutrons and electrons: recent developments in Phenix. *Acta Crystallogr. D Struct. Biol.* **75**, 861–877 (2019).
64. Yamashita, K., Palmer, C. M., Burnley, T. & Murshudov, G. N. Cryo-EM single-particle structure refinement and map calculation using Servalcat. *Acta Crystallogr. D Struct. Biol.* **77**, 1282–1291 (2021).
65. Croll, T. I. ISOLDE: a physically realistic environment for model building into low-resolution electron-density maps. *Acta Crystallogr. D Struct. Biol.* **74**, 519–530 (2018).
66. Williams, C. J. et al. MolProbity: more and better reference data for improved all-atom structure validation. *Protein Sci.* **27**, 293–315 (2018).
67. Goddard, T. D. et al. UCSF ChimeraX: meeting modern challenges in visualization and analysis. *Protein Sci.* **27**, 14–25 (2018).
68. Amici, D. R. et al. FIREWORKS: a bottom-up approach to integrative coessentiality network analysis. *Life Sci. Alliance* **4**, e202000882 (2021).

Acknowledgements We thank C. Ungewickell, S. Rieder and A. Gilmozzi for technical assistance; M. C. Riepe for discussion throughout this work and for critical reading of the manuscript; A. Ting for reagents and advice with the proximity labelling experiments; and Y. Liu from S^2C^2 for support and assistance. This study was supported by grants from the ERC (RELYUBL, 677623), the Lister Institute of Preventive Medicine, the BBSRC (BB/T008172/1) and the MRC (grant MC_UU_00018/3) to Y. K.; from the ERC (ADG 885711 Human-Ribogenesis and DFG (SFB/TRR-174, BE1814/15-1, BE1814/1-1) to R.B.; and from the NIH to R.R.K. (1R01GM148477 and 5R01GM074874), J.W.H. (RO1AG011085 and R01NS083524) and J.A.P. (K01DK098285). P.A.D. was supported by NIH training grant 5T32NS007280. S.C.G. was supported by NIH training grant T32GM007276 and by a Stanford Graduate Fellowship. Some of this work was performed at the S^2C^2, which is supported by the National Institutes of Health Common Fund Transformative High-Resolution Cryo-Electron Microscopy program (U24 GM129541). The content is solely the responsibility of the authors and does not necessarily represent the official views of the National Institutes of Health.

Author contributions P.A.D., I.P., R.R.K., T.B. and R.B. conceived and designed the project. P.A.D. devised and performed all cell-based and cell-free biochemical experiments, except the translocon release assays, which were designed and performed by S.C.G. and M.W., and the AP accumulation assay, performed by F.S. P.A.D. prepared the cryo-EM grids for the in vitro UFMylated 60S samples. P.A.D., A.O., J.A.P. and J.W.H. conceived and designed the proximity labelling and affinity capture experiments. A.O. and J.A.P. performed the MS experiments. J.J.P. and Y.K. provided purified UFMylation enzymes and assisted with in vitro UFMylation. I.P. generated Flag–UFM1 and Flag–UFL1 constructs and cell lines, performed immunoisolation and processed all the cryo-EM data. P.A.D. and I.P. conducted and analysed the AlphaFold modelling. I.P. generated molecular models and, together with T.B. and R.B., analysed the E3(UFM1) structures. P.A.D., I.P., R.R.K., T.B. and R.B. wrote and edited the manuscript with input from all authors.

Competing interests The authors declare no competing interests.

Additional information

Supplementary information The online version contains supplementary material available at https://doi.org/10.1038/s41586-024-07073-0.

Correspondence and requests for materials should be addressed to Roland Beckmann or Ron R. Kopito.

Peer review information *Nature* thanks Claudio Hetz, Robert Keenan and the other, anonymous, reviewer(s) for their contribution to the peer review of this work.

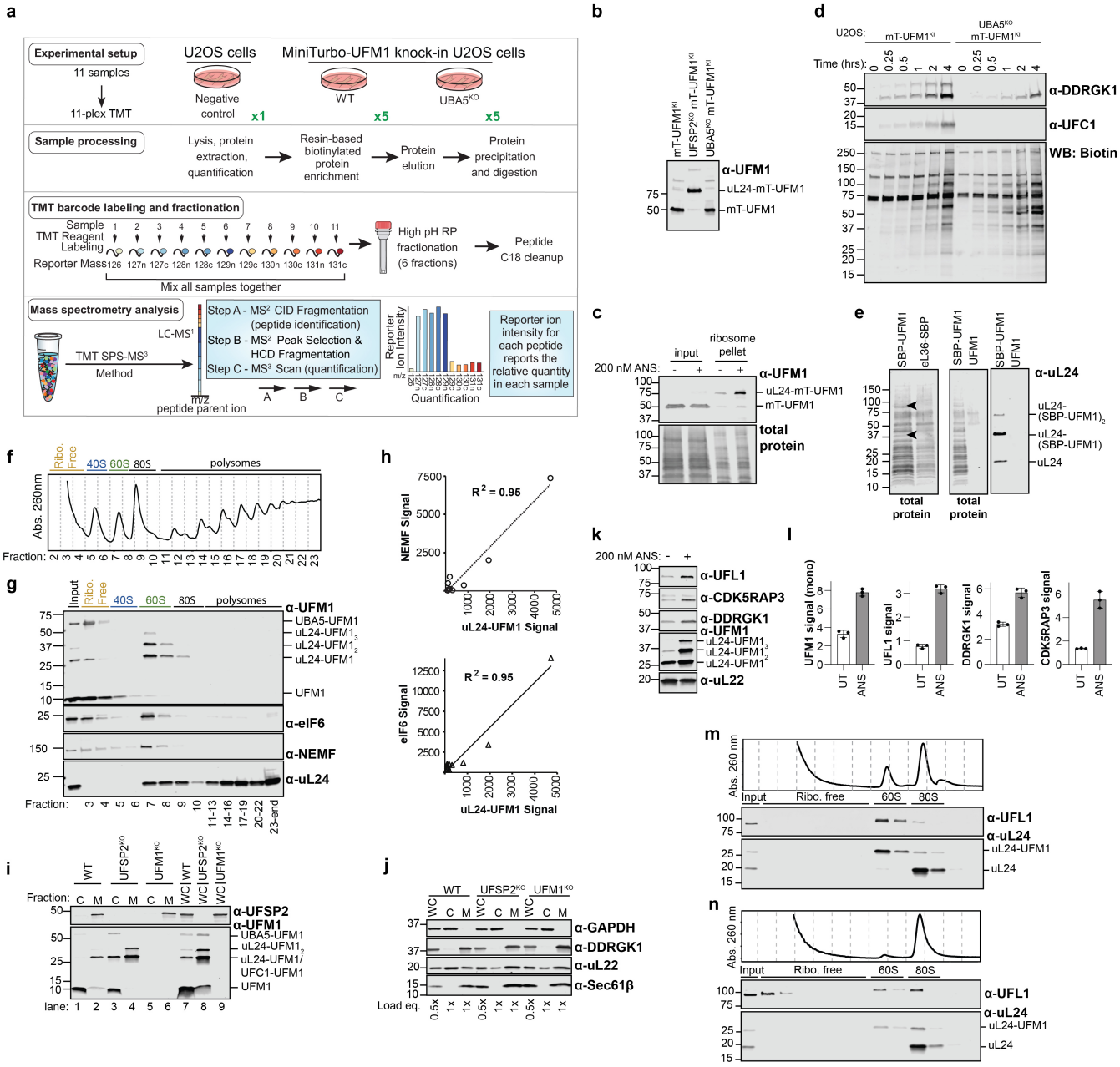

Extended Data Fig. 1 | See next page for caption.

Extended Data Fig. 1 | E3^{UFM1} selectively modifies and then binds 60S ribosomes. a, Workflow for UFM1 miniTurbo proximity profiling. **b**, Covalent modification of uL24 UFM1 by mT-UFM1 depends on expression of UBA5 and is enhanced by disruption of UFSP2. Immunoblot analysis of mT-UFM1 knock-in cell lines in the indicated genetic backgrounds used in the proximity labeling experiment in (**a**) and Fig. 1b. Note presence of non-specific band just above uL24-UFM1 band visible in *UBA5*^{KO}. **c**, mT-UFM1 is conjugated to uL24 on ribosomes (control for experiment in **a** and Fig. 1b). Lysates of U2OS mT-UFM1 knock-in cells treated with or without 200 nM anisomycin for 20 min to induce ribosome collisions were analyzed before (input) or after pelleting (ribosome pellet) through a sucrose cushion. **d**, Proximity labeling with mT-UFM1 shows conjugation-dependent biotinylation of proteins. Time course of UFC1 and DDRGK1 biotinylation in U2OS mT-UFM1 knock-in cells in wildtype or *UBA5*^{KO} background (as indicated) showing the conjugation-dependent specificity of biotin labeling. Cells were incubated with biotin for the indicated times prior to lysis, followed by streptavidin pulldowns (for biotinylated proteins), and elution from streptavidin beads by boiling in Laemmli buffer for immunoblot analysis. Based on the continued high selectivity for UFC1 biotinylation over the time course, mass spectrometry analysis was performed with a 4 h incubation with biotin (see Methods). **e**, Representative elutions from pull-downs as in Fig. 1b, c staining nitrocellulose with total protein stain (LI-COR Revert) or immunoblotted for uL24 to show the capture of ribosomes and enrichment of UFMylated uL24 (~80 % UFMylated). Transiently expressed eL36-SBP used to isolate ribosomes results in characteristic ribosome band patterning seen in SBP-UFM1 pulldowns, but lack bands (black arrowheads) discernable in the SBP-UFM1 pulldown that likely correspond to UFL1 and DDRGK1 (by molecular weight). Untagged UFM1 is used as a negative control. **f**, Sucrose density sedimentation profile for experiment in (**g**). **g**, UFM1 modifies exclusively 60S in vivo. Lysates from wildtype K562 cells were fractionated on sucrose density gradients and analyzed by immunoblot with the indicated antibodies. Sedimentation behavior of UFMylated uL24 parallels that of the obligatory 60S markers NEMF and eIF6. **h**, Quantification of indicated bands for fractions in (**g**) showing correlations between UFMylated uL24 and NEMF (upper) and eIF6 (lower). **i**, Validation of cell lines (lanes 7–9) and UFM1 and UFSP2 distribution in fractions (lanes 1–6) used for the sucrose density sedimentation in Fig. 1d. Clonal K562 cell knockouts of UFSP2 and UFM1 show no detectable expression of UFSP2 and UFM1, respectively. Cell lysates were separated via sequential detergent fractionation into, cytosolic ("C"), and membrane ("M") fractions and analyzed by immunoblot with indicated antibodies. Non-fractionated whole cell lysate, "WC". This fractionation distinguishes the cytosolic UFC1-UFM1 adduct (an isopeptide linked conjugate) from the co-migrating uL24-UFM1 conjugate as reported previously[2,6,12]. **j**, Additional fractionation controls as in (**i**) for samples used in Fig. 1d showing partitioning of ER membrane and cytosolic markers. Membrane fractions are highly enriched for membrane markers (DDRGK1 and SEC61β) and lack cytosolic contaminants (e.g., GAPDH). **k**, Ribosome collisions increase E3^{UFM1}–60S association. K562 cells were treated with or without 200 nM anisomycin (ANS) for 1 h to induce ribosome collisions. Lysates were sedimented through 1 M sucrose to isolate ribosomes and analyzed by immunoblotting with the indicated antibodies. **l**, Quantification of mono-UFMylated uL24, UFL1, DDRGK1, and CDK5RAP3 from biological triplicates in experiment as in (**k**). Data show mean ± SD for n = 3 biological replicates. **m**, 60S ribosomes are the preferred target of UFMylation in vitro. Sucrose density sedimentation analysis of in vitro UFMylation reaction containing a 1:2 60S:80S molar ratio showing selectivity for 60S ribosome modification. **n**, 80S ribosomes are poor substrates of UFMylation in vitro. Sucrose density sedimentation as in (**m**) with the same concentration of 80S ribosomes as substrate showing strongly reduced UFMylation and E3^{UFM1} binding. Source data is available in Supplementary Fig. 5 (for **b**-**e** and **g**-**n**), Supplementary Table 3 (for **h**), and Supplementary Table 4 (for **l**). Data in b-e, g, k, m, and n were replicated at least twice with similar results; for detailed descriptions see "Statistics and reproducibility" section of the Methods. The mobility of molecular weight markers (in kDa) is indicated on the left hand side of the blots in panels **b**-**e**, **g**, **i**-**k**, **m**, **n**.

a

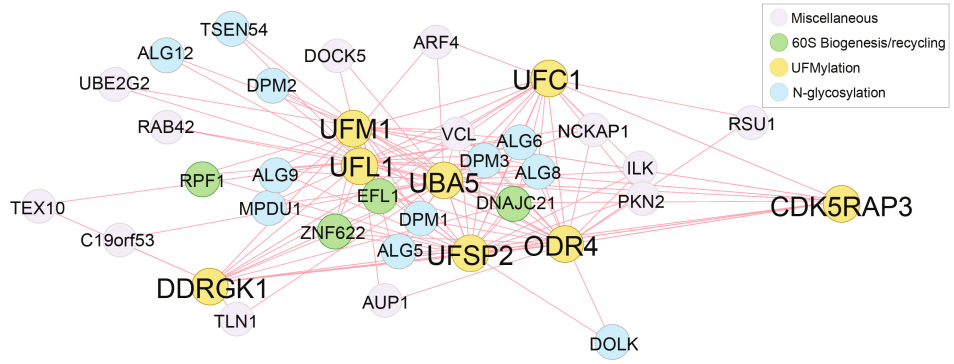

b

Rank	Gene	Entrez Id	Correlation
1	UBA5	79876	0.83
2	UFL1	23376	0.78
3	UFSP2	55325	0.67
4	ODR4	54953	0.63
5	UFC1	51506	0.60
6	DDRGK1	65992	0.50
7	CDK5RAP3	80279	0.38
8	DNAJC21	134218	0.37
9	ZNF626	199777	0.34
10	SBDS	51119	0.33
11	EFL1	79631	0.31

c

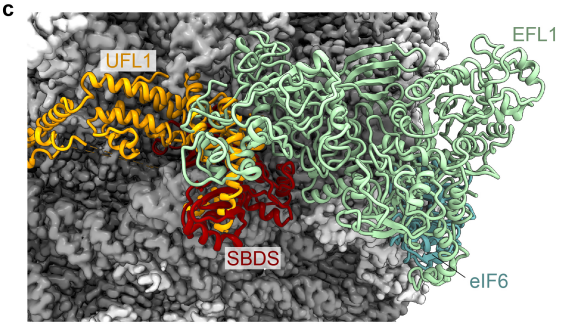

Extended Data Fig. 2 | Coessential relationship between UFMylation and 60S recycling pathway genes. a, The UFMylation pathway exhibits strong co-essentiality with genes involved in 60S ribosome biogenesis (green circles) and N-glycosylation genes (blue circles). All UFMylation pathway genes (yellow circles) were used as input for the FIREWORKS (https://mendillolab.shinyapps.io/fireworks/)[68]. **b**, Table of DEPMAP co-dependencies for UFM1 network showing strong Pearson correlations with UFM1 pathway (yellow) and with 60S biogenesis factors EFL1, SBDS, and DNAJC21 (green). **c**, The UFL1-CTD binding site is incompatible with EFL1 and SBDS binding. Overlay of 60S-UFM1-E3^{UFM1} complex in State 3 with 60S-bound SBDS and EFL1 before displacement of eIF6 (PDB 5ANB)[35]. Note that the CTD of UFL1 (orange) would sterically clash with SBDS and EFL1, suggesting that eIF6 eviction may not occur until E3^{UFM1} has dissociated.

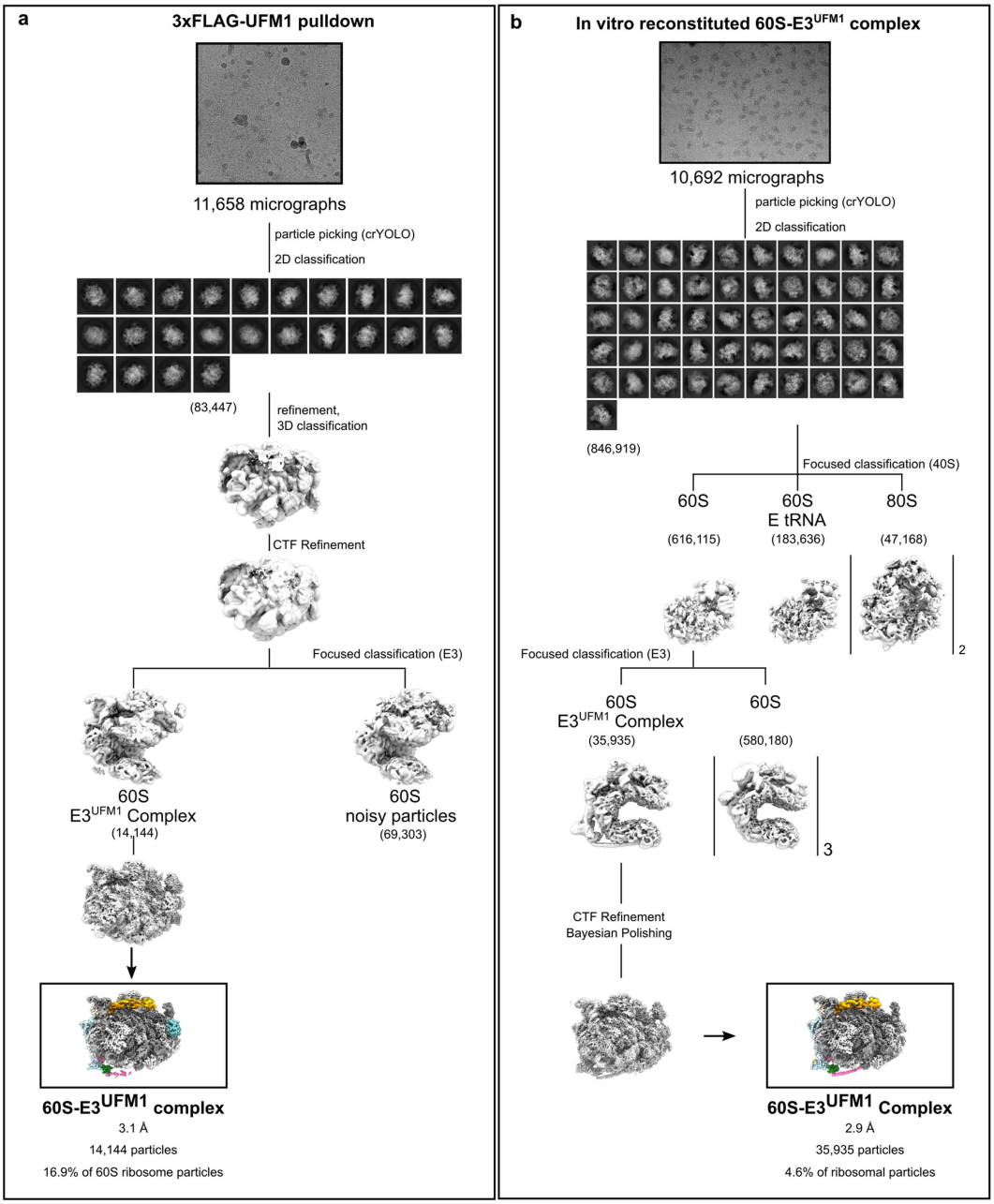

Extended Data Fig. 3 | Cryo-EM data analysis and classification of native and reconstituted 60S-UFM1-E3^{UFM1} complexes. a, Data processing scheme for the native 60S-UFM1-E3^{UFM1} complex derived from a FLAG-UFM1 pulldown. 616,046 particles were picked from 11,658 micrographs using crYOLO. Following 2D classification in cryoSPARC, 83,447 particles corresponding to 60S ribosomal subunits were selected. A consensus refinement was performed followed by CTF refinement in RELION. The 60S particles were then subjected to several rounds of 3D classification using a soft mask focusing on regions where non-ribosomal extra density was observed. This revealed one stable class consisting of 14,144 particles (16,9% of all 60S particles) that was refined to an average resolution of 3.1 Å. **b**, Data processing scheme for the in vitro reconstituted 60S-UFM1-E3^{UFM1} complex. 1,136,353 particles were picked from 10,692 micrographs using RELION's AutoPick LoG algorithm. 2D classification revealed 846,919 ribosomal particles. 3D classification with a focused mask around the 40S revealed a number of classes, a majority of which were 60S particles with and without a bound E-site tRNA. In addition, two classes representing empty 80S ribosomes were found. Using a soft mask focusing on regions where non-ribosomal extra density was observed, one stable class consisting of 35,935 particles (4.6% of all particles) was isolated representing the stable 60S-UFM1-E3^{UFM1} complex. This class was refined to an average resolution of 2.9 Å.

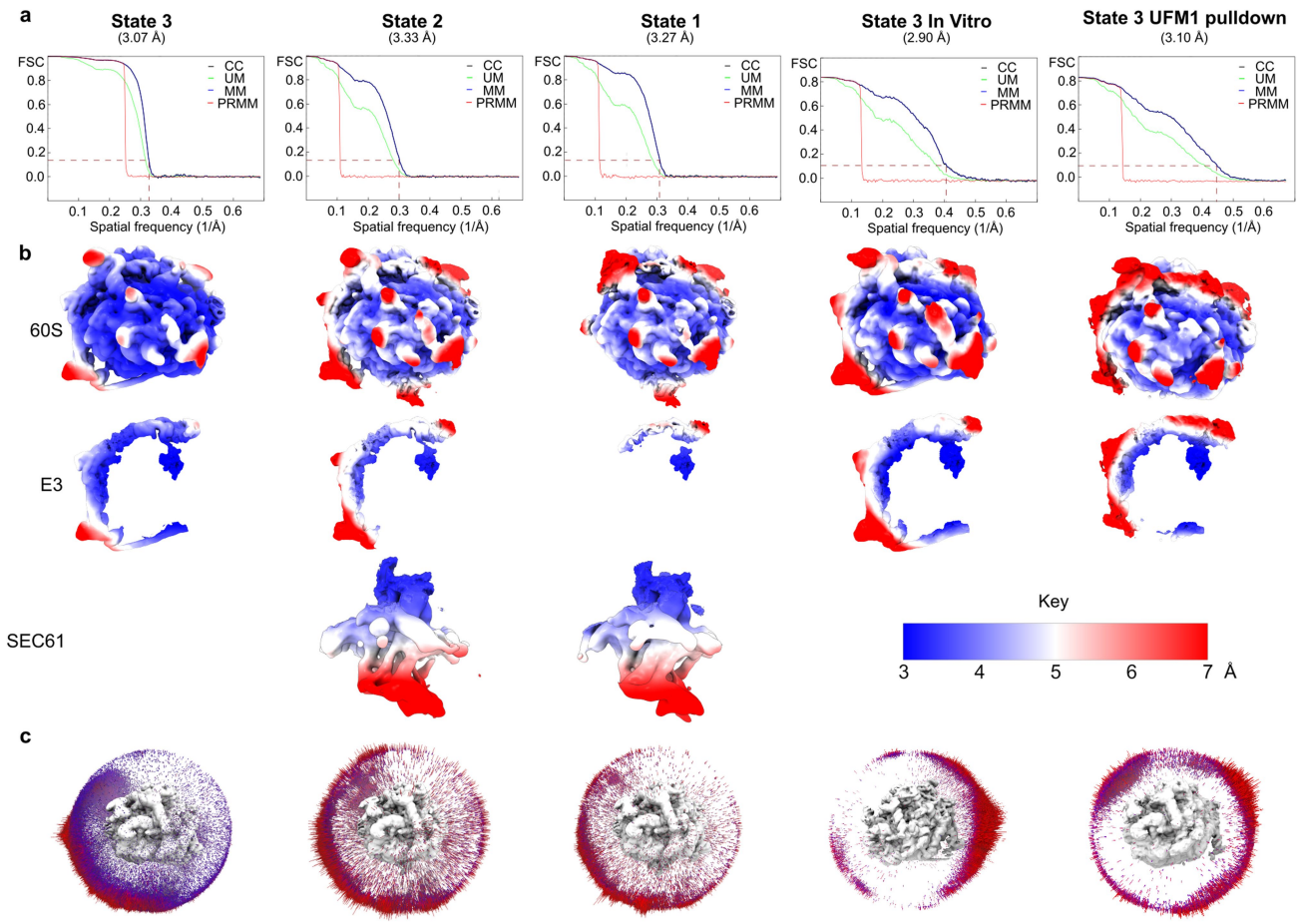

Extended Data Fig. 4 | Overall and local resolution and angular distribution of 60S-UFM1-E3^{UFM1} complexes. (Local) resolution and angular distribution was assessed in RELION for the FLAG-UFM1 pulldown and the in vitro reconstituted sample (both resulting in State 3; see Extended Data Fig. 3) and the FLAG-UFL1 pulldown sample (yielding states 1, 2 and 3; see Extended Data Fig. 7). **a**, Gold-standard Fourier Shell Correlation (FSC) curves (obtained from RELION) for the reconstructions of the three states obtained from the UFL1 pulldown sample (states 1–3), the in vitro reconstituted sample (state 3) and the UFM1-pulldown sample (also state 3). CC = correlation corrected; UM = unmasked maps; MM = masked maps; PRMM = phase randomized masked maps. **b**, Cryo-EM maps, displayed after Gaussian low-pass filtering at a standard deviation of 2 in ChimeraX and colored according to local resolution. Shown are the entire 60S-UFM1-E3^{UFM1} reconstructions (60S) as well as isolated densities for the E3^{UFM1} (E3) and the SEC61 complex (SEC61; visualized in states 1 and 2 as obtained from the FLAG-UFL1 pulldown sample). **c**, Original (unfiltered) cryo-EM maps and angular distribution plots for final 60S-UFM1-E3^{UFM1} complex reconstructions obtained from RELION. The height and color (from blue to red) of the cylinder bars is proportional to the number of particles in those views.

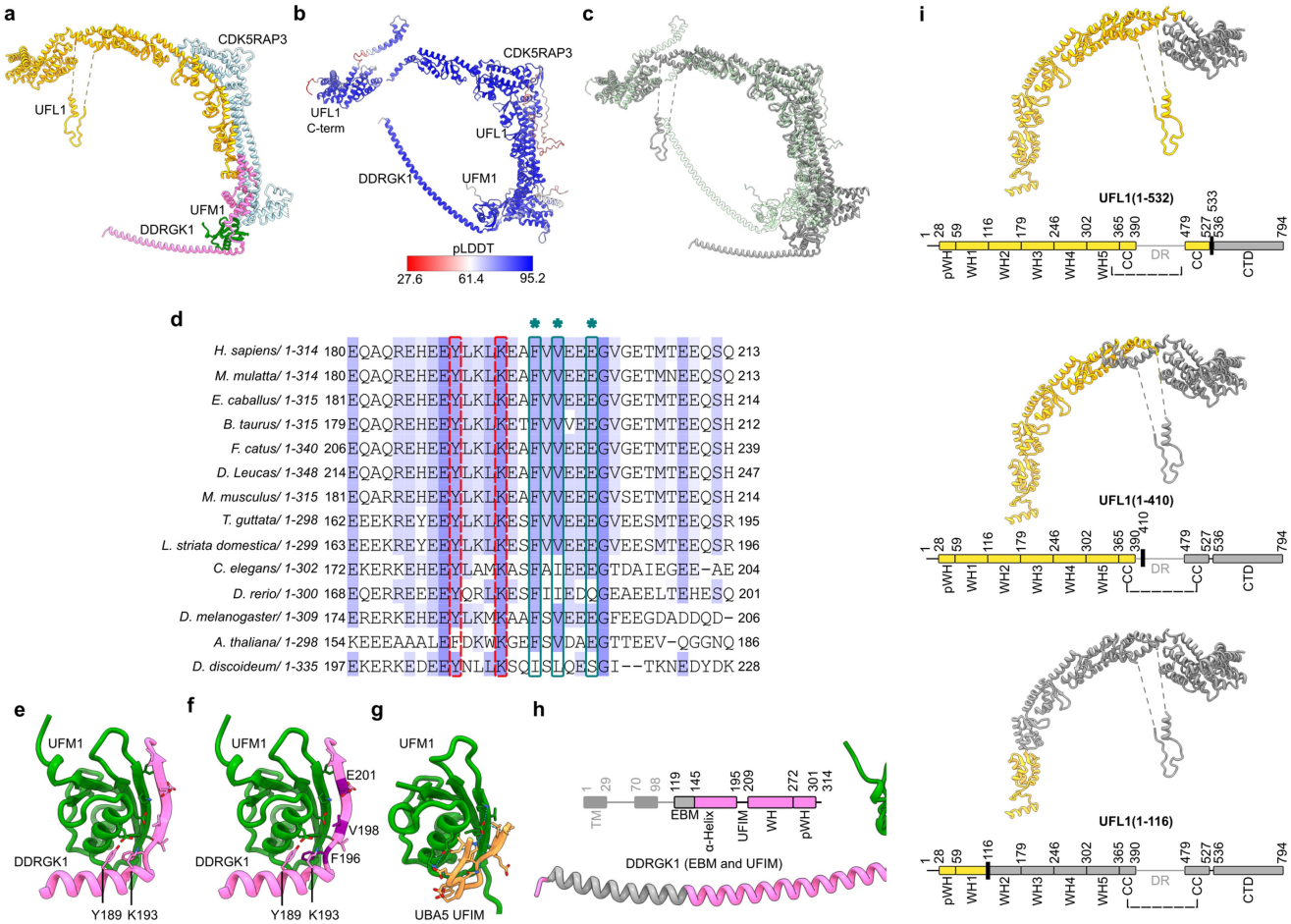

Extended Data Fig. 5 | Models and mutational analyses of the 60S-UFM1-E3^{UFM1} complex. a, Final model of the UFM1-E3^{UFM1} complex derived from fitting the AlphaFold model (shown in (**b**) into the cryo-EM map of the reconstituted 60S-UFM1-E3^{UFM1} complex. This conformation represents State 3. **b**, AlphaFold model of the UFM1-E3^{UFM1} complex. In this model, the C-terminal region (480–794) of UFL1 was derived from AlphaFold 2 prediction[18] and an N-terminal fragment (1–389) was used for AlphaFold-Multimer modeling[19]. The models are colored according to a per-model confidence score (pLDDT; from 0 to 100). Blue regions display a very high confidence (pLDDT > 90), red region low confidence (pLDDT <50). **c**, Overlay of the initial AlphaFold model (green) with the final cryo-EM model (grey). **d**, Multiple sequence alignment of the DDRGK1 UFIM and flanking regions. Intensity of color (blue/violet) represents the % sequence identity. Mutated residues in UFIM^{mt} are indicated by asterisks. Conserved residues that contact UFM1 at the C-terminal end of the DDRGK1 exit-binding helix (EBH; shown in (**e**) and (**f**) are highlighted in red. **e**, Close-up of the DDRGK1 UFIM and EBH interactions with UFM1 derived from AlphaFold-Multimer prediction and consistent with cryo-EM density map. Side chain interactions predicted by AlphaFold-Multimer at this interface are noted. **f**, Same as (**e**), but with the amino acids that were mutated in Figs. 4d, h and i within the UFIM highlighted in purple. **g**, Crystal structure of the UFIM of UBA5 in complex with UFM1 (PDB 5IA8)[23]. Like the DDRGK1 UFIM, the UBA5 UFIM also establishes a β-augmentation with β2 of UFM1, however, neither the sequence nor the overall conformation of these UFIMs are conserved. **h**, Molecular model and schematic representation of the DDRGK1 ΔEBM mutant used in Figs. 4d, h and i. The truncated regions are depicted in gray. **i**, Molecular model and schematic representation of UFL1 C-terminal deletion mutants used in Fig. 4c. Truncated regions are depicted in gray. UFL1(1–532) = ΔCTD.

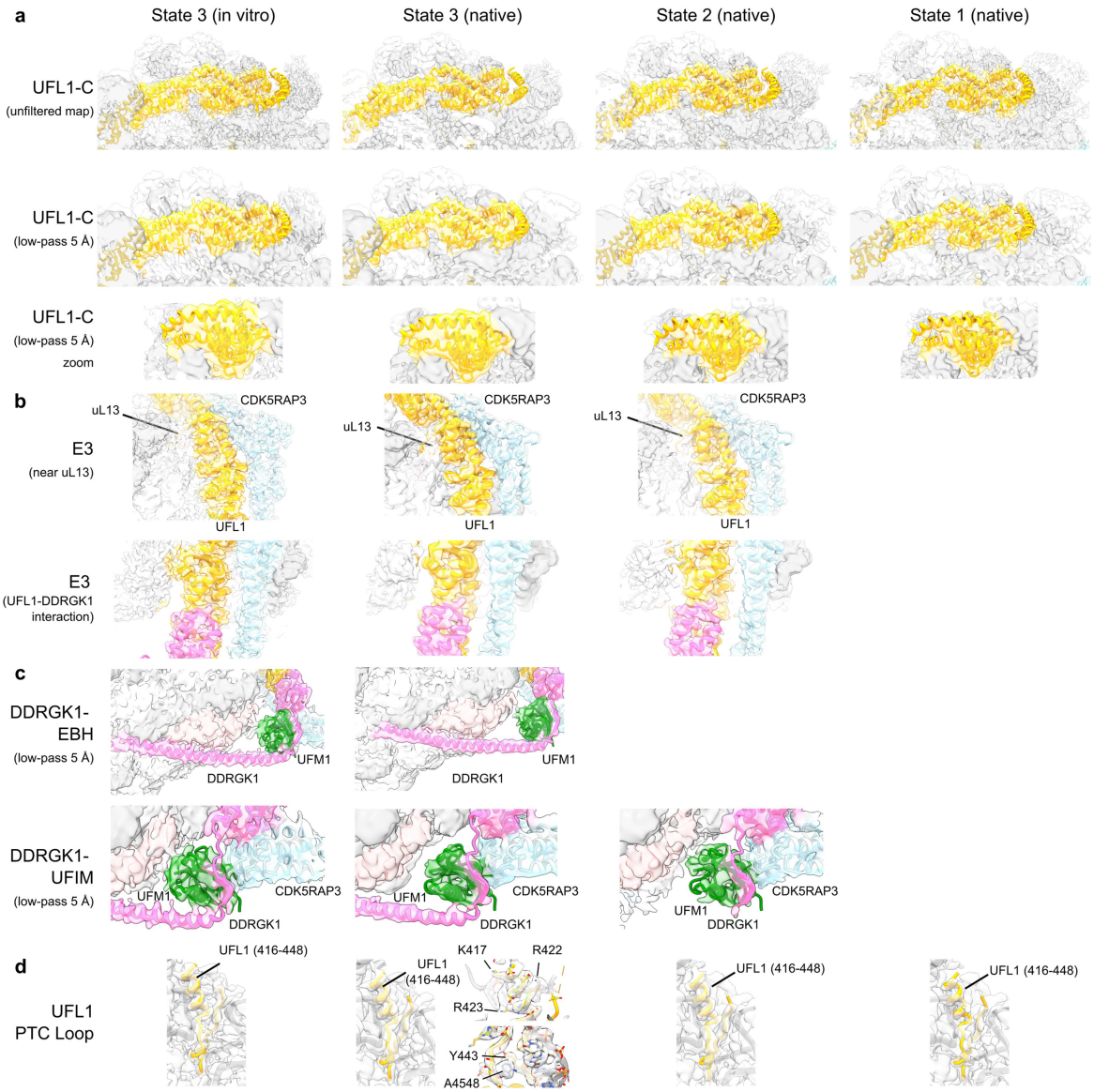

Extended Data Fig. 6 | Map quality, model fitting and molecular interactions of 60S-UFM1-E3^{UFM1} complexes. Shown are fits of the E3^{UFM1} complex model (in ribbons) into cryo-EM maps (transparent surface) of the FLAG-UFL1 native pulldown sample (States 1–3; native) and the in vitro reconstituted sample (state 3; in vitro). **a**, Views highlighting the interactions of the UFL1 C-terminal regions (UFL1-C) with the 60S. The maps are shown unmodified after refinement (upper row) or low-pass filtered at 5 Å (center and bottom rows) to visualize more flexible parts. Bottom row, close-up of the UFL1-C in center row; alternate angle. UFL1, yellow; 60S, grey. **b**, Views highlighting the interaction network of CDK5RAP3 and DDRGK1 with the UFL1 scaffold. Upper row; central region of the E3 complex (E3) with multiple interactions between UFL1 (yellow) and CDK3RAP5 (blue) near uL13. Lower row; UFL1/DDRGK1(magenta) interface (pHW complementation). In state 1, these parts of the complex are not resolved. **c**, Views focusing on the DDRGK1 EBH (upper row) and close-up view on the DDRGK1 region near uL24-conjugated UFM1 (lower row; uL24, light pink; UFM1, green). Here, β-augmentation is predicted by AlphaFold formed by UFM1 and the UFIM-containing linker region between the DDRGK1 EBH and the DDRGK1 WH. The cryo-EM maps were low-pass filtered at 5 Å and show experimental evidence for predicted β-augmentation. Note that in state 1, these parts of the complex are not visualized and in states 1 and 2, the DDRGK1 EBH is not positioned. **d**, Views focusing on the structured PTC loop region (D416-V448) of the UFL1 disordered domain (N391-F479) identified near the peptidyl transferase center (PTC) of the 60S. In the best resolved density map for this region (State 3 from FLAG-UFL1 pulldown), a clear helical density is present that fits the α-helical part of the N-terminus of this region (State 3, upper right). We clearly observe densities for three basic residues (K417, R422 and R423); UFL1 Y443 engages in stacking interactions with 25S rRNA base A4548 (lower right; see also Fig. 3f).

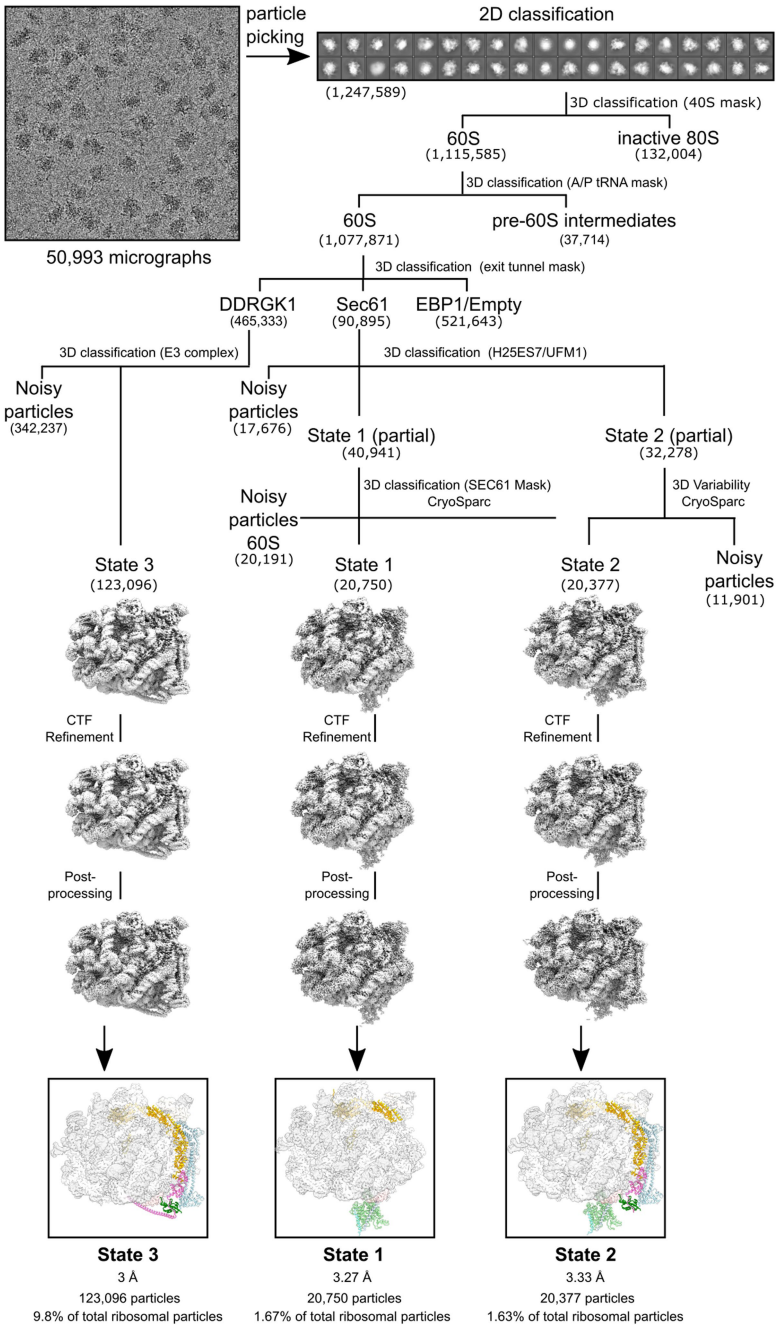

Extended Data Fig. 7 | Cryo-EM data analysis and classification of native 60S-E3^{UFM1} complexes derived from the FLAG-UFL1 pulldown. From 50,993 micrographs, 3,017,721 particles were picked using RELION AutoPick and used for 2D classification, which yielded a total of 1,247,589 ribosomal particles. 3D classification with a mask focusing around the 40S revealed 132,004 inactive 80S ribosomes harboring eEF2 and EBP1 (ref. 55), with the remainder of particles being 60S subunits. The 60S particles were further classified with a mask focusing around the A- and P- sites of the 60S, revealing 37,714 particles corresponding to a biogenesis intermediate featuring LSG1, NMD3, and ZNF622 (PDB 6LSR[58]). No density corresponding to the UFMylation machinery was found in this class. The remaining particles were sorted with a mask focusing around the tunnel exit of the 60S, revealing three major subsets. One subset featured the DDRGK1 EBH and was further classified, revealing the entire E3 complex at a final resolution of 3 Å. This state was dubbed state 3. The second subset featured SEC61 bound to the 60S, and downstream classification revealed two distinct classes, one with the entire E3 bound, but with a delocalized DDRGK1 helix, and a second featuring only the C-terminal region. These states were refined to final resolutions of 3.33 and 3.27 Å, respectively, and were dubbed States 2 and 1. The last subset featured either EBP1 or no density around the tunnel exit, and further classification showed that these were empty 60S subunits.

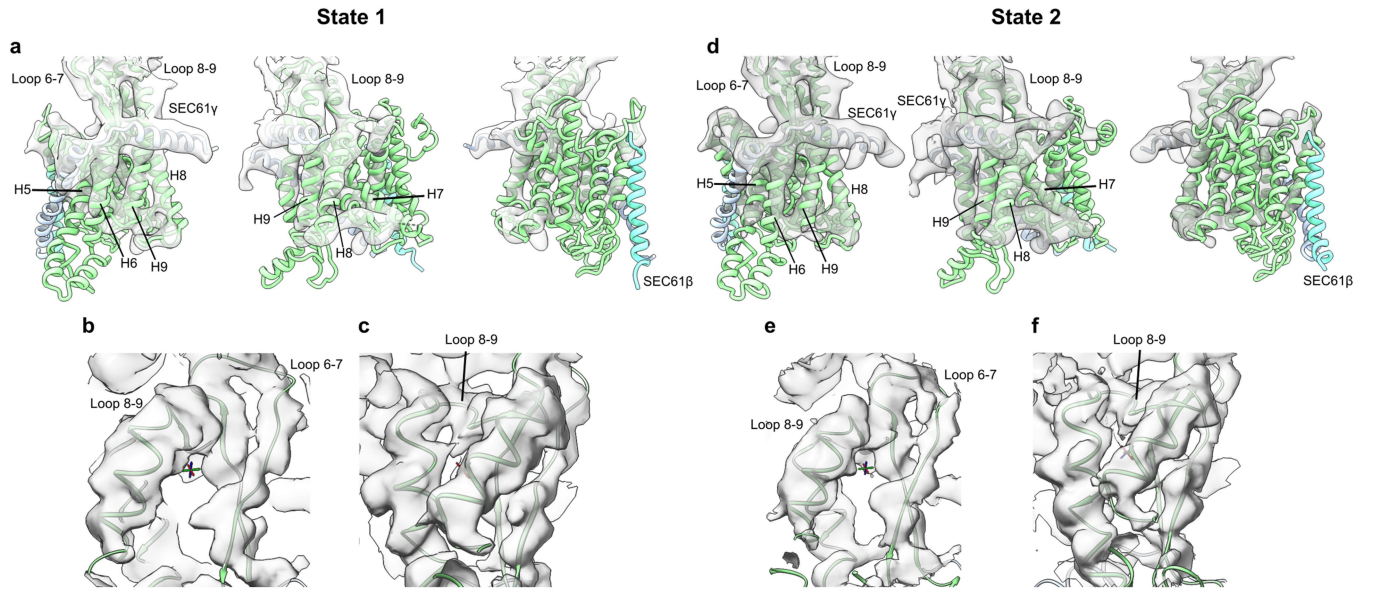

Extended Data Fig. 8 | SEC61 model fitting in States 1 and 2. a, Three views of the SEC61 complex density from State1, low-pass filtered at 5 Å (transparent grey) with fitted model of SEC61 in closed state (PDB 6W6L)[26]. Left and center views at the C-terminal half of SEC61α including the ribosome anchor (loops 6-7 and 8-9) and the amphipathic helix of SEC61γ. This region is usually well-resolved in ribosome-SEC61 cryo-EM reconstructions and we observe helical density for transmembrane helices 5–9 of SEC61α and the N-terminal amphipathic helix of SEC61γ. Right; View at the N-terminal half of SEC61α and SEC61β. Here, the density is expectedly rather weak and only visible at very low contour levels. The N-terminal half is more flexible, especially in case the complex is not engaged with a nascent peptide substrate. **b**, **c**, Close-up views at the ribosome binding site of SEC61α, consisting of loops L6-7 and L8-9 (unfiltered density map). Here, density for these loops could be unambiguously fitted. **d**-**f**, same as (**a**-**c**), but for state 2.

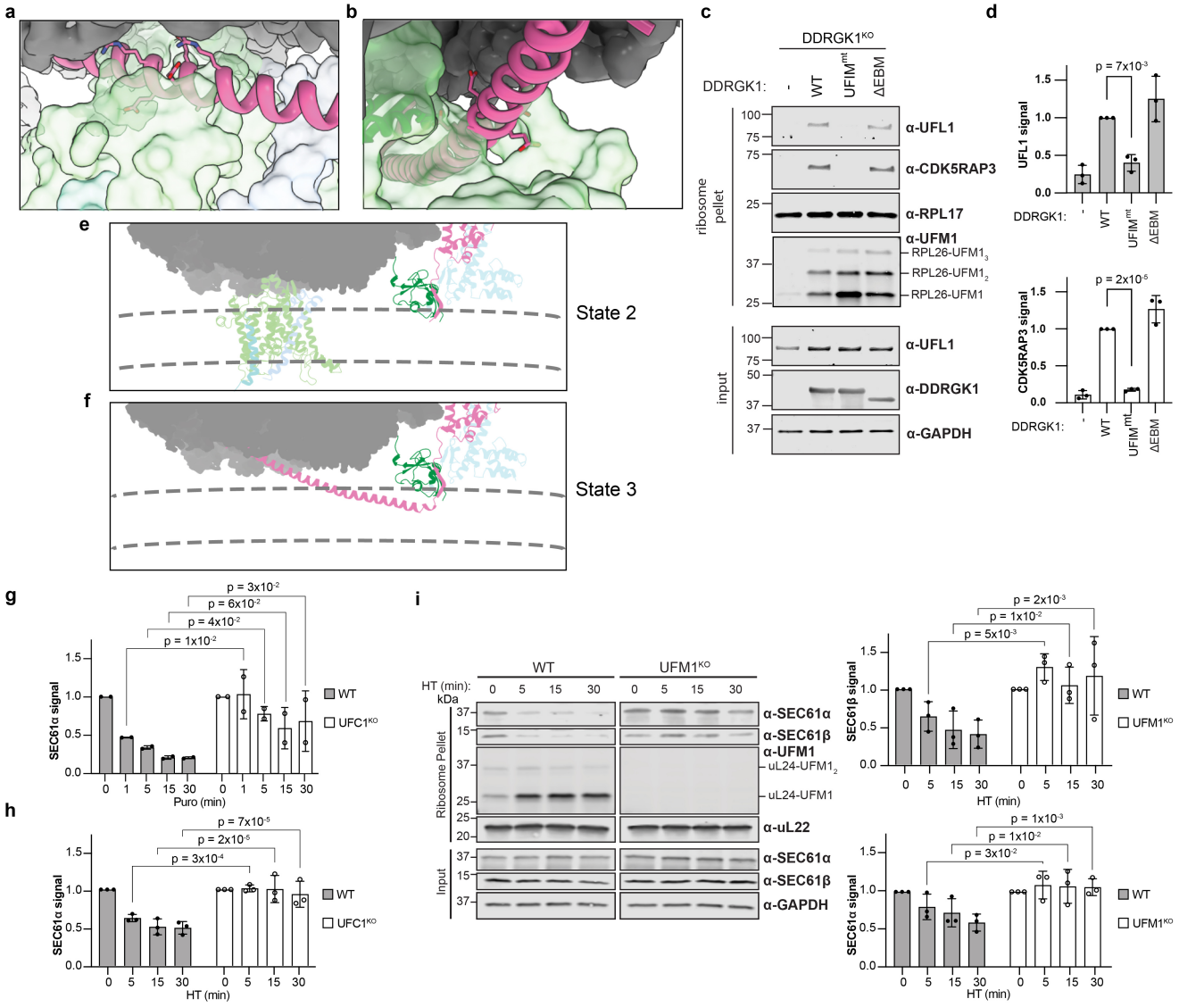

Extended Data Fig. 9 | UFMylation of 60S promotes SEC61 displacement. **a**, **b**, Two views showing steric clashes between the N-terminal tip of the DDRGK1 EBH with SEC61 at the 60S tunnel exit site. Shown is an overlay of the DDRGK1 helix from State 3 (pink) with SEC61 from State 2 (model shown as transparent surface; SEC61α, light green; SEC61γ light blue). **c**, Mutation of the DDRGK1 UFIM reduces ribosome $E3^{UFM1}$-60S association. Representative immunoblot analysis of ribosome pellets or inputs from *DDRGK1*^{KO} HEK293 cells transiently replaced with indicated DDRGK1 variants. UFMylation was stimulated with anisomycin to enhance the detection of the low abundance E3-ribosome association. **d**, Quantification of UFL1 and CDK5RAP3 band intensities of ribosome pellets as in (**c**) from biological triplicates. Data show mean ± SD relative to *DDRGK1*^{KO} HEK293 rescued with WT DDRGK1. P values in plots for the indicated comparisons were derived from one-way ANOVA and Dunnett's multiple comparison tests for n = 3 biological replicates. **e**, **f**, 60S-UFM1-$E3^{UFM1}$ complexes sterically clash with the outer leaflet of the ER membrane. Cryo-EM maps for State 2 (**e**) and State 3 (**f**) 60S-UFM1-$E3^{UFM1}$ complexes were fitted into cryo-ET maps of mammalian ER-membrane-bound 80S ribosomes (EMD-0084)[24] to obtain an outline of the lipid bilayer (gray dashed lines). The observed position of UFM1 and the bound $E3^{UFM1}$ would partially clash with the ER membrane in State 2 requiring a slight tilt of the ribosome at the SEC61-ribosome junction to accommodate stable E3 association. In State 3, the DDRGK1 EBH would reach deep into the lipid bilayer and could only be accommodated with a substantial tilt or full dissociation of the ribosome from the SEC61 complex. **g**, Quantification of SEC61α band intensities in ribosome pellets, as in Fig. 4e. Data show mean ± SD relative to untreated and p values from indicated comparisons derived from a two-way ANOVA followed by uncorrected Fisher's LSD for $n = 2$ biological replicates. **h**, Quantification of SEC61α band intensities in ribosome pellets, as in 4f. Data show mean ± SD relative to untreated and p values from indicated comparisons derived from a two-way ANOVA followed by uncorrected Fisher's LSD for $n = 3$ biological replicates. **i**, UFMylation is required for timely dissociation of 60S from translocon following translation termination. Immunoblot analysis of ribosome pellets or inputs from WT or *UFM1*^{KO} HEK293 cells treated with 3.75 µM harringtonine for the indicated times. Quantification of SEC61α or SEC61β band intensities in ribosome pellets, as in 4e,f. Data show mean ± SD relative to untreated and p values from indicated comparisons derived from a two-way ANOVA followed by uncorrected Fisher's LSD for $n = 3$ biological replicates. Source data is available in Supplementary Fig. 6 (for **c**-**d** and **g**-**i**) and Supplementary Tables 5, 6, 7 and 8 (for **d**, **g**, **h** and **i**, respectively). All experiments were replicated at least twice; for p values and detailed descriptions of data replications see "Statistics and reproducibility" section of the Methods. The mobility of molecular weight markers (in kDa) is indicated on the left hand side of the blots in panels **c** and **i**.

Extended Data Table 1 | Cryo-EM data collection, refinement and model validation

	60S-UFM1-E3^{UFM1} (State 3) (UFM1 pulldown) (EMDB-16903)	60S-E3^{UFM1}-SEC61 (State 1) (UFL1 pulldown) (EMDB-16908) (PDB 8OJ8)	60S-UFM1-E3^{UFM1}-SEC61 (State 2) (UFL1 pulldown) (EMDB-16902) (PDB 8OJ0)	60S-UFM1-E3^{UFM1} (State 3) (UFL1 pulldown) (EMDB-16880) (PDB 8OHD)	60S-UFM1- E3^{UFM1} (State 3) (*in vitro* reconstituted) (EMDB-16905) (PDB 80J5)
Data collection and processing					
Magnification	130000	165000	165000	165000	105000
Voltage (kV)	300	300	300	300	300
Electron exposure (e–/Å^2)	46.4	60	60	60	50
Defocus range (μm)	0.5-3.5	0.5-3	0.5-3	0.5-3	0.8-2
Pixel size (Å)	1.045	0.727	0.727	0.727	0.86
Symmetry imposed	C1	C1	C1	C1	C1
Initial particle images (no.)	616046	3017721	3017721	3017721	113635
Final particle images (no.)	14144	20750	20377	123096	35935
Map resolution (Å)	3.13	3.27	3.33	3	2.87
FSC threshold	0.143	0.143	0.143	0.143	0.143
Refinement					
Initial model used (PDB code)		6z6m, AlphaFold	6z6m, AlphaFold	6z6m, AlphaFold	6z6m, AlphaFold
Model resolution (Å)		3.3	3.3	3.1	2.7
FSC threshold		0.5	0.5	0.5	0.5
Model composition					
Non-hydrogen atoms		144644	150117	146864	145060
Protein residues		7861	8662	8224	8000
Nucleotides		3783	3742	3742	3742
Ligands		225	225	225	225
B factors (Min/max/mean) (Å^2)					
Protein		0.00/770.21/84.61	19.12/356.77/92.37	25.99/470.37/101.5	0.00/295.59/61.87
Nucleotide		6.86/1000.80/95.91	22.22/449.21/92.65	19.03/316.79/85.59	0.00/163.01/55.64
Ligand		6.86/207.84/51.46	9.41/205.31/58.79	17.4/178.08/57.47	6.18/126.85/37.66
R.m.s. deviations					
Bond lengths (Å)		0.003	0.003	0.002	0.002
Bond angles (°)		0.621	0.628	0.578	0.583
Validation					
MolProbity score		1.27	1.20	1.04	1.00
Clashscore		4.02	3.64	2.55	2.24
Poor rotamers (%)		0.09	0.08	0.46	0.38
Ramachandran plot					
Favored (%)		97.63	97.80	98.32	98.58
Allowed (%)		2.35	2.18	1.65	1.41
Disallowed (%)		0.03	0.02	0.02	0.01

Table showing data collection, processing and refinement statistics for the five cryo-EM reconstructions and resulting molecular models presented in this work.

nature portfolio

Corresponding author(s): Prof. Ron R. Kopito
Prof. Roland Beckmann

Last updated by author(s): Dec 29, 2023

Reporting Summary

Nature Portfolio wishes to improve the reproducibility of the work that we publish. This form provides structure for consistency and transparency in reporting. For further information on Nature Portfolio policies, see our Editorial Policies and the Editorial Policy Checklist.

Statistics

For all statistical analyses, confirm that the following items are present in the figure legend, table legend, main text, or Methods section.

n/a	Confirmed	
☐	☒	The exact sample size (*n*) for each experimental group/condition, given as a discrete number and unit of measurement
☐	☒	A statement on whether measurements were taken from distinct samples or whether the same sample was measured repeatedly
☐	☒	The statistical test(s) used AND whether they are one- or two-sided *Only common tests should be described solely by name; describe more complex techniques in the Methods section.*
☒	☐	A description of all covariates tested
☐	☒	A description of any assumptions or corrections, such as tests of normality and adjustment for multiple comparisons
☐	☒	A full description of the statistical parameters including central tendency (e.g. means) or other basic estimates (e.g. regression coefficient) AND variation (e.g. standard deviation) or associated estimates of uncertainty (e.g. confidence intervals)
☐	☒	For null hypothesis testing, the test statistic (e.g. *F*, *t*, *r*) with confidence intervals, effect sizes, degrees of freedom and *P* value noted *Give P values as exact values whenever suitable.*
☒	☐	For Bayesian analysis, information on the choice of priors and Markov chain Monte Carlo settings
☒	☐	For hierarchical and complex designs, identification of the appropriate level for tests and full reporting of outcomes
☒	☐	Estimates of effect sizes (e.g. Cohen's *d*, Pearson's *r*), indicating how they were calculated

Our web collection on statistics for biologists contains articles on many of the points above.

Software and code

Policy information about availability of computer code

Data collection	EPU 2.12.1., EPU 3.3.1 Proteomics data were collected using an Exploris 480 mass spectrometer or Orbitrap Fusion Lumos Tribrid MS (Thermo Fisher Scientific, San Jose, CA)

Data analysis	Cryo-EM data were processed using Relion 3.1.1 and 4.0.1, MotionCor2 1.4.0, CTFFIND4 4.1.13, GCTF (https://www2.mrc-lmb.cam.ac.uk/download/gctf/), crYOLO 1.7.6 and cryoSPARC 3.2 and 4.2. For 2D classification the VDAM algorithm (available in Relion version 4.0.1) was used. Molecular models were built and refined using Coot 0.9.8 and Phenix 1.21-4487, Servalcat REFMAC5 and ISOLDE (as plug-in for ChimeraX-1.6); DeepEMHancer; Structural figures were created using ChimeraX 1.6 Proteomics data were processed using: - Comet (v2019.01 rev. 5); Eng, J.K. et al. (2013), Proteomics 13, 22-24. - Perseus (version 1.5.3.2); Tyanova et al., Nat Methods. (2016) 13:731-40. http://www.perseus-framework.org - Microsoft Excel v16 https://www.microsoft.com Densitometry and resulting plots were processed using: - Image Studio Lite Version 5.2.5 - Microsoft Excel v16 https://www.microsoft.com - GraphPad Prism - version 10.1.2 For co-essentiality analysis the FIREWORKS interactive network tool69 (https://mendillolab.shinyapps.io/fireworks/) was used. UFM1 co-dependencies were obtained from the Broad Institute's DEPMAP portal (https://depmap.org/portal/) (23Q4 release).

For manuscripts utilizing custom algorithms or software that are central to the research but not yet described in published literature, software must be made available to editors and reviewers. We strongly encourage code deposition in a community repository (e.g. GitHub). See the Nature Portfolio guidelines for submitting code & software for further information.

Data

Policy information about availability of data

All manuscripts must include a data availability statement. This statement should provide the following information, where applicable:

- Accession codes, unique identifiers, or web links for publicly available datasets
- A description of any restrictions on data availability
- For clinical datasets or third party data, please ensure that the statement adheres to our policy

All relevant data are included in the manuscript and Supplementary Information.

Mass spectrometry data files have been uploaded to the MassIVE proteomics database MSV000093510 (ftp://massive.ucsd.edu/MSV000093510/).

The cryo-EM structural data generated in this study have been deposited in the Protein Data Bank and the Electron Microscopy Data Bank under accession codes EMD-16903 for the 60S-UFM1-E3UFM1 (obtained from the UFM1 pulldown), EMD-16908 and PDB-8OJ8 for the 60S-E3UFM1-SEC61 complex in State 1, EMD-16902 and PDB-8OJ0 for the 60S-UFM1-E3UFM1-SEC61 complex in State 2, EMD-16880 and PDB-8OHD for the 60S-UFM1-E3UFM1 complex in State 3 (States 1, 2 and 3 obtained from the UFL1 pulldown) and EMD-16905 and PDB-8OJ5 for the in vitro reconstituted 60S-UFM1-E3UFM1 complex (State 3).

The structures used for atomic model building of 60S-UFM1-E3UFM1 and 60S-UFM1-E3UFM1-SEC61 complexes are available in Worldwide Protein Data Bank (wwPDB) with accession code 8GLP [https://www.wwpdb.org/pdb?id=pdb_00008glp], 8G5Y [https://www.wwpdb.org/pdb?id=pdb_00008g5y], 6Z6M [https://www.wwpdb.org/pdb?id=pdb_00006z6m] and 6W6L [https://www.wwpdb.org/pdb?id=pdb_00006w6l]

Human research participants

Policy information about studies involving human research participants and Sex and Gender in Research.

Reporting on sex and gender	N/A
Population characteristics	N/A
Recruitment	N/A
Ethics oversight	N/A

Note that full information on the approval of the study protocol must also be provided in the manuscript.

Field-specific reporting

Please select the one below that is the best fit for your research. If you are not sure, read the appropriate sections before making your selection.

☒ Life sciences ☐ Behavioural & social sciences ☐ Ecological, evolutionary & environmental sciences

For a reference copy of the document with all sections, see nature.com/documents/nr-reporting-summary-flat.pdf

Life sciences study design

All studies must disclose on these points even when the disclosure is negative.

Sample size	No calculations or statistical method was used for sample sizes. Experiments were repeated in part or in whole at least twice for all biochemical or functional cell-based assays. For assays in which statistics were pertinent, the sample size was judged based on the effect size and was generally between three and five biological replicates. For a detailed description of each experiment please see the "Statistics and reproducibility" section of Methods. For proteomics experiments, we chose n=1 or n=5 given the limitation of the available TMT channels; all experiments were repeated at least three times independently. Cryo-EM data were collected to yield a sufficient amount of particles for thorough 2D and 3D classification. The exact sample size is variable because of dataset heterogeneity For ligand-bound ribosomal complexes sample sizes of 10,000 - 50,000 micrographs, yielding in approx. 500,000 - 2,000,000 particles images is common practice. All datasets in this study were within this range.
Data exclusions	No data were excluded intentionally, except for removal of common laboratory contaminants from proteomics dataset. During cryo-EM data processing, particles were excluded if their 2D class averages represented noise or didn't show clearly identifable features of a 60S or 80S ribosomal particle.
Replication	For a detailed discussion of replicated data please see the Methods section entitled "Statistics and reproducibility". As indicated above, all experiments were replicated in the same, or extremely similar experiments, in part or in whole on different days. All attempts were successful and no data was excluded from any statistical analyses for which there are biological replicates shown in the manuscript. For proteomics experiments replicates clustered together in PCA, and we observed low coefficient of variation among replicates; for each series of experiments, all replication attempts were successful.
Randomization	For the in vitro work in this manuscript, randomization is not applicable; no group allocations were performed. Proteomics samples for comparison with TMT reagents, were randomly allocated in the TMT group and replicates were in adjacent channels.; To obtain the resolution of cryo-EM reconstructions, the"Gold Standard" Fourier shell correlation (FSC) is measured. Here, data are randomly divided into two halves resulting in two independent 3D maps that were used for the FSC calculation. Randomization is not applicable for all other experiments performed here.
Blinding	No group allocations were performed; blinding is not relevant to the work herein. Blinding was not relevant for proteomics samples, because all the data were analyzed using unbiased methods.; the investigators were not blinded during data collection. For cryo-EM data processing, all steps including data division for FSC calculation are a computer-based, unbiased processes.

Behavioural & social sciences study design

All studies must disclose on these points even when the disclosure is negative.

Study description	*Briefly describe the study type including whether data are quantitative, qualitative, or mixed-methods (e.g. qualitative cross-sectional, quantitative experimental, mixed-methods case study).*
Research sample	*State the research sample (e.g. Harvard university undergraduates, villagers in rural India) and provide relevant demographic information (e.g. age, sex) and indicate whether the sample is representative. Provide a rationale for the study sample chosen. For studies involving existing datasets, please describe the dataset and source.*
Sampling strategy	*Describe the sampling procedure (e.g. random, snowball, stratified, convenience). Describe the statistical methods that were used to predetermine sample size OR if no sample-size calculation was performed, describe how sample sizes were chosen and provide a rationale for why these sample sizes are sufficient. For qualitative data, please indicate whether data saturation was considered, and what criteria were used to decide that no further sampling was needed.*
Data collection	*Provide details about the data collection procedure, including the instruments or devices used to record the data (e.g. pen and paper, computer, eye tracker, video or audio equipment) whether anyone was present besides the participant(s) and the researcher, and whether the researcher was blind to experimental condition and/or the study hypothesis during data collection.*
Timing	*Indicate the start and stop dates of data collection. If there is a gap between collection periods, state the dates for each sample cohort.*
Data exclusions	*If no data were excluded from the analyses, state so OR if data were excluded, provide the exact number of exclusions and the rationale behind them, indicating whether exclusion criteria were pre-established.*
Non-participation	*State how many participants dropped out/declined participation and the reason(s) given OR provide response rate OR state that no participants dropped out/declined participation.*
Randomization	*If participants were not allocated into experimental groups, state so OR describe how participants were allocated to groups, and if allocation was not random, describe how covariates were controlled.*

Ecological, evolutionary & environmental sciences study design

All studies must disclose on these points even when the disclosure is negative.

Study description	*Briefly describe the study. For quantitative data include treatment factors and interactions, design structure (e.g. factorial, nested, hierarchical), nature and number of experimental units and replicates.*
Research sample	*Describe the research sample (e.g. a group of tagged Passer domesticus, all Stenocereus thurberi within Organ Pipe Cactus National Monument), and provide a rationale for the sample choice. When relevant, describe the organism taxa, source, sex, age range and any manipulations. State what population the sample is meant to represent when applicable. For studies involving existing datasets, describe the data and its source.*
Sampling strategy	*Note the sampling procedure. Describe the statistical methods that were used to predetermine sample size OR if no sample-size calculation was performed, describe how sample sizes were chosen and provide a rationale for why these sample sizes are sufficient.*
Data collection	*Describe the data collection procedure, including who recorded the data and how.*
Timing and spatial scale	*Indicate the start and stop dates of data collection, noting the frequency and periodicity of sampling and providing a rationale for these choices. If there is a gap between collection periods, state the dates for each sample cohort. Specify the spatial scale from which the data are taken*
Data exclusions	*If no data were excluded from the analyses, state so OR if data were excluded, describe the exclusions and the rationale behind them, indicating whether exclusion criteria were pre-established.*
Reproducibility	*Describe the measures taken to verify the reproducibility of experimental findings. For each experiment, note whether any attempts to repeat the experiment failed OR state that all attempts to repeat the experiment were successful.*
Randomization	*Describe how samples/organisms/participants were allocated into groups. If allocation was not random, describe how covariates were controlled. If this is not relevant to your study, explain why.*
Blinding	*Describe the extent of blinding used during data acquisition and analysis. If blinding was not possible, describe why OR explain why blinding was not relevant to your study.*

Did the study involve field work? ☐ Yes ☐ No

Field work, collection and transport

Field conditions	*Describe the study conditions for field work, providing relevant parameters (e.g. temperature, rainfall).*
Location	*State the location of the sampling or experiment, providing relevant parameters (e.g. latitude and longitude, elevation, water depth).*
Access & import/export	*Describe the efforts you have made to access habitats and to collect and import/export your samples in a responsible manner and in compliance with local, national and international laws, noting any permits that were obtained (give the name of the issuing authority, the date of issue, and any identifying information).*
Disturbance	*Describe any disturbance caused by the study and how it was minimized.*

Reporting for specific materials, systems and methods

We require information from authors about some types of materials, experimental systems and methods used in many studies. Here, indicate whether each material, system or method listed is relevant to your study. If you are not sure if a list item applies to your research, read the appropriate section before selecting a response.

Materials & experimental systems

n/a	Involved in the study
☐	☒ Antibodies
☐	☒ Eukaryotic cell lines
☒	☐ Palaeontology and archaeology
☒	☐ Animals and other organisms
☒	☐ Clinical data
☒	☐ Dual use research of concern

Methods

n/a	Involved in the study
☒	☐ ChIP-seq
☒	☐ Flow cytometry
☒	☐ MRI-based neuroimaging

Antibodies

Antibodies used

rabbit anti-UFM1, Abcam, Cat# ab109305, dilution, 1:1,000
mouse anti-UFSP2, Santa Cruz Biotechnology, Cat# sc-376084, dilution, 1:1,000
rabbit anti-UFC1, Abcam, Cat# ab189251, dilution, 1:2,000
rabbit anti-UBA5, Proteintech , Cat# 12093-1-AP, dilution, 1:2,000
rabbit anti-DDRGK1, Proteintech, Cat #21445-1-AP, dilution, 1:1,000
rabbit anti-UFL1, Bethyl Laboratories, Cat# A303-456A, dilution, 1:2,000
rabbit anti- CDK5RAP3, Bethyl Laboratories, Cat# A300-870A, dilution, 1:2,000
rabbit anti-RPL26 (uL24), Abcam, Cat # ab59567, dilution, 1:3,000
mouse anti-RPL17 (C-8) (uL22), Santa Cruz Biotechnology, Cat# sc-515904, dilution, 1:2,000
rabbit anti-NEMF, Proteintech, Cat# 11840-1-AP, dilution, 1:2,000
rabbit anti-eIF6, Bethyl Laboratories, Cat# A303-029A, dilution, 1:2,000
mouse anti-FLAG M2, Sigma-Aldrich Cat# F1804, dilution, 1:4,000
mouse anti-GAPDH clone D4C6R, Cell Signaling, 97166S, dilution, 1:5,000
rabbit anti-GAPDH clone 14C10, Cell Signaling, Cat# 2118, dilution, 1:5,000
IRDye 800CW Streptavidin, LI-COR Biosciences, Cat# 925-32230, dilution, 1:5,000
rabbit anti-SEC61β, Gift from Hegde Lab, dilution, 1:2,000
rabbit anti-SEC61α, Gift from Hegde Lab, dilution, 1:1,000
anti-Mouse IgG, IRDye 800CW, LI-COR Biosciences, Cat# 926-32210, RRID: AB_621842, dilution, 1:20,000
anti-Mouse IgG, IRDye 680LT, LI-COR Biosciences, Cat# 926-68020, RRID: AB_10706161, dilution, 1:20,000
anti-Rabbit IgG, IRDye 800CW, LI-COR Biosciences, Cat# 926-32211, RRID: AB_621843, dilution, 1:20,000
anti-Rabbit IgG, IRDye 680LT, LI-COR Biosciences, Cat# 926-68021, RRID: AB_10706309, dilution, 1:20,000

Validation

rabbit anti-UFM1 - Validated for IB by manufacturer, and by knockout experiments in this manuscript and in ref. 2 and 4
mouse anti-UFSP2 - Validated for IB by manufacturer, and by knockout experiments in this manuscript and in ref. 2
rabbit anti-UFC1 - Validated for IB by manufacturer, and by knockout experiments in ref. 2
rabbit anti-UBA5 - Validated for IB by manufacturer, and by knockout experiments in ref. 2, and inducible knockdown experiments in ref. 4
rabbit anti-DDRGK1 - Validated for IB by manufacturer, by knockout experiments in ref. 2, and using purified protein in this manuscript and in ref. 6
rabbit anti-UFL1 - Validated for IB by manufacturer, and with purified UFL1 in this manuscript
rabbit anti-CDK5RAP3 - Validated for IB by manufacturer, in this manuscript and in ref. 6 using purified protein, and by knockout experiments in the Kopito Lab (unpublished).
rabbit anti-RPL26 (uL24) - Validated for IB by manufacturer and in CRISPRi knockdown experiments in ref. 2
mouse anti-RPL17 (C-8) - Validated for IB by manufacturer and using purified 60S ribosome in this manuscript
rabbit anti-NEMF - Validated for IB by manufacturer and by knockout and siRNA knockdown experiments in ref. 4
rabbit anti-eIF6 - Validated for IB by manufacturer and by ribosome co-sedimentation in this manuscript.
Rabbit, anti-SEC61β, Gift from Hegde Lab - validated in Fons RD, Bogert BA, Hegde RS. J Cell Biol. 2003.
Rabbit, anti-SEC61α, Gift from Hegde Lab - validated in Fons RD, Bogert BA, Hegde RS. J Cell Biol. 2003.
mouse anti-FLAG M2 - Validated for IB by manufacturer
mouse anti-GAPDH - Validated for IB by manufacturer
rabbit anti-GAPDH - Validated for IB by manufacturer
IRDye 800CW Streptavidin - Validated for IB by manufacturer
anti-Mouse IgG, IRDye 800CW - Validated for IB by manufacturer
anti-Mouse IgG, IRDye 680LT - Validated for IB by manufacturer
anti-Rabbit IgG, IRDye 800CW - Validated for IB by manufacturer
anti-Rabbit IgG, IRDye 680LT - Validated for IB by manufacturer

Eukaryotic cell lines

Policy information about cell lines and Sex and Gender in Research

Cell line source(s)

Human K562 Cells, ATCC, Cat #CCL-243
Human: HEK293T Cells, ATCC, Cat# CRL-3216
Human: HEK293 Cells, ATCC, Cat# CRL-1573
Human: HEK293 UFM1-KO/UFSP-KO (Walczak et al., 2019)
Human: HEK293 DDRGK1-KO (Walczak et al., 2019)
Human: HEK293 UFSP2-KO (Walczak et al., 2019)
Human: HEK293 UFL1-KO (This study)
Human: HEK293 UFL1-KO + UFL1-3XFLAG (This study)

Human: HEK293 UFL1-KO + UFL1(1-532)-3XFLAG (This study)
Human: HEK293 UFL1-KO + UFL1(1-410)-3XFLAG (This study)
Human: HEK293 UFL1-KO + UFL1(1-116)-3XFLAG (This study)
Human: HEK293 UFM1-KO (Walczak et al., 2019)
Human: HEK293 UFC1-KO (Walczak et al., 2019)
Human: K562 (UCOE) Cas9 (Bassik Lab)
Human: K562 (UCOE) Cas9 UFSP2-KO (This study)
Human: K562 (UCOE) Cas9 UFM1-KO (This study)
Human: HEK293 Flp-In™ T-REx™ Cells, ThermoFisher, Cat#R78007

Authentication	Cell lines were not authenticated except by growth in the appropriate antibiotic for which they have resistance, and/or the confirmation of transgene expression and/or gene knockout.
Mycoplasma contamination	Mycoplama contamination was tested using PCR Mycoplasma Detection Kit (ABM Inc., Cat# G238) and no mycoplasma contaminations were detected.
Commonly misidentified lines (See ICLAC register)	No commonly misidentified cell lines were used.

Palaeontology and Archaeology

Specimen provenance	*Provide provenance information for specimens and describe permits that were obtained for the work (including the name of the issuing authority, the date of issue, and any identifying information). Permits should encompass collection and, where applicable, export.*
Specimen deposition	*Indicate where the specimens have been deposited to permit free access by other researchers.*
Dating methods	*If new dates are provided, describe how they were obtained (e.g. collection, storage, sample pretreatment and measurement), where they were obtained (i.e. lab name), the calibration program and the protocol for quality assurance OR state that no new dates are provided.*

☐ Tick this box to confirm that the raw and calibrated dates are available in the paper or in Supplementary Information.

Ethics oversight	*Identify the organization(s) that approved or provided guidance on the study protocol, OR state that no ethical approval or guidance was required and explain why not.*

Note that full information on the approval of the study protocol must also be provided in the manuscript.

Animals and other research organisms

Policy information about studies involving animals; ARRIVE guidelines recommended for reporting animal research, and Sex and Gender in Research

Laboratory animals	*For laboratory animals, report species, strain and age OR state that the study did not involve laboratory animals.*
Wild animals	*Provide details on animals observed in or captured in the field; report species and age where possible. Describe how animals were caught and transported and what happened to captive animals after the study (if killed, explain why and describe method; if released, say where and when) OR state that the study did not involve wild animals.*
Reporting on sex	*Indicate if findings apply to only one sex; describe whether sex was considered in study design, methods used for assigning sex. Provide data disaggregated for sex where this information has been collected in the source data as appropriate; provide overall numbers in this Reporting Summary. Please state if this information has not been collected. Report sex-based analyses where performed, justify reasons for lack of sex-based analysis.*
Field-collected samples	*For laboratory work with field-collected samples, describe all relevant parameters such as housing, maintenance, temperature, photoperiod and end-of-experiment protocol OR state that the study did not involve samples collected from the field.*
Ethics oversight	*Identify the organization(s) that approved or provided guidance on the study protocol, OR state that no ethical approval or guidance was required and explain why not.*

Note that full information on the approval of the study protocol must also be provided in the manuscript.

Clinical data

Policy information about clinical studies

All manuscripts should comply with the ICMJE guidelines for publication of clinical research and a completed CONSORT checklist must be included with all submissions.

Clinical trial registration	*Provide the trial registration number from ClinicalTrials.gov or an equivalent agency.*
Study protocol	*Note where the full trial protocol can be accessed OR if not available, explain why.*

Data collection	*Describe the settings and locales of data collection, noting the time periods of recruitment and data collection.*
Outcomes	*Describe how you pre-defined primary and secondary outcome measures and how you assessed these measures.*

Dual use research of concern

Policy information about dual use research of concern

Hazards

Could the accidental, deliberate or reckless misuse of agents or technologies generated in the work, or the application of information presented in the manuscript, pose a threat to:

No	Yes	
☒	☐	Public health
☒	☐	National security
☒	☐	Crops and/or livestock
☒	☐	Ecosystems
☒	☐	Any other significant area

Experiments of concern

Does the work involve any of these experiments of concern:

No	Yes	
☒	☐	Demonstrate how to render a vaccine ineffective
☒	☐	Confer resistance to therapeutically useful antibiotics or antiviral agents
☒	☐	Enhance the virulence of a pathogen or render a nonpathogen virulent
☒	☐	Increase transmissibility of a pathogen
☒	☐	Alter the host range of a pathogen
☒	☐	Enable evasion of diagnostic/detection modalities
☒	☐	Enable the weaponization of a biological agent or toxin
☒	☐	Any other potentially harmful combination of experiments and agents

ChIP-seq

Data deposition

☐ Confirm that both raw and final processed data have been deposited in a public database such as GEO.

☐ Confirm that you have deposited or provided access to graph files (e.g. BED files) for the called peaks.

Data access links *May remain private before publication.*	*For "Initial submission" or "Revised version" documents, provide reviewer access links. For your "Final submission" document, provide a link to the deposited data.*
Files in database submission	*Provide a list of all files available in the database submission.*
Genome browser session (e.g. UCSC)	*Provide a link to an anonymized genome browser session for "Initial submission" and "Revised version" documents only, to enable peer review. Write "no longer applicable" for "Final submission" documents.*

Methodology

Replicates	*Describe the experimental replicates, specifying number, type and replicate agreement.*
Sequencing depth	*Describe the sequencing depth for each experiment, providing the total number of reads, uniquely mapped reads, length of reads and whether they were paired- or single-end.*
Antibodies	*Describe the antibodies used for the ChIP-seq experiments; as applicable, provide supplier name, catalog number, clone name, and lot number.*
Peak calling parameters	*Specify the command line program and parameters used for read mapping and peak calling, including the ChIP, control and index files used.*
Data quality	*Describe the methods used to ensure data quality in full detail, including how many peaks are at FDR 5% and above 5-fold enrichment.*

Software | *Describe the software used to collect and analyze the ChIP-seq data. For custom code that has been deposited into a community repository, provide accession details.*

Flow Cytometry

Plots

Confirm that:

☐ The axis labels state the marker and fluorochrome used (e.g. CD4-FITC).

☐ The axis scales are clearly visible. Include numbers along axes only for bottom left plot of group (a 'group' is an analysis of identical markers).

☐ All plots are contour plots with outliers or pseudocolor plots.

☐ A numerical value for number of cells or percentage (with statistics) is provided.

Methodology

Sample preparation	*Describe the sample preparation, detailing the biological source of the cells and any tissue processing steps used.*
Instrument	*Identify the instrument used for data collection, specifying make and model number.*
Software	*Describe the software used to collect and analyze the flow cytometry data. For custom code that has been deposited into a community repository, provide accession details.*
Cell population abundance	*Describe the abundance of the relevant cell populations within post-sort fractions, providing details on the purity of the samples and how it was determined.*
Gating strategy	*Describe the gating strategy used for all relevant experiments, specifying the preliminary FSC/SSC gates of the starting cell population, indicating where boundaries between "positive" and "negative" staining cell populations are defined.*

☐ Tick this box to confirm that a figure exemplifying the gating strategy is provided in the Supplementary Information.

Magnetic resonance imaging

Experimental design

Design type	*Indicate task or resting state; event-related or block design.*
Design specifications	*Specify the number of blocks, trials or experimental units per session and/or subject, and specify the length of each trial or block (if trials are blocked) and interval between trials.*
Behavioral performance measures	*State number and/or type of variables recorded (e.g. correct button press, response time) and what statistics were used to establish that the subjects were performing the task as expected (e.g. mean, range, and/or standard deviation across subjects).*

Acquisition

Imaging type(s)	*Specify: functional, structural, diffusion, perfusion.*
Field strength	*Specify in Tesla*
Sequence & imaging parameters	*Specify the pulse sequence type (gradient echo, spin echo, etc.), imaging type (EPI, spiral, etc.), field of view, matrix size, slice thickness, orientation and TE/TR/flip angle.*
Area of acquisition	*State whether a whole brain scan was used OR define the area of acquisition, describing how the region was determined.*

Diffusion MRI ☐ Used ☐ Not used

Preprocessing

Preprocessing software	*Provide detail on software version and revision number and on specific parameters (model/functions, brain extraction, segmentation, smoothing kernel size, etc.).*
Normalization	*If data were normalized/standardized, describe the approach(es): specify linear or non-linear and define image types used for transformation OR indicate that data were not normalized and explain rationale for lack of normalization.*
Normalization template	*Describe the template used for normalization/transformation, specifying subject space or group standardized space (e.g. original Talairach, MNI305, ICBM152) OR indicate that the data were not normalized.*

Noise and artifact removal

Describe your procedure(s) for artifact and structured noise removal, specifying motion parameters, tissue signals and physiological signals (heart rate, respiration).

Volume censoring

Define your software and/or method and criteria for volume censoring, and state the extent of such censoring.

Statistical modeling & inference

Model type and settings

Specify type (mass univariate, multivariate, RSA, predictive, etc.) and describe essential details of the model at the first and second levels (e.g. fixed, random or mixed effects; drift or auto-correlation).

Effect(s) tested

Define precise effect in terms of the task or stimulus conditions instead of psychological concepts and indicate whether ANOVA or factorial designs were used.

Specify type of analysis: ☐ Whole brain ☐ ROI-based ☐ Both

Statistic type for inference
(See Eklund et al. 2016)

Specify voxel-wise or cluster-wise and report all relevant parameters for cluster-wise methods.

Correction

Describe the type of correction and how it is obtained for multiple comparisons (e.g. FWE, FDR, permutation or Monte Carlo).

Models & analysis

n/a	Involved in the study
☐	☐ Functional and/or effective connectivity
☐	☐ Graph analysis
☐	☐ Multivariate modeling or predictive analysis

Functional and/or effective connectivity

Report the measures of dependence used and the model details (e.g. Pearson correlation, partial correlation, mutual information).

Graph analysis

Report the dependent variable and connectivity measure, specifying weighted graph or binarized graph, subject- or group-level, and the global and/or node summaries used (e.g. clustering coefficient, efficiency, etc.).

Multivariate modeling and predictive analysis

Specify independent variables, features extraction and dimension reduction, model, training and evaluation metrics.

SCIENCE ADVANCES | RESEARCH ARTICLE

CELL BIOLOGY

UFMylation orchestrates spatiotemporal coordination of RQC at the ER

Ivan Penchev[1]†, Samantha Gumbin[2]†, Francesco Scavone[2], Otto Berninghausen[1], Thomas Becker[1], Ron Kopito[2]*, Roland Beckmann[1]*

Degradation of arrest peptides from endoplasmic reticulum (ER) translocon-bound 60*S* ribosomal subunits via the ribosome-associated quality control (ER-RQC) pathway requires covalent modification of RPL26/uL24 on 60*S* ribosomal subunits with UFM1. However, the underlying mechanism that coordinates the UFMylation and RQC pathways remains elusive. Structural analysis of ER-RQC intermediates revealed concomitant binding and direct interaction of the UFMylation and RQC machineries on the 60*S*. In the presence of an arrested peptidyl–transfer RNA, the RQC factor NEMF and the UFM1 E3 ligase ($E3^{UFM1}$) form a direct interaction via the UFL1 subunit of $E3^{UFM1}$, and UFL1 adopts a conformation distinct from that previously observed for posttermination 60*S*. While this concomitant binding occurs on translocon-bound 60*S*, LTN1 recruitment and arrest peptide degradation require UFMylation-dependent 60*S* dissociation from the translocon. These data reveal a mechanism by which the UFMylation cycle orchestrates ER-RQC.

INTRODUCTION

Despite the highly processive nature of protein synthesis, ribosomes can stall while translating mRNA, generating ribosomes that are incapacitated by truncated peptidyl-tRNA adducts that obstruct the P-site and clog the exit tunnel. Ribosome-associated quality control (RQC) recognizes these aberrant ribosomes, ensuring efficient extraction and degradation of potentially toxic arrested polypeptides (APs) and recycling of the 60*S* subunit (*1*, *2*). RQC impairment is linked to neurodevelopmental and neurodegenerative phenotypes, suggesting that this pathway plays a key role in maintaining proteostasis (*3*–*6*).

In RQC, splitting of stalled 80*S* ribosomes yields a free 40*S* subunit and a 60*S* subunit that contain an AP covalently bound to a tRNA in the P-site (P-tRNA). The AP-tRNA is recognized by nuclear export mediation factor (NEMF), a component of the core RQC machinery (*1*, *7*–*10*) that catalyzes template-less translation (TLT), resulting in polymerization of additional amino acids at the C terminus of the P-tRNA (*6*, *9*, *11*). These so-called C-terminal alanine and threonine (CAT) tails are composed predominantly of alanine in humans (*6*) and a mixture of alanine and threonine in yeast (*9*). NEMF promotes TLT by delivering aminoacylated-tRNAs to the A-site, mimicking the canonical translation elongation cycle and extending the AP in a process called CATylation (*6*, *9*, *11*). NEMF also recruits the E3 ubiquitin ligase listerin (LTN1) to P-tRNA-60*S*, allowing LTN1 to position its catalytic RING domain adjacent to the peptide exit tunnel to ubiquitylate the AP, enabling ubiquitin-dependent AP extraction from the ribosome and degradation by the 26*S* proteasome (*1*, *7*, *8*, *12*). CAT tails have been suggested to facilitate AP extraction and degradation by extruding lysine residues that are initially buried in the exit tunnel, allowing them to access cytosolic ubiquitylation machinery including LTN1 (*13*), or by serving as degrons to ensure efficient destruction of aggregation-prone, cytotoxic APs that escape LTN1-mediated ubiquitylation (*14*–*16*).

Ribosome stalls can also occur during cotranslational translocation of secretory and membrane proteins at the endoplasmic reticulum (ER), resulting in P-tRNA-60*S* docked at SEC61 translocons (*17*–*19*). These ER-APs are likely to be partially translocated across the ER membrane, clogging both the SEC61 translocon and the 60*S* exit tunnel. Like cytosolic APs, ER-APs are also degraded by a proteasome-mediated process that requires CATylation by NEMF and ubiquitylation by LTN1 (*17*, *18*). However, ER-RQC differs from cytosolic RQC by requiring covalent conjugation of the ubiquitin-like protein UFM1 (UFMylation) to uL24 (also known as RPL26), a core 60*S* protein situated directly adjacent to the translocon docking site (*20*, *21*). UFMylation is highly selective, with the ER membrane–anchored UFM1 E3 ligase ($E3^{UFM1}$) predominantly modifying a single lysine residue (K134) on uL24 of translocon-docked 60*S* (*20*, *21*).

Genetic and biochemical studies (*17*) suggested a model in which UFMylation facilitates ER-RQC by disrupting the ribosome-translocon junction, thereby enabling cytosolic ubiquitin conjugation machinery like LTN1 to access lysine residues on ER-APs that would otherwise be obscured by the translocon and the ER membrane bilayer. These ubiquitylated ER-APs are extracted from the translocon and the exit tunnel by p97/VCP and degraded by cytosolic proteasomes (*17*). In the absence of RQC or UFMylation machinery, ER-APs are not properly extracted into the cytosol for degradation but are instead released into the ER lumen (*17*), where they can form toxic aggregates that could potentially escape the cell via the secretory pathway. These considerations highlight the need for precise spatiotemporal coordination of UFMylation-mediated 60*S*-translocon dissociation with P-tRNA cleavage and ER-AP ubiquitylation to ensure efficient degradation of ER-APs by cytosolic proteasomes.

The recently reported structures of $E3^{UFM1}$ bound to posttermination (i.e., release factor mediated, nonstall) 60*S* complexes (*22*, *23*) provide mechanistic insight into how UFMylation promotes ribosome-translocon dissociation. Single-particle cryo–electron microscopy (cryo-EM) analysis of 60*S* particles affinity

[1]Department of Biochemistry, Gene Center, Feodor-Lynen-Str. 25, University of Munich, 81377, Munich, Germany. [2]Department of Biology, Stanford University, Stanford, CA 94305, USA.
*Corresponding author. Email: kopito@stanford.edu (R.K.); beckmann@genzentrum.lmu.de (R.B.)
†These authors contributed equally to this work.

purified with E3^{UFM1}, a heterotrimeric complex composed of UFL1, DDRGK1, and CDK5RAP3, from untreated wild-type (WT) cells identified three distinct conformational states that differed in terms of the E3^{UFM1} conformation and the presence or absence of conjugated UFM1 and the SEC61 translocon (*22*). Two E3^{UFM1}-bound 60*S* structures, corresponding to states before and after UFM1 transfer to uL24, exhibited clear densities corresponding to the SEC61 translocon. By contrast, in the third state, the SEC61 density on UFMylated 60*S* was absent, instead replaced by an α-helical domain of the DDRGK1 subunit of E3^{UFM1}. These structures, together with biochemical data (*22*, *23*), suggest that, following normal termination, uL24 UFMylation promotes dissociation of 60*S* from ER translocons. The structures of E3^{UFM1} bound to post-termination 60*S* support our hypothesis that UFMylation promotes ER-RQC by releasing the 60*S* from the translocon, thus enabling the ubiquitin-proteasome system (UPS) machinery to access ER-APs obscured by the translocon and the ER membrane. However, the previously reported conformation of UFL1 bound to posttermination 60*S* is incompatible with the known structures of RQC-60*S*, because the ER-AP and NEMF would obstruct the previously observed binding sites for the UFL1 C-terminal domain (CTD) and PTC loop (*22*, *23*). This clash suggests a fundamental incompatibility of the RQC and UFMylation machineries to operate on the same 60*S* particle, despite genetic evidence that these machineries must cooperate (*17*, *22*).

In this study, we used single-particle cryo-EM of E3^{UFM1}-bound P-tRNA-60*S* particles captured from anisomycin (ANM)–treated cells to resolve this conundrum. We find that during ER-RQC, the UFL1 CTD adopts a rotated conformation on P-tRNA-60*S* that does not occupy the A- and P-tRNA binding sites. In this conformation, part of the mostly unstructured, 79–amino acid region of UFL1 that encompasses the PTC loop (the "loop domain") forms a β-augmented interface with NEMF. Structure-directed mutational analysis demonstrates that direct interaction between NEMF and UFL1 is critical for coordinating P-tRNA cleavage, UFMylation-mediated translocon release, and ER-AP ubiquitylation, which must occur in a precise temporal sequence to ensure ER-AP extraction to the cytosol for degradation. We present an ensemble of cryo-EM structures of ER-RQC that support a model in which UFMylation plays a central role in coordinating the temporal and spatial order of events in ER-RQC.

RESULTS

E3^{UFM1} adopts an alternate conformation on RQC-60*S*

We affinity captured ER-RQC-60*S* complexes via the tagged UFL1 subunit of E3^{UFM1} (3xFLAG-UFL1) from cells that were challenged with ANM to induce ribosome collisions and subsequent RQC (Fig. 1A) (*24*). Mass spectrometric analysis (data S1) of this sample identified E3^{UFM1}, 60*S*, SEC61, and the RQC factors, NEMF and LTN1, suggesting that E3^{UFM1} and RQC factors can coexist on the same 60*S* ribosomal subunits at the ER. We then performed a single-particle cryo-EM analysis that revealed four major classes of ER-RQC intermediates that were affinity captured with UFL1 in addition to the previously observed posttermination E3^{UFM1} complexes (fig. S1). The ratio of posttermination E3^{UFM1} complexes to ER-RQC complexes is roughly 10:1, suggesting that UFMylation acts in ER-RQC in addition to its primary role in posttermination 60*S* recycling. Among the ER-RQC states, the best-resolved class (fig. S2A) contained E3^{UFM1}, NEMF, a peptidyl-tRNA in the P-site (fig. S2A), and LTN1 bound to the same 60*S* subunit (E3^{UFM1}-RQC-60*S*; Fig. 1, B to D). A molecular model for

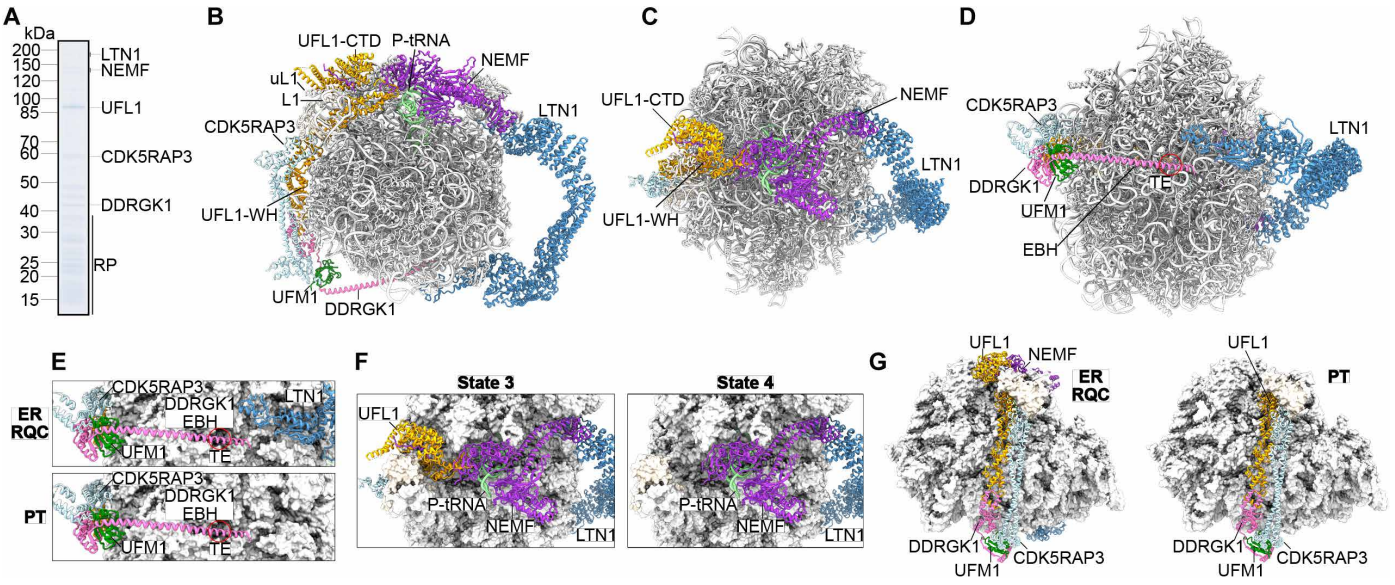

Fig. 1. Cryo-EM structure of the E3^{UFM1}-RQC-60*S* complex. (**A**) Coomassie-stained SDS–polyacrylamide gel electrophoresis (SDS-PAGE) gel of a 3xFLAG-UFL1 pulldown from cells challenged with ANM. (**B** to **D**) Molecular model of the E3^{UFM1}-RQC-60*S* (RQC state 3) complex, shown as a side view on the intersubunit space (B), a top view (C), and a bottom view on the peptide tunnel exit (D). (**E** to **G**) Comparison of the E3^{UFM1}-RQC-60*S* complex with the posttermination E3^{UFM1}-60*S* complex (*22*) and RQC-60*S* complex (RQC state 4) (E) view of the tunnel exit region, (F) comparison of the E3^{UFM1}-RQC-60*S* structure (RQC state 3) with the RQC-60*S* class (RQC state 4, no E3^{UFM1} bound) obtained from this study (see also Fig. 4D and figs. S1 and S2), and (G) view focusing on the overall position of the E3^{UFM1}. Molecular models in (E) to (G) are rendered as surfaces for the 60*S* and as ribbons for nonribosomal ligands. TE, tunnel exit; EBH, exit binding helix of DDRGK1; CTD, UFL1 C-terminal domain; WH, UFL1 winged helix domain; PT, posttermination.

this map, which we refer to as "RQC state 3" (fig. S1), was built, initially guided by previous structures (*22*) and AlphaFold [see Materials and Methods, Fig. 1 (B to D), fig. S3 (A to C), and table S1] (*25*–*27*).

In the structure of RQC state 3 (Fig. 1, B to D), NEMF is observed in a previously identified intermediate state of the CATylation cycle, namely, the postinitiation/predecoding TLT intermediate before accommodation of the next A-site tRNA [state E in yeast cytosolic RQC (*11*); fig. S4]. In this state, NEMF contacts the P-tRNA, which is in the P^{RQC} conformation [as observed in yeast complexes (*11*)] via its NFACT domains, while the connecting coiled-coil-middle (CC-M) domain of NEMF contacts the 60*S* stalk base at the sarcin-ricin loop, as well as uL11 and LTN1 (*7*). As described before (*7*, *9*, *11*, *28*), LTN1's HEAT repeats arch over the 60*S* toward the peptide tunnel exit (Fig. 1, B to D), while its RING domain is located in close proximity to the long N-terminal α helix of DDRGK1 [exit binding helix (EBH)] (Fig. 1, D and E).

We also observed a RQC-60*S* complex, RQC state 4 (fig. S1), in which $E3^{UFM1}$ was not visible. This state likely arose from dissociation of the UFMylation machinery before cryo-EM analysis. LTN1 and NEMF are in virtually identical conformations in RQC states 3 and 4 (Fig. 1F), except for the notable difference that NEMF's NFACT-C domain is more rigid in RQC state 3 (fig. S2C). This conformational stabilization of NEMF's NFACT-C domain by $E3^{UFM1}$, together with the occupancy of the E-site by UFL1, suggests that NEMF's CATylation activity is likely to be paused upon $E3^{UFM1}$ binding.

RQC state 3 (Fig. 2A) differs substantially from the previously reported posttermination $E3^{UFM1}$-60*S* structures (Fig. 2B) (*22*, *23*) in that UFL1's globular CTD is markedly repositioned, and a part of

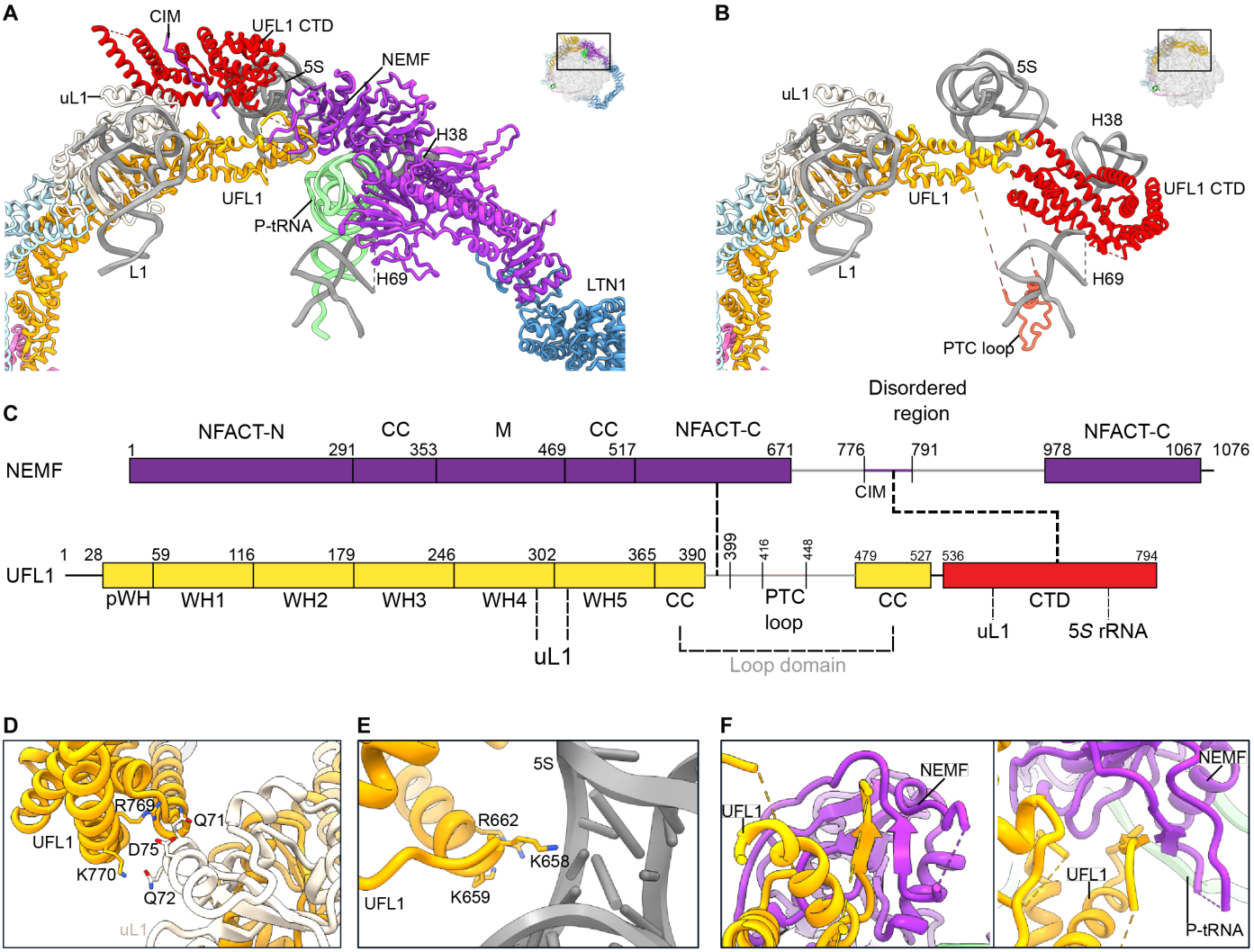

Fig. 2. Conformational change of the UFL1 C terminus and its interaction with NEMF. (**A** and **B**) Molecular models of the $E3^{UFM1}$-RQC-60*S* complex (RQC state 3) (A) and $E3^{UFM1}$-60*S* complex (posttermination state) (*22*) (B). View focuses on the tRNA binding sites in the 60*S* intersubunit space, and thumbnails indicate the orientation. Note that in the $E3^{UFM1}$-RQC-60*S* complex, the UFL1 C terminus flips toward the L1 stalk and uL1 protein. (**C**) Schematic representation of NEMF and UFL1 domain organization and interactions between them. The vertical dashed line marks the site of the β-augmented residues. (**D** to **F**) Close-up views on the interactions between the UFL1 CTD and (D) uL1 (white), (E) 5*S* rRNA (gray), and (F) the NEMF C-terminal NFACT domain (violet; two views). CTD, UFL1 C-terminal domain; CIM, CTD-interacting motif of NEMF; WH, winged helix; CC, coiled-coil (NEMF and UFL1); M, middle domain of NEMF; NFACT, domain found in NEMF, FbpA, Caliban, and Tae2.

the PTC loop–containing loop domain (Fig. 2C) establishes a direct interaction with NEMF. Otherwise, the overall architecture of E3^{UFM1} in the E3^{UFM1}-RQC-60*S* structures is nearly identical to its conformation on posttermination E3^{UFM1}-60*S* (*22*, *23*). In both, E3^{UFM1} forms a clamp-like structure (Fig. 1G) where the EBH of DDRGK1 spans from the peptide exit tunnel toward UFMylated uL24 (Fig. 1E), and the UFL1-CDK5RAP3 winged helix scaffold reaches toward the L1 stalk (Fig. 1G). Thus, repositioning of UFL1's CTD and loop domain allows E3^{UFM1} and the RQC factors NEMF and LTN1 to coexist on the same ER-AP containing 60*S* particles.

In the posttermination E3^{UFM1}-60*S* complex (*22*, *23*), the UFL1 CTD occupies the A- and P-sites, being locked between ribosomal RNA (rRNA) helices H38 (A-site finger) and H69 (Fig. 2B) (*22*, *23*). However, in RQC state 3, this space is occupied by the P-tRNA and NEMF, and UFL1's CTD is rotated backward by approximately 150° into a position between ribosomal protein uL1 and 5*S* rRNA (Fig. 2, A and C). Two basic patches in the UFL1 CTD (R769/K770 and K658/K659/R662) are likely to stabilize this conformation by interacting with complementary acidic patches in either uL1 (Q71/Q72/D75) or the backbone of 5*S* rRNA (Fig. 2, D and E). Notably, a region of UFL1 encompassing amino acids N390 to E399 interacts with a portion of NEMF's NFACT-C domain (Fig. 2, A, C, and F, and fig. S3, D to F). Specifically, the UFL1-NEMF interface displays a β-augmentation of the residues S634-M636 of NEMF with the residues H394-I396 of UFL1, which are part of the PTC loop domain (Fig. 2C) (*22*, *23*). In the posttermination 60*S* conformation of UFL1 (*22*, *23*) (posttermination state 3), the mostly unstructured PTC loop domain occupies the P-site, and the α-helical PTC loop is localized at the PTC (Fig. 2B). In contrast, in RQC state 3 (Fig. 3A), the P-site is occupied by the P-tRNA and NEMF, and the region of the PTC loop containing the small α-helical segment is delocalized and unresolved. In addition to the interface between UFL1 and

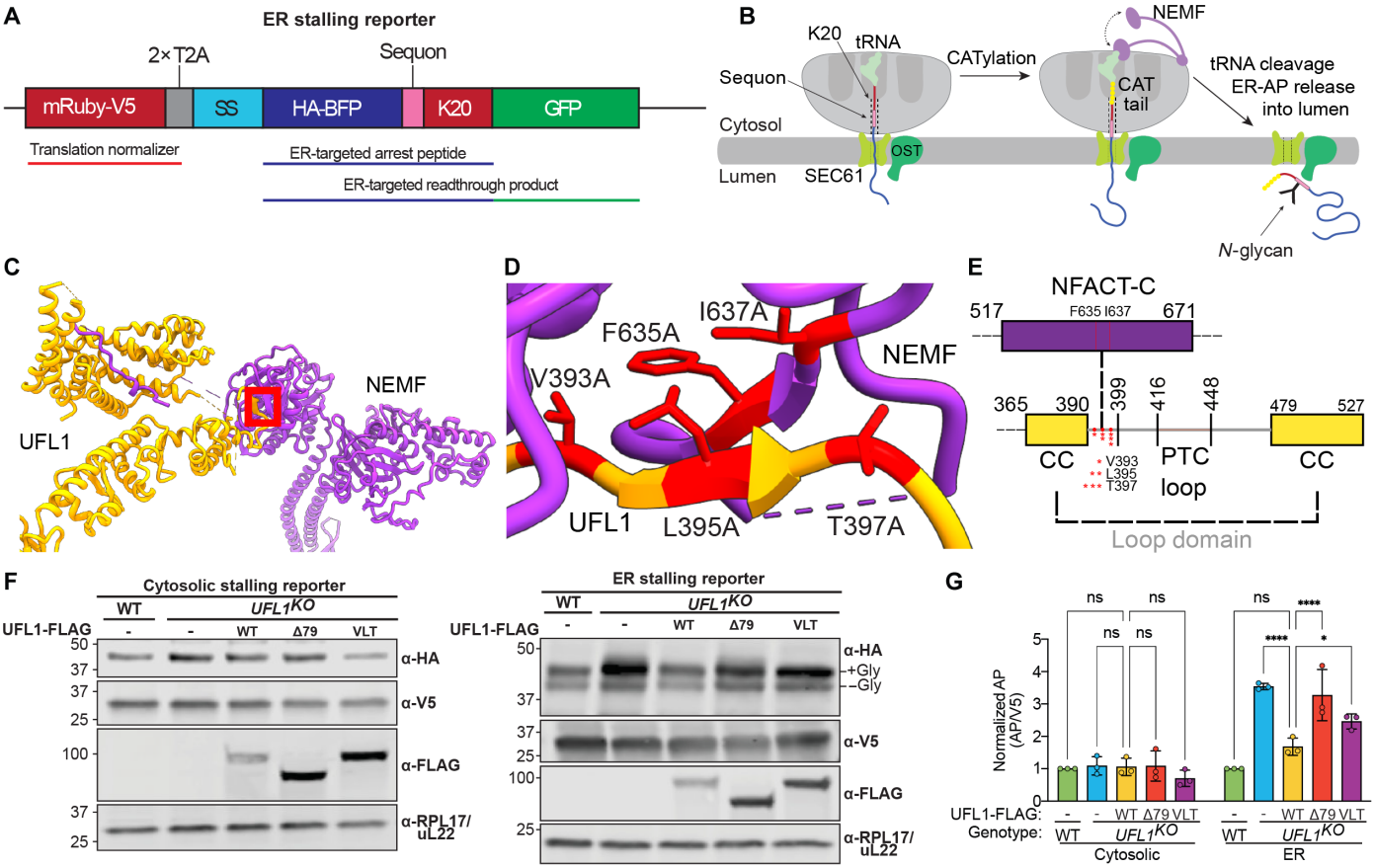

Fig. 3. ER-AP but not cytosolic AP clearance depends on interaction between NEMF and UFL1. (**A**) Schematic of the ER-targeted stalling reporters contained the following features: mRuby; V5 epitope tag; T2A (*Thosea asigna* virus 2A) peptide bond skipping sequences; signal sequence (SS) from bovine preprolactin; hemagglutinin epitope tag; blue fluorescent protein (BFP); *N*-glycosylation sequon; polylysine (K20) stalling sequence; superfolder green fluorescent protein (GFP). The protein species produced by each stalling reporter are indicated. (**B**) Model of the ER-targeted stalling reporter on a 60*S* ribosome at the ER. When the ER-AP is still attached to the ribosome by a P-tRNA, the *N*-glycosylation sequon is retained in the ribosome exit tunnel and is inaccessible to the glycosylation machinery in the ER lumen. If the ER-AP is released from the 60*S* and P-tRNA, then it will enter the ER lumen, and the sequon will be glycosylated. (**C**) Position of NEMF-UFL1 β-augmentation interface (red box). (**D** and **E**) Residues mutated in VLT UFL1, shown as molecular model (D) or schematic representation (E). The vertical dashed line marks the site of the β-augmented residues. (**F**) Degradation of ER but not cytosolic APs depends on UFL1-NEMF interaction. UFL1-dependent degradation of ER-AP but not cytosolic AP in WT or *UFL1*^{KO} cells stably rescued with WT, but not mutant Δ79 (deletion of residues L395-E473) and VLT (V393A/L395A/T397A) UFL1-FLAG. (**G**) Quantification of cytosolic and ER-AP reporter intensities from data in (F). For ER-APs, the sum of the −Gly and +Gly bands are quantified. Data show mean V5 normalized fold change ± SD relative to *UFL1*^{KO} cells rescued with WT UFL1-FLAG, *P* value from the indicated comparison derived from two-way analysis of variance (ANOVA) of $n = 3$ biological replicates. ns, not significant. $^{*}P > 0.05$, $^{****}P > 0.0001$.

NEMF formed by β-augmentation, we observed a short stretch of the disordered region of NEMF interacting with the concave surface of the UFL1 CTD, which we named the CTD-interacting motif of NEMF (Fig. 2, A and C, and fig. S3, G to I).

Together, the structure of the E3^{UFM1}-RQC-60*S* shows that the UFMylation and RQC machineries can concomitantly engage the ER-AP containing 60*S*. The ability of E3^{UFM1} to engage posttermination 60*S* and RQC-60*S* is enabled by the capacity of the UFL1's CTD to adopt either of two alternate conformations. Notably, this observation solves the conundrum of P-tRNA-60*S* recognition by E3^{UFM1} raised by the clash of UFL1's CTD in the posttermination conformation with P-tRNA or NEMF.

UFL1-NEMF interface coordinates ER-RQC

To test the functional importance of the UFL1-NEMF interaction, we focused on the β-augmentation interface between UFL1 and NEMF, since it stabilizes the NFACT-C domain of NEMF in a rigid conformation (fig. S2C). We monitored the effect of mutations of key residues at this interface on turnover of cytoplasmic- and ER-targeted APs using modified versions of our previously described ER-targeted and cytosolic stalling reporters (Fig. 3, A to E) (*17*). Inclusion of an *N*-glycosylation sequon in the ER-targeted reporter directly upstream of the K20 stall sequence allows glycosylation status to distinguish ER-APs that are released into the ER lumen (sequon glycosylated) from those that remain ribosome bound (sequon sequestered in the exit tunnel not glycosylated) (Fig. 3, A and B). The normalized steady-state levels of the stalling reporters serve as a proxy for degradation (*17*). As expected, neither knockout of *UFL1* nor rescue of *UFL1*^{KO} cells with UFL1 variants affected the cytosolic stalling reporter, as UFMylation is dispensable for cytosolic RQC (Fig. 3, F and G) (*17*). By contrast, knockout of *UFL1* caused substantial accumulation of the glycosylated ER reporter (Fig. 3, F and G, "+Gly," and fig. S5A), confirming our previous observation that UFL1 is essential for ER-AP degradation and that, in the absence of UFMylation, ER-APs are fully released into and are stabilized in the ER lumen (*17*). This defect was rescued by reexpression of WT UFL1, but not of a UFL1 variant (Δ79) that lacks the loop domain, or a variant harboring mutations predicted to disrupt the β-augmented NEMF interface on UFL1 (V393A/L395A/T397A; "VLT") (Fig. 3, C to G, and fig. S5A). We conclude that this interaction serves to prevent ER-AP release into the ER lumen.

We attempted to confirm these findings by rescuing *NEMF*^{KO} cells with NEMF variants harboring mutations in key residues on the β strand that contribute to this interface (F635A/I637A; "FI"). Reexpression of WT NEMF in *NEMF*^{KO} cells robustly rescued the defect in degradation of cytosolic, but not ER-targeted stalling reporters (fig. S5, B and C) (*17*), suggesting that *NEMF*^{KO} cells had adapted to the engineered deletion by becoming partially NEMF independent. All four *NEMF*^{KO} clones had elevated steady-state levels of uL24 UFMylation (fig. S5D), which could not be returned to WT levels by reexpressing NEMF (fig. S5E). The observation that transient knockdown of NEMF does not induce hyper-UFMylation (*17*) suggests that elevated UFMylation is an adaptive strategy to survive the selective impact of chronic NEMF depletion on ER-RQC and consistent with the high coessential dependency between UFMylation genes and *NEMF* (*29*) and the synthetic lethality between *NEMF* and *UFM1* (*17*). Because of adaptations to the loss of ER-RQC in the *NEMF*^{KO} clones, we could not draw conclusions about the contribution of specific amino acid residues on the NEMF side of the UFL1 β-augmented interface in RQC. However, the UFL1 rescue experiments strongly support an essential role of this interaction in ER-RQC (Fig. 3, F and G). Further studies will be required to understand how uL24 hyper-UFMylation and perhaps additional undiscovered adaptive changes contribute to cell survival in the absence of NEMF.

In addition to considering a model in which the interaction between NEMF and UFL promotes ER-AP release, we also considered a model in which the direct physical interaction of NEMF with UFL1 could facilitate ER-RQC by promoting uL24 UFMylation. However, we ruled out this model because UFMylation is not impaired upon NEMF knockdown, even in ANM-treated cells, suggesting that UFM1 conjugation occurs independently of NEMF (*17*). Moreover, we observed similar levels of UFL1 and UFMylated uL24 cofractionated in ribosomal pellets from ANM-treated *UFL1*^{KO} cells rescued with both WT and VLT variants of UFL1 (fig. S6A). Therefore, disruption of the NEMF-UFL1 interface does not inhibit either E3^{UFM1} binding or UFMylation in response to ribosome stalling. By contrast, deletion of the entire loop domain (Δ79), which includes the PTC loop and the NEMF β-augmented interface, or the PTC loop alone (Δ32) impairs UFMylation (fig. S6A), suggesting that this region contributes to the stable binding of E3^{UFM1} to posttermination-60*S* and RQC-60*S* independently of the UFL1-NEMF β-augmented interface.

Cryo-EM reveals distinct snapshots of ER-RQC

Apart from the E3^{UFM1}-RQC-60*S* (RQC state 3) and RQC-60*S* (RQC state 4) structures shown above (Figs. 1 and 2), two additional RQC-60*S* structures were identified in our cryo-EM dataset from the ANM-challenged UFL1-pulldown sample (Fig. 4, A to D, and fig. S1). The first structure (RQC state 1; Fig. 4A) contains the SEC61 complex and NEMF bound to non-UFMylated P-tRNA-60*S* in the same conformation as observed in the E3^{UFM1}-RQC-60*S* structure (RQC state 3) (Fig. 1, B to D). While we cannot directly prove that this state is part of the UFMylation cycle, we speculate that it corresponds to recently split ER membrane–bound P-tRNA-60*S* to which NEMF has bound and has presumably begun synthesizing CAT tails, which is consistent with biochemical evidence showing that ER-AP CATylation can occur in the absence of UFMylation (*17*). Since all particles in this study were captured by UFL1 pulldown, the absence of visible density corresponding to UFMylation machinery in RQC states 1 and 4 possibly reflects that E3^{UFM1}, weakly associated in the absence of tight binding to UFMylated uL24, was either highly delocalized or had dissociated during sample preparation.

In the next intermediate (RQC state 2; Fig. 4B), NEMF, P-tRNA, and SEC61 are all positioned as in RQC state 1, with the addition of UFMylated uL24 and the tightly bound E3^{UFM1}, which is fully resolved except for the EBH of DDRGK1, which is not yet positioned to dislocate SEC61, as in posttermination state 2 (*22*). RQC state 2 confirms that, even in the UFL1 CTD rotated conformation and with the β-augmented interface with NEMF (Fig. 1), E3^{UFM1} is still able to catalyze uL24 modification. eIF6 was observed in RQC states 1 and 2 and a subset of RQC state 3 particles. We did not observe eIF6 in RQC state 4 particles.

RQC state 3 (Fig. 4C) is the best-resolved structure shown in Fig. 1. Its most notable features are the conspicuous absence of density corresponding to SEC61, which is replaced by the DDRGK1 EBH, and the presence of LTN1. As previously reported for posttermination

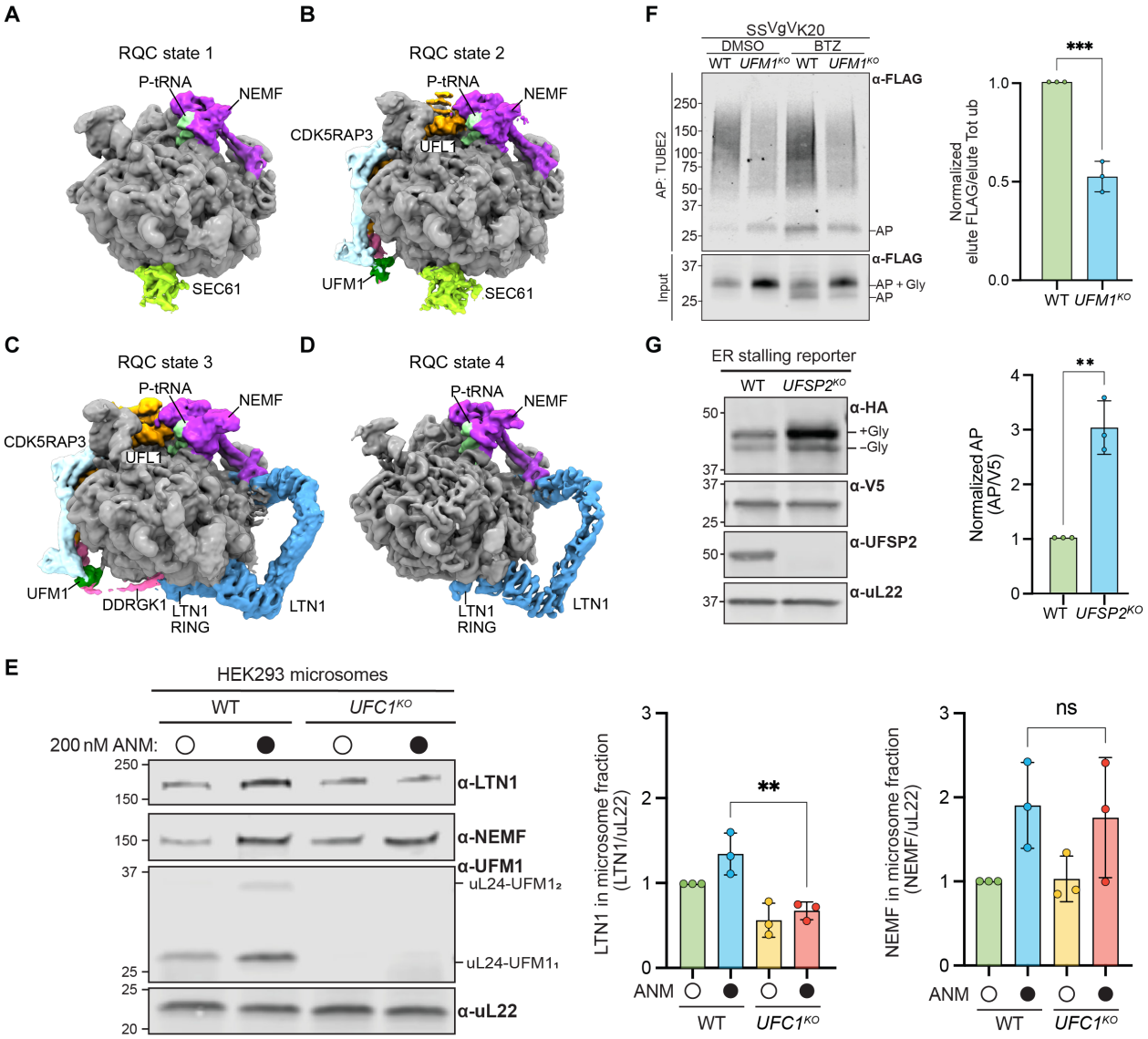

Fig. 4. UFMylation promotes SEC61 displacement and LTN1 binding. (**A** to **D**) Cryo-EM density maps of the four main classes found in the ANM-challenged UFL1 immunoprecipitation. (A) RQC state 1, a SEC61-bound ER-RQC intermediate with NEMF bound to a P-tRNA. (B) RQC state 2, same as (A) but with the $E3^{UFM1}$ bound to uL24-UFMylated 60*S*. (C) RQC state 3, $E3^{UFM1}$-60*S*-RQC complex as shown in Fig. 1. Compared to (B), no SEC61 is visible, instead the DDRGK1 EBH is positioned below the tunnel exit and LTN1 is bound. (D) RQC state 4, same as (C) but lacking the $E3^{UFM1}$. (**E**) LTN1 binding to ribosomes at the ER depends on UFMylation. Microsomes derived from WT or *UFC1*^{KO} HEK293 cells were treated with ANM and analyzed by immunoblot. Quantification is from $n = 3$ biological replicates, fold change ± SD relative to WT cells, *P* value from the indicated comparison derived from one-way ordinary ANOVA of $n = 3$ biological replicates. $^{**}P = 0.0052$. (**F**) Loss of UFM1 reduces ER-AP ubiquitylation. WT or *UFM1*^{KO} HEK293 cells transfected with $SS^{VgV}K20$ from (*17*) were treated with dimethyl sulfoxide (DMSO) or BTZ for 4 hours before isolation of Ub conjugates using pan-ubiquitin (TUBE2) agarose. Quantification is from $n = 3$ biological replicates from TUBE affinity purification in the presence of BTZ. Data show mean FLAG smear in elution/total ubiquitin smear in elution (fig. S8), fold change ± SD relative to WT cells, *P* value from the indicated comparison derived from unpaired *t* test, $^{***}P = 0.0004$. (**G**) Loss of UFSP2 accumulates ER-APs. Human embryonic kidney (HEK) 293 WT or *UFSP2*^{KO} cells were transfected with the ER-targeted stalling reporter and analyzed by immunoblot. For ER-APs, both the −Gly and +Gly bands are quantified. Data show mean V5 normalized fold change ± SD relative to WT cells, *P* value from the indicated comparison derived from unpaired *t* test of $n = 3$ biological replicates, $^{**}P = 0.0021$.

60*S*, SEC61 displacement occurs after conjugation of UFM1 to uL24, which stabilizes DDRGK1 EBH at the tunnel exit (Figs. 1 and 4C) (*22*, *23*). We never observed particles in which RQC-60*S* was simultaneously bound to both SEC61 and LTN1. This mutually exclusive binding can be explained by the steric clash between the translocon (and the ER membrane) with the RING domain and adjacent regions of LTN1 (fig. S7), supporting the conclusion that displacement of P-tRNA-60*S* from SEC61 must temporally precede recruitment of LTN1. It is also likely that SEC61 engagement by 60*S* would sterically hinder not only LTN1 engagement but also access of an activated E2 ubiquitin–conjugating enzyme to lysine residues on ER-AP.

To test this model, we assessed the impact of disrupting UFMylation on the binding of endogenous LTN1 to ER-bound ribosomes in response to ANM-induced ribosome collisions. ANM treatment

increased the amount of NEMF associated with microsomes from both WT and UFMylation E2–deficient (*UFC1*^{KO}) cells, confirming that UFMylation does not interfere with NEMF binding (Fig. 4E). By contrast, ANM treatment caused the amount of microsome-bound LTN1 to increase only in WT cells, suggesting that UFMylation-dependent displacement of 60*S* from ER translocons is a prerequisite for LTN1 engagement (Fig. 4E). We also observed that ER-AP ubiquitylation was significantly reduced in *UFM1*^{KO} compared to WT cells, consistent with impaired access of LTN1 to ER-AP in the absence of UFMylation (Fig. 4F and fig. S8).

RQC state 4 [Figs. 1F (right) and 4D] features 60*S* bound to P-tRNA, NEMF, and LTN1 in conformations similar to RQC state 3 but lacks densities corresponding to SEC61, E3^{UFM1}, and UFM1 on uL24, suggesting that it could possibly represent RQC-60*S* after translocon dissociation and uL24 deUFMylation. We found that ER-AP levels were strongly elevated in the absence of the deUFMylase, UFSP2, suggesting that deUFMylation may be necessary for ER-AP degradation (Fig. 4G). While we cannot provide direct evidence that the observed structures are directly linked in the same pathway, the suggested scenario represents the simplest and most plausible interpretation.

DISCUSSION

Our structural and biochemical observations suggest a model for ER-RQC (Fig. 5). After translational stalling and 80*S* ribosome splitting, P-tRNA-60*S* remains bound to the SEC61 translocon and is recognized by NEMF, which CATylates the ER-AP (RQC state 1; Fig. 4A). Following CATylation, E3^{UFM1}, with the UFL1 CTD in the rotated conformation, binds to RQC state 1, where it forms a β-augmented interface with NEMF, giving rise to RQC state 2 (Fig. 4B). Further research will be needed to identify what, if any additional signal is required for E3^{UFM1} to bind to RQC state 1.

We hypothesize that this binding mode of UFL1 has two consequences for the CATylation activity of NEMF. First, the translocation of any deacylated tRNA from the P-site into the E-site is prevented by the presence of E3^{UFM1} in the E-site. Second, the interaction between the UFL1 loop domain and the NEMF NFACT-C domain stabilizes NEMF's conformation on the 60*S* subunit, as suggested by comparably higher local resolution (fig. S2C). As the β-augmentation interaction likely restrains the conformational flexibility of NEMF necessary for efficiently promoting the TLT cycle for CATylation (*11*), we propose that CATylation is stalled by the NEMF-UFL1 interaction. This, along with the observation that CAT tail length is unaffected by loss of UFMylation (*17*), suggests a model in which CAT tails are formed before E3^{UFM1} binding to the RQC-60*S*, although it is possible that that CATylation may resume after translocon release and deUFMylation. Further study will be needed to determine whether the UFL1-NEMF interaction influences CAT tail composition or length, and how this could contribute to ER-AP degradation.

Disruption of this β-augmented interface results in lumenal accumulation of the glycosylated form of the ER-targeted reporter, pointing to premature peptidyl-tRNA cleavage and failed ER-RQC–mediated extraction of the ER-AP to the cytosol (Fig. 3, F and G). This supports a model in which the UFL1-NEMF β-augmented interaction halts CATylation, keeping NEMF in a conformation over the P-tRNA where it could potentially protect it from hydrolysis, delaying cleavage by nucleases or hydrolases such as ANKZF1 or Ptrh1 (*30*–*32*). Unfortunately, exactly how CATylation termination by ANKZF1 (or Ptrh1) is triggered and the exact role NEMF plays in termination is not understood. Previous reports (*30*–*32*) suggest that NEMF (Rqc2 in yeast) has an inhibitory effect on ANKZF1's activity (Vms1 in yeast), in agreement with our model.

Transfer of UFM1 onto uL24 results in tight binding of E3^{UFM1} to 60*S* and displacement of 60*S* from the SEC61 translocon (*22*, *23*), enabling LTN1's RING domain to access the ER-AP which was previously inaccessible (RQC state 3; Fig. 1, B to D). Critically, cleavage of the P-tRNA must occur after ubiquitylation of ER-AP to allow for extraction of ER-AP by an ubiquitin-dependent AAA+ adenosine triphosphatase like p97/VCP (*12*, *17*). If the P-tRNA is cleaved before translocon release or ubiquitylation, then there is nothing to prevent the entire ER-AP from being pulled into the ER lumen, evading degradation by the UPS. CATylated APs are highly

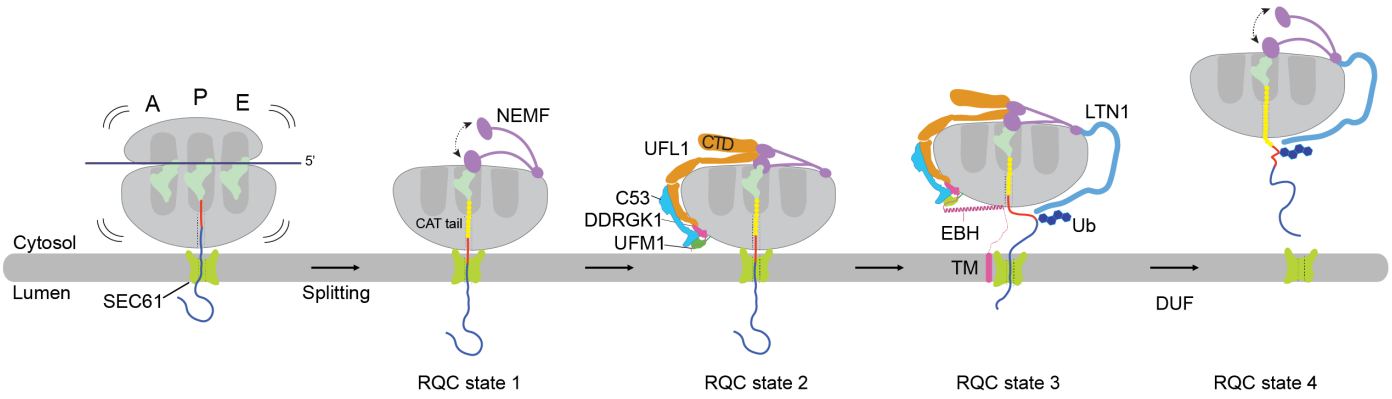

Fig. 5. Model for E3^{UFM1} and RQC cooperation in ER-RQC. Stalled, translocon-docked ribosomes are split, yielding a translocon-engaged 60*S* subunit with a peptidyl-tRNA in the P-site, an ER-AP clogging the exit tunnel and the SEC61 translocon (RQC state 1). As in cytosolic RQC, binding of NEMF to the P-tRNA and empty A-site initiates TLT, forming a CAT tail (yellow circles) on the AP. Double headed arrows denote conformational flexibility of the NEMF NFACT-C domain. In RQC state 2, E3^{UFM1} is bound with UFL1 CTD in the rotated conformation, forming a stabilizing interface with NEMF to pause TLT, and E3^{UFM1} catalyzes the transfer of UFM1 to uL24. In RQC state 3, the EBH of DDRGK1 is stabilized at the tunnel exit, promoting dissociation of 60*S* from SEC61 and allowing LTN1 to position its RING domain near the tunnel exit to ubiquitylate the ER-AP. DeUFMylation allows E3^{UFM1} to dissociate, producing RQC state 4 in which the NEMF NFACT-C domain regains its mobility and the P-tRNA-60*S* complex is no longer tethered to the ER membrane by E3^{UFM1}. DUF, DeUFMylation enzyme, UFSP2.

aggregation prone (*15*, *16*, *33*), making these APs likely to be problematic if retained in the lumen or secreted.

We propose that deUFMylation-mediated release of $E3^{UFM1}$ in the transition to RQC state 4 restores mobility to the NEMF NFACT-C domain, enabling peptidyl tRNA cleavage by ANKZF1 or other nucleases/hydrolases. Therefore, deUFMylation is another critical step in choreography of ER-RQC, by ensuring that P-tRNA cleavage can only occur after release of the SEC61 translocon from P-tRNA-60*S*. This coordination ensures that ER-APs that are released upon cleavage of the P-tRNA are efficiently degraded by cytosolic proteasomes instead of being translocated into the ER lumen.

MATERIALS AND METHODS

Mammalian cell culture

Human embryonic kidney (HEK) 293 cells (American Type Culture Collection) were maintained in Dulbecco's modified Eagle's medium (DMEM)–high glucose (Cytiva) supplemented with 10% fetal bovine serum. Cell lines were grown in a humidified incubator at 37°C and 5% CO_2. All cell lines were routinely tested for mycoplasma infection using a polymerase chain reaction (PCR) mycoplasma detection kit according to the manufacturer's instructions (ABM Inc.).

Mammalian cell transfections

For reporter transfections, HEK293 cells were transfected using Lipofectamine 3000 (Thermo Fisher Scientific, L3000015) according to the manufacturer's instructions. Transfected cells were cultured for 24 to 48 hours before being processed for downstream analysis.

Plasmids

Plasmids and DNA constructs were generated using standard PCR and site-directed mutagenesis techniques using NEBNext High-Fidelity PCR Master Mix (New England Biolabs) and verified by sequencing. Lentiviral vectors for the expression of UFL1 were generated from a modified pLVX vector with an EF1α promoter and a blasticidin selection marker. All lentivirus packaging vectors were obtained from Addgene. To generate stalling reporter sequences, mRuby-V5-2xT2A-SS-HA-SBP-BFP-K20 was ordered as a gene block (Genewiz) and inserted into a pcDNA3.1 parent vector containing a cytomegalovirus promoter and green fluorescent protein downstream of the insertion. The cytosolic variant of the reporter was generated by standard subcloning methods. $SS^{VgV}K20$ was reported previously (*17*).

Cell line generation

Previously reported $UFL1^{KO}$ and $UFSP2^{KO}$ HEK293 cells were used for this study (*17*, *20*, *22*). Stable UFL1-FLAG expressing HEK293 cells were generated through the lentiviral transduction of $UFL1^{KO}$ cells. Lentivirus was used to produce stable cell lines through transfection of HEK293T cells with third-generation packaging plasmids (pRSV, pMDL, and pVSVG) and a lentiviral vector containing either WT UFL1-FLAG, UFL1-FLAG Δ32 (deletion of residues K417-V448), UFL1-FLAG Δ79 (deletion of residues L395-E473), or UFL1-FLAG V393A/L395A/T397A using TransIT-LT1 transfection reagent (Mirus) according to the manufacturer's instructions and grown for 72 hours before collection of the viral supernatant. The supernatant (medium) containing the viral particles was collected and filtered through a 0.45-μm syringe filter and used fresh. $UFL1^{KO}$ HEK293 cells were infected by reverse transduction; cells were resuspended in the viral supernatant containing polybrene (8 μg ml^{-1}) and plated. The viral supernatant was removed, and cells were provided fresh DMEM and grown for about 72 hours before selection with blasticidin for ~2 weeks, after which cells were used as a polyclonal line.

AP accumulation assay

The ribosome stalling reporter (0.5 or 1 μg of plasmid DNA) was transfected 48 hours before cell collection. Whole cell lysates were prepared in radioimmunoprecipitation assay (RIPA) lysis buffer [50 mM tris (pH 7.6), 150 mM NaCl, 1% NP-40, 0.5% sodium deoxycholate, and 0.1% SDS] with protease inhibitor cocktail (complete, EDTA-free protease inhibitor cocktail; Roche) and 1 mM phenylmethylsulfonyl fluoride (PMSF). The total protein concentration was determined for each sample using a Pierce BCA Protein Assay kit (23225). Normalized samples were analyzed by SDS–polyacrylamide gel electrophoresis (SDS-PAGE) and hemagglutinin immunoblotting to detect AP produced. The number of biological replicates for each experiment is listed in the legends; bar graphs in Fig. 3G show the means and SD, and significance was determined using two-way analysis of variance (ANOVA).

Glycosidase treatment

HEK293 cells were collected and lysed in RIPA lysis buffer [50 mM tris (pH 7.6), 150 mM NaCl, 1% NP-40, 0.5% sodium deoxycholate, and 0.1% SDS] with protease inhibitor cocktail and 1 mM PMSF. Total protein concentration was determined for each sample with the Pierce BCA Protein Assay Kit (23225) according to the manufacturer's instructions. Protein concentrations were normalized between samples. Samples were denatured and Endo H treated following the manufacturer's protocols (New England Biolabs Inc., P0702L). Reactions were incubated at 37°C for 1 hour and then analyzed by SDS-PAGE and immunoblotting.

Sucrose cushion sedimentation

Cells were collected and lysed in 1% Triton lysis buffer [20 mM tris (pH 7.5), 150 mM NaCl, 5 mM $MgCl_2$, and 1% Triton X-100] with protease inhibitor cocktail, 1 mM PMSF, and 1 mM dithiothreitol (DTT). Total protein concentration was determined for each sample with the Pierce 600 nm Protein Assay Reagent according to the manufacturer's protocol. Samples were centrifuged at 100,000 rpm for 1 hour at 4°C through a 1 M sucrose cushion in 1% Triton lysis buffer. Pellets were washed once with ice-cold H_2O and resuspended in 1× Laemmli buffer containing 2-mercaptoethanol 5% (v/v) by heating at 100°C for 5 min. Samples were analyzed by SDS-PAGE and immunoblotting.

SDS-PAGE and immunoblotting

Proteins were denatured in 1× Laemmli buffer containing 2-mercaptoethanol 5% (v/v) by heating at 100°C for 5 min. Samples were then separated by SDS-PAGE [12% tris-glycine gels or "4 to 20% Mini-PROTEAN TGX" (Bio-Rad)] and transferred in a semidry transfer to nitrocellulose following the manufacturer's protocol (Bio-Rad). Nitrocellulose membranes were blocked in Intercept (tris-buffered saline) Blocking Buffer to reduce nonspecific antibody binding and incubated with primary antibodies diluted in PBS-T containing 0.1% Tween 20 and 5% bovine serum albumin. Immunoreactivity was detected using fluorescent IRDye secondary antibodies and scanning by Odyssey imaging (LI-COR Biosciences). Band intensities were quantified by Image Studio Lite software (LI-COR Biosciences).

Polyubiquitin affinity capture and identification of polyubiquitylated ER-APs

HEK293 WT or *UFM1*^{KO} cells were transfected with 2 μg of SS^{VgV}K20 stalling reporter for 48 hours and treated with or without 1 μM BTZ for 4 hours. Cells were harvested by centrifugation at 1000*g* for 5 min, washed thrice with phosphate-buffered saline (PBS), and lysed in 250 μl of lysis buffer [50 mM Hepes (pH 7.35), 150 mM NaCl, 1% NP-40, Roche protease inhibitor cocktail, and 1 mM PMSF] supplemented with 40 mM *N*-ethylmaleimide, 10 mM iodoacetamide, and 50 μM PR-619. Lysates were clarified by centrifuging at 13,000*g* for 10 min and incubated with immobilized tandem ubiquitin binding entity (TUBE2 agarose, LifeSensors, catalog no. UM-402) for 16 hours at 4°C by rotating (0.5 mg of whole cell lysates added to 20 μl of TUBE2-agarose). The agarose was washed twice with high salt buffer [50 mM Hepes (pH 7.35), 500 mM NaCl, and 0.5% NP-40] and once with low salt buffer [50 mM Hepes (pH 7.35), 150 mM NaCl, and 0.5% NP-40] by shaking at 4°C for 10 min. Polyubiquitin conjugates were eluted by boiling beads in the presence of ~50 μl of 2× SDS-PAGE sample buffer. The inputs and eluates were analyzed by immunoblotting for endogenous ubiquitin and FLAG to detect ER-APs.

Preparation of rough microsomes from HEK293 cells

HEK293 WT, *UFC1*^{KO}, or *UFSP2*^{KO} cells (*20*) grown to ~80% confluency in 15-cm plates were treated with 0.2 μM ANM for 20 min. Microsomal membranes were isolated using a protocol that has been previously described and adapted for HEK293 cells (*34*–*36*). Briefly, cells from each 15-cm plate were harvested in 5 ml of ice-cold PBS by pipetting, centrifuged for 5 min at 800*g*, and resuspended in 2.5 ml of lysis buffer [10 mM Hepes-NaOH (pH 7.4), 250 mM sucrose, 2 mM $MgCl_2$, and 0.5 mM DTT] containing protease inhibitor cocktail (complete, EDTA-free protease inhibitor cocktail; Roche) and 1 mM PMSF. Cells were homogenized using a chilled and equilibrated isobiotec cell homogenizer (six single passes, 18 μm clearance) on ice, and lysate was cleared twice (1500*g* for 3 min at 4°C). Microsomes were pelleted at 10,000*g* for 10 min at 4°C, resuspended in 300 μl of microsome buffer [10 mM Hepes-NaOH (pH 7.4), 250 mM sucrose, 1 mM $MgCl_2$, and 0.5 mM DTT] containing protease inhibitor cocktail, PMSF, and RNaseOUT (Thermo Fisher Scientific), and pelleted again (10,000*g* for 10 min at 4°C). The membrane pellets were resuspended in microsome buffer and adjusted to a final concentration of 4 mg/ml.

Statistical analysis

Data are represented as means ± SD unless otherwise stated. The number of independent replicates performed for each experiment is indicated in the figure legends. Western blot band intensities were quantified using Image Studio Lite version 5.2.5 (LI-COR Biosciences) and normalized to translation/expression normalizer (mRuby-V5).

Affinity purification of UFL1-bound ribosomes

Large ribosomal subunits bound to E3^{UFM1} and the RQC complex were purified essentially as described before (*22*) with the main difference being that cells were treated with ANM before harvesting for lysis. Following procedures previously described in (*22*), for purification, HEK293 FlpIn TRex cells with a plasmid expressing C-terminally 3× Flag-tagged UFL1 were grown to 50% confluency, and protein expression of 3xFlag-UFL1 was induced by tetracycline (1 μg/ml). At 22 hours following induction, cells were treated with 200 nM ANM for 20 min before being collected and washed twice with PBS by centrifugation at 127*g* for 10 min. Cells were then resuspended in lysis buffer [150 mM potassium acetate (KOAc), 20 mM Hepes (pH 7.5), 5 mM magnesium chloride ($MgCl_2$), 5% glycerol, 1% digitonin, 1 mM DTT, 0.5 mM sodium fluoride (NaF), 0.1 mM sodium vanadate (Na_3VO_4), and complete EDTA-free protease inhibitor (Roche)] and lysed by sonicating 4 × 10 s with 20 s on ice in between (Branson Sonifier 250). The lysate was clarified by centrifugation at 3166*g* for 15 min and at 36,603*g* for 20 min and then incubated with M2 anti-Flag agarose beads (Sigma-Aldrich) on a rotating wheel for 120 min at 4°C. Beads were washed twice with washing buffer [150 mM KOAc, 20 mM Hepes (pH 7.5), 5 mM $MgCl_2$, 0.1% GDN, 1 mM DTT, 0.5 mM NaF, 0.1 mM Na_3VO_4, and complete EDTA-free protease inhibitor (Roche)] and then once more using final buffer [150 mM KOAc, 20 mM Hepes (pH 7.5), 5 mM $MgCl_2$, 1 mM DTT, and 0.1% GDN]. Beads were transferred onto a 1-ml Mobicol (MoBiTec), washed with 5 ml of final buffer, and then incubated with final buffer containing 40 μg of 3C protease for 60 min at 4°C. Following elution, the ribosomes were pelleted through a sucrose cushion [20 mM Hepes (pH 7.5), 150 mM potassium acetate, 5 mM $MgCl_2$, 0.1% GDN, and and 1 M sucrose] by centrifugation at 100,000 rpm for 1 hour using a TLA 120.2 rotor, after which the pellet was resuspended in final buffer and used for cryo-EM sample preparation and NuPAGE gel analysis.

Electron microscopy and image processing

Following procedures previously described in (*22*), 3.5 μl of the sample was applied to Quantifoil R3/3 holey carbon grids with 2-nm continuous carbon coating, blotted for 3 s, and then plunge frozen in liquid ethane using a Vitrobot Mark IV. Data collection was performed at 300 keV using a Titan Krios equipped with a SelectrisX Energy Filter and a Falcon4i direct electron detector at a pixel size of 0.727 Å and a defocus range of −0.5 to −3.5 μm and 40 e^- per Å^2 total dose. Gain correction, alignment, and summation of movie frames were performed using MotionCor2 (*37*) with 20 EER frames grouped into one fraction, producing 40 fractions with 1 e^- per Å^2 dose per fraction. Contrast transfer function (CTF) parameters were estimated using CTFFIND4 (*38*). Collected micrographs were automatically filtered for CTF resolution (maximum 6 Å) and astigmatism (maximum 8), resulting in a total of 45,093 micrographs being selected.

Following procedures previously described in (*22*), particle picking was performed using crYOLO (*39*), with a total of 1,412,867 particles picked. Following two-dimensional (2D) classification in cryoSPARC (*40*), 1,027,683 ribosomal particles were selected. The particles were then 3D classified in Relion (*41*, *42*) using a soft mask around the 40*S* subunit, resulting in a small subset featuring a previously described pre-60*S* harboring NMD3, LSG1, and ZNF622 (*43*), a mixture of stalled or hibernating 80*S* ribosomes, and a major subset featuring various 60*S* states. Here, extra density was already visible for E3^{UFM1} and for RQC factors. Thus, the 60*S* class was classified further using a mask around the binding site for RQC factors NEMF and LTN1. This revealed three distinct classes featuring RQC subunits, two of which were at sufficient resolution to be further classified.

The first subset featured NEMF in the absence of LTN1, as well as the SEC61 translocon. 3D classification with a mask around the tRNA binding sites followed by another round of classification around the E3^{UFM1} binding site led to two final classes that were both refined to resolutions of 2.8 and 3.0 Å, respectively, and used for interpretation. The first, dubbed here as RQC state 1 (see also

Fig. 4A), featured only NEMF, a P-site tRNA, and the SEC61 translocon (NEMF-SEC61-60*S*). The second (RQC state 2; Fig. 4B) also showed not only NEMF, a P-site tRNA, and SEC61 but also $E3^{UFM1}$ ligase (E3-NEMF-SEC61-60*S*) in a conformation identical to the previously described posttermination state 2 (posttermination state 2) (*22*), with the exception of the UFL1 C terminus, which was flipped back and the PTC loop was remodeled.

The second subset featured both NEMF and LTN1 but no SEC61. 3D classification around the $E3^{UFM1}$ binding site revealed two classes lacking the E3 and featuring only NEMF, LTN1, and a P-site tRNA, with minor conformational differences of NEMF between the two (NEMF conformations 1 and 2). Both classes were refined, but only the larger and better resolved "NEMF conformation 2" class (2.8 Å) was used for interpretation, here termed RQC state 4 (Figs. 1F and 4D). A third class resulting from 3D classification with the $E3^{UFM1}$ mask featured NEMF, LTN1, a P-tRNA, and the entire $E3^{UFM1}$, in a conformation similar to posttermination state 3 (posttermination state 3). As a fourth class, we identified a minor state featuring NEMF, LTN1, a P-tRNA, and partial occupancy of the UFL1 CTD in flipped conformation but lacking UFM1, thus likely representing a state where the $E3^{UFM1}$ only partially dissociated from the RQC-60*S*. The class featuring both RQC and E3 complexes was classified further, this time with a mask around the tRNA binding sites. This revealed two states, one featuring only a P-site tRNA and another featuring an A-site tRNA with partial occupancy for a P-site tRNA. For the latter class, however, we were unable to reach sufficient local resolution for the ligands due to the small particle number. The former (featuring only a P-site tRNA) was further refined, and multibody refinement in RELION (*44*) was used to achieve higher local resolution for the bound ligands. Multibody refinement was done by splitting the particle in three parts—the 60*S* core, LTN1 alone, and $E3^{UFM1}$ ligase together with NEMF and the P-tRNA. The focused refined maps were then combined into a composite map using Phenix (*45*), resulting in the best-resolved E3-RQC-60*S* map (RQC state 3; Fig. 4C). Postprocessing via DeepEMhancer (*46*) was used to assist with model building and interpretation of the density map. All important steps of image processing are summarized in fig. S1.

Model building and refinement

Following procedures previously described in (*22*), the best-resolved state (RQC state 3) was used to generate a model for the ER-RQC substrate. The previously generated model for the 60*S*-bound UFM1 E3 ligase (*22*) [Protein Data Bank (PDB) identifier 8ohd] was used as a template for the ribosomal backbone and E3 ligase. The template was largely unchanged with the exception of the UFL1 C terminus, which was refitted into the rotated conformation using Coot (*47*) and Isolde (*48*). In addition, the NEMF-interacting region (residues 390 to 399) was built using a combination of de novo modeling and AlphaFold Multimer (*26*) predictions. The extra density around the UFL1 CTD was identified via de novo modeling as NEMF residues 776 to 791, which was then confirmed via AlphaFold3 (*27*) prediction using the CTD and the region NEMF around said residues (770 to 800).

Following procedures previously described in (*22*), AlphaFold2 models were used for NEMF, LTN1, as well as ribosomal proteins uL10 and uL11. The proteins were initially rigid-body fitted using Coot (v.0.9.8.92) and then fine-tuned using Isolde. The NFACT_N domain of NEMF and parts of the coiled-coil were primarily rigid-body docked due to insufficient resolution, whereas most of the middle domain and a large part of the NFACT_C domain could be fitted at a side-chain resolution. Unlike in the yeast homolog Rqc2, we did not observe density for the hook domain. For LTN1, parts of the N- and C-terminal regions could be fitted at a side-chain level; however, most of the HEAT repeats constituting the backbone could only be rigid-body fitted. The RING domain of LTN1 was also rigid-body fitted. Ribosomal proteins uL10 and uL11 were docked into the density, with minimal adjustments necessary to fit the well resolved regions. A model for the alanyl-tRNA was generated using AlphaFold3 and fitted into the density map.

The complete model was refined using Phenix and then fine-tuned using Isolde. Figures of the model and densities were generated using ChimeraX (*49*).

Supplementary Materials

The PDF file includes:

Figs. S1 to S8
Table S1
Legend for dataset S1

Other Supplementary Material for this manuscript includes the following:

Dataset S1

REFERENCES AND NOTES

1. O. Brandman, J. Stewart-Ornstein, D. Wong, A. Larson, C. C. Williams, G.-W. Li, S. Zhou, D. King, P. S. Shen, J. Weibezahn, J. G. Dunn, S. Rouskin, T. Inada, A. Frost, J. S. Weissman, A ribosome-bound quality control complex triggers degradation of nascent peptides and signals translation stress. *Cell* **151**, 1042–1054 (2012).
2. S. Filbeck, F. Cerullo, S. Pfeffer, C. A. P. Joazeiro, Ribosome-associated quality-control mechanisms from bacteria to humans. *Mol. Cell* **82**, 1451–1466 (2022).
3. A. Ahmed, M. Wang, G. Bergant, R. Maroofian, R. Zhao, M. Alfadhel, M. Nashabat, M. T. AlRifai, W. Eyaid, A. Alswaid, C. Beetz, Y. Qin, T. Zhu, Q. Tian, L. Xia, H. Wu, L. Shen, S. Dong, X. Yang, C. Liu, L. Ma, Q. Zhang, R. Khan, A. A. Shah, J. Guo, B. Tang, L. Leonardis, K. Writzl, B. Peterlin, H. Guo, S. Malik, K. Xia, Z. Hu, Biallelic loss-of-function variants in NEMF cause central nervous system impairment and axonal polyneuropathy. *Hum. Genet.* **140**, 579–592 (2021).
4. P. B. Martin, Y. Kigoshi-Tansho, R. B. Sher, G. Ravenscroft, J. E. Stauffer, R. Kumar, R. Yonashiro, T. Müller, C. Griffith, W. Allen, D. Pehlivan, T. Harel, M. Zenker, D. Howting, D. Schanze, E. A. Faqeih, N. A. M. Almontashiri, R. Maroofian, H. Houlden, N. Mazaheri, H. Galehdari, G. Douglas, J. E. Posey, M. Ryan, J. R. Lupski, N. G. Laing, C. A. P. Joazeiro, G. A. Cox, NEMF mutations that impair ribosome-associated quality control are associated with neuromuscular disease. *Nat. Commun.* **11**, 4625 (2020).
5. J. Chu, N. A. Hong, C. A. Masuda, B. V. Jenkins, K. A. Nelms, C. C. Goodnow, R. J. Glynne, H. Wu, E. Masliah, C. A. P. Joazeiro, S. A. Kay, A mouse forward genetics screen identifies LISTERIN as an E3 ubiquitin ligase involved in neurodegeneration. *Proc. Natl. Acad. Sci. U.S.A.* **106**, 2097–2103 (2009).
6. T. Udagawa, M. Seki, T. Okuyama, S. Adachi, T. Natsume, T. Noguchi, A. Matsuzawa, T. Inada, Failure to degrade CAT-tailed proteins disrupts neuronal morphogenesis and cell survival. *Cell Rep.* **34**, 108599 (2021).
7. S. Shao, A. Brown, B. Santhanam, R. S. Hegde, Structure and assembly pathway of the ribosome quality control complex. *Mol. Cell* **57**, 433–444 (2015).
8. M. H. Bengtson, C. A. P. Joazeiro, Role of a ribosome-associated E3 ubiquitin ligase in protein quality control. *Nature* **467**, 470–473 (2010).
9. P. S. Shen, J. Park, Y. Qin, X. Li, K. Parsawar, M. H. Larson, J. Cox, Y. Cheng, A. M. Lambowitz, J. S. Weissman, O. Brandman, A. Frost, Protein synthesis. Rqc2p and 60S ribosomal subunits mediate mRNA-independent elongation of nascent chains. *Science* **347**, 75–78 (2015).
10. T. Inada, R. Beckmann, Mechanisms of translation-coupled quality control. *J. Mol. Biol.* **436**, 168496 (2024).
11. P. Tesina, S. Ebine, R. Buschauer, M. Thoms, Y. Matsuo, T. Inada, R. Beckmann, Molecular basis of eIF5A-dependent CAT tailing in eukaryotic ribosome-associated quality control. *Mol. Cell* **83**, 607–621.e4 (2023).
12. Q. Defenouillère, Y. Yao, J. Mouaikel, A. Namane, A. Galopier, L. Decourty, A. Doyen, C. Malabat, C. Saveanu, A. Jacquier, M. Fromont-Racine, Cdc48-associated complex bound to 60S particles is required for the clearance of aberrant translation products. *Proc. Natl. Acad. Sci. U.S.A.* **110**, 5046–5051 (2013).

13. K. K. Kostova, K. L. Hickey, B. A. Osuna, J. A. Hussmann, A. Frost, D. E. Weinberg, J. S. Weissman, CAT-tailing as a fail-safe mechanism for efficient degradation of stalled nascent polypeptides. *Science* **357**, 414–417 (2017).
14. C. S. Sitron, O. Brandman, CAT tails drive degradation of stalled polypeptides on and off the ribosome. *Nat. Struct. Mol. Biol.* **26**, 450–459 (2019).
15. A. Thrun, A. Garzia, Y. Kigoshi-Tansho, P. R. Patil, C. S. Umbaugh, T. Dallinger, J. Liu, S. Kreger, A. Patrizi, G. A. Cox, T. Tuschl, C. A. P. Joazeiro, Convergence of mammalian RQC and C-end rule proteolytic pathways via alanine tailing. *Mol. Cell* **81**, 2112–2122.e7 (2021).
16. Y.-J. Choe, S.-H. Park, T. Hassemer, R. Körner, L. Vincenz-Donnelly, M. Hayer-Hartl, F. U. Hartl, Failure of RQC machinery causes protein aggregation and proteotoxic stress. *Nature* **531**, 191–195 (2016).
17. F. Scavone, S. C. Gumbin, P. A. Da Rosa, R. R. Kopito, RPL26/uL24 UFMylation is essential for ribosome-associated quality control at the endoplasmic reticulum. *Proc. Natl. Acad. Sci. U.S.A.* **120**, e2220340120 (2023).
18. S. Arakawa, K. Yunoki, T. Izawa, Y. Tamura, S.-I. Nishikawa, T. Endo, Quality control of nonstop membrane proteins at the ER membrane and in the cytosol. *Sci. Rep.* **6**, 30795 (2016).
19. K. von der Malsburg, S. Shao, R. S. Hegde, The ribosome quality control pathway can access nascent polypeptides stalled at the Sec61 translocon. *Mol. Biol. Cell* **26**, 2168–2180 (2015).
20. C. P. Walczak, D. E. Leto, L. Zhang, C. Riepe, R. Y. Muller, P. A. DaRosa, N. T. Ingolia, J. E. Elias, R. R. Kopito, Ribosomal protein RPL26 is the principal target of UFMylation. *Proc. Natl. Acad. Sci. U.S.A.* **116**, 1299–1308 (2019).
21. L. Wang, Y. Xu, H. Rogers, L. Saidi, C. T. Noguchi, H. Li, J. W. Yewdell, N. R. Guydosh, Y. Ye, UFMylation of RPL26 links translocation-associated quality control to endoplasmic reticulum protein homeostasis. *Cell Res.* **30**, 5–20 (2020).
22. P. A. DaRosa, I. Penchev, S. C. Gumbin, F. Scavone, M. Wąchalska, J. A. Paulo, A. Ordureau, J. J. Peter, Y. Kulathu, J. W. Harper, T. Becker, R. Beckmann, R. R. Kopito, UFM1 E3 ligase promotes recycling of 60S ribosomal subunits from the ER. *Nature* **627**, 445–452 (2024).
23. L. Makhlouf, J. J. Peter, H. M. Magnussen, R. Thakur, D. Millrine, T. C. Minshull, G. Harrison, J. Varghese, F. Lamoliatte, M. Foglizzo, T. Macartney, A. N. Calabrese, E. Zeqiraj, Y. Kulathu, The UFM1 E3 ligase recognizes and releases 60S ribosomes from ER translocons. *Nature* **627**, 437–444 (2024).
24. S. Juszkiewicz, V. Chandrasekaran, Z. Lin, S. Kraatz, V. Ramakrishnan, R. S. Hegde, ZNF598 is a quality control sensor of collided ribosomes. *Mol. Cell* **72**, 469–481.e7 (2018).
25. J. Jumper, D. Hassabis, Protein structure predictions to atomic accuracy with AlphaFold. *Nat. Methods* **19**, 11–12 (2022).
26. R. Evans, M. O'Neill, A. Pritzel, N. Antropova, A. Senior, T. Green, A. Žídek, R. Bates, S. Blackwell, J. Yim, O. Ronneberger, S. Bodenstein, M. Zielinski, A. Bridgland, A. Potapenko, A. Cowie, K. Tunyasuvunakool, R. Jain, E. Clancy, P. Kohli, J. Jumper, D. Hassabis, Protein complex prediction with AlphaFold-Multimer. bioRxiv 463034 [Preprint] (2022). https://doi.org/10.1101/2021.10.04.463034.
27. J. Abramson, J. Adler, J. Dunger, R. Evans, T. Green, A. Pritzel, O. Ronneberger, L. Willmore, A. J. Ballard, J. Bambrick, S. W. Bodenstein, D. A. Evans, C.-C. Hung, M. O'Neill, D. Reiman, K. Tunyasuvunakool, Z. Wu, A. Žemgulytė, E. Arvaniti, C. Beattie, O. Bertolli, A. Bridgland, A. Cherepanov, M. Congreve, A. I. Cowen-Rivers, A. Cowie, M. Figurnov, F. B. Fuchs, H. Gladman, R. Jain, Y. A. Khan, C. M. R. Low, K. Perlin, A. Potapenko, P. Savy, S. Singh, A. Stecula, A. Thillaisundaram, C. Tong, S. Yakneen, E. D. Zhong, M. Zielinski, A. Žídek, V. Bapst, P. Kohli, M. Jaderberg, D. Hassabis, J. M. Jumper, Accurate structure prediction of biomolecular interactions with AlphaFold 3. *Nature* **630**, 493–500 (2024).
28. S. Shao, R. S. Hegde, Reconstitution of a minimal ribosome-associated ubiquitination pathway with purified factors. *Mol. Cell* **55**, 880–890 (2014).
29. A. Tsherniak, F. Vazquez, P. G. Montgomery, B. A. Weir, G. Kryukov, G. S. Cowley, S. Gill, W. F. Harrington, S. Pantel, J. M. Krill-Burger, R. M. Meyers, L. Ali, A. Goodale, Y. Lee, G. Jiang, J. Hsiao, W. F. J. Gerath, S. Howell, E. Merkel, M. Ghandi, L. A. Garraway, D. E. Root, T. R. Golub, J. S. Boehm, W. C. Hahn, Defining a cancer dependency map. *Cell* **170**, 564–576.e16 (2017).
30. K. Kuroha, A. Zinoviev, C. U. T. Hellen, T. V. Pestova, Release of ubiquitinated and non-ubiquitinated nascent chains from stalled mammalian ribosomal complexes by ANKZF1 and Ptrh1. *Mol. Cell* **72**, 286–302.e8 (2018).
31. T. Su, T. Izawa, M. Thoms, Y. Yamashita, J. Cheng, O. Berninghausen, F. U. Hartl, T. Inada, W. Neupert, R. Beckmann, Structure and function of Vms1 and Arb1 in RQC and mitochondrial proteome homeostasis. *Nature* **570**, 538–542 (2019).
32. T. Izawa, S.-H. Park, L. Zhao, F. U. Hartl, W. Neupert, Cytosolic protein Vms1 links ribosome quality control to mitochondrial and cellular homeostasis. *Cell* **171**, 890–903.e18 (2017).
33. C. S. Sitron, J. H. Park, J. M. Giafaglione, O. Brandman, Aggregation of CAT tails blocks their degradation and causes proteotoxicity in S. cerevisiae. *PLOS ONE* **15**, e0227841 (2020).
34. M. Ma, R. Dubey, A. Jen, G. V. Pusapati, E. Shishkova, K. A. Overmyer, V. Cormier-Daire, L. Aravind, J. J. Coon, R. Rohatgi, Substrate-directed control of N-glycosylation in the endoplasmic reticulum calibrates signal reception at the cell-surface. bioRxiv 591210 [Preprint] (2024). https://doi.org/10.1101/2024.04.25.591210.
35. A. Sharma, M. Mariappan, S. Appathurai, R. S. Hegde, In vitro dissection of protein translocation into the mammalian endoplasmic reticulum. *Methods Mol. Biol.* **619**, 339–363 (2010).
36. P. Walter, G. Blobel, Preparation of microsomal membranes for cotranslational protein translocation. *Methods Enzymol.* **96**, 84–93 (1983).
37. S. Q. Zheng, E. Palovcak, J.-P. Armache, K. A. Verba, Y. Cheng, D. A. Agard, MotionCor2: Anisotropic correction of beam-induced motion for improved cryo-electron microscopy. *Nat. Methods* **14**, 331–332 (2017).
38. A. Rohou, N. Grigorieff, CTFFIND4: Fast and accurate defocus estimation from electron micrographs. *J. Struct. Biol.* **192**, 216–221 (2015).
39. T. Wagner, F. Merino, M. Stabrin, T. Moriya, C. Antoni, A. Apelbaum, P. Hagel, O. Sitsel, T. Raisch, D. Prumbaum, D. Quentin, D. Roderer, S. Tacke, B. Siebolds, E. Schubert, T. R. Shaikh, P. Lill, C. Gatsogiannis, S. Raunser, SPHIRE-crYOLO is a fast and accurate fully automated particle picker for cryo-EM. *Commun. Biol.* **2**, 218 (2019).
40. A. Punjani, J. L. Rubinstein, D. J. Fleet, M. A. Brubaker, cryoSPARC: Algorithms for rapid unsupervised cryo-EM structure determination. *Nat. Methods* **14**, 290–296 (2017).
41. D. Kimanius, L. Dong, G. Sharov, T. Nakane, S. H. W. Scheres, New tools for automated cryo-EM single-particle analysis in RELION-4.0. *Biochem. J.* **478**, 4169–4185 (2021).
42. D. Kimanius, K. Jamali, M. E. Wilkinson, S. Lövestam, V. Velazhahan, T. Nakane, S. H. W. Scheres, Data-driven regularization lowers the size barrier of cryo-EM structure determination. *Nat. Methods* **21**, 1216–1221 (2024).
43. X. Liang, M.-Q. Zuo, Y. Zhang, N. Li, C. Ma, M.-Q. Dong, N. Gao, Structural snapshots of human pre-60S ribosomal particles before and after nuclear export. *Nat. Commun.* **11**, 3542 (2020).
44. T. Nakane, S. H. W. Scheres, Multi-body refinement of cryo-EM images in RELION. *Methods Mol. Biol.* **2215**, 145–160 (2021).
45. D. Liebschner, P. V. Afonine, M. L. Baker, G. Bunkóczi, V. B. Chen, T. I. Croll, B. Hintze, L. W. Hung, S. Jain, A. J. McCoy, N. W. Moriarty, R. D. Oeffner, B. K. Poon, M. G. Prisant, R. J. Read, J. S. Richardson, D. C. Richardson, M. D. Sammito, O. V. Sobolev, D. H. Stockwell, T. C. Terwilliger, A. G. Urzhumtsev, L. L. Videau, C. J. Williams, P. D. Adams, Macromolecular structure determination using x-rays, neutrons and electrons: Recent developments in Phenix. *Acta Crystallogr. D Struct. Biol.* **75**, 861–877 (2019).
46. R. Sanchez-Garcia, J. Gomez-Blanco, A. Cuervo, J. M. Carazo, C. O. S. Sorzano, J. Vargas, DeepEMhancer: A deep learning solution for cryo-EM volume post-processing. *Commun. Biol.* **4**, 874 (2021).
47. P. Emsley, K. Cowtan, Coot: Model-building tools for molecular graphics. *Acta Crystallogr. D Biol. Crystallogr.* **60**, 2126–2132 (2004).
48. T. I. Croll, ISOLDE: A physically realistic environment for model building into low-resolution electron-density maps. *Acta Crystallogr. D Struct. Biol.* **74**, 519–530 (2018).
49. E. F. Pettersen, T. D. Goddard, C. C. Huang, E. C. Meng, G. S. Couch, T. I. Croll, J. H. Morris, T. E. Ferrin, UCSF ChimeraX: Structure visualization for researchers, educators, and developers. *Protein Sci.* **30**, 70–82 (2021).

Acknowledgments: We thank C. Ungewickell, S. Rieder, and A. Gilmozzi for excellent technical assistance; T. Fröhlich and Laboratory for Functional and Genome Analysis (LAFUGA) for mass spectrometric analyses; M. Wachalska, P. A. DaRosa, and Jingdong Cheng for helpful discussion throughout this work; and C. Riepe for critical reading of the manuscript. **Funding:** This study was supported by grants from the ERC (ADG 885711 Human-Ribogenesis and DFG (BE1814/20-1 and BE1814/22-1) to R.B.; National Institutes of Health grants 1R01GM148477 and 5R01GM074874 to R.K.; and National Institutes of Health training grant T32GM007276 and Stanford Graduate Fellowship to S.G. **Author contributions:** Conceptualization: I.P., S.G., F.S., R.K., and R.B. Data curation: S.G. Formal analysis: S.G. and I.P. Investigation: I.P., S.G., F.S., and O.B. Funding acquisition: R.K., R.B., and S.G. Methodology: I.P., S.G., and F.S. Project administration: R.K. and R.B. Resources: S.G. Supervision: R.K., R.B., and T.B. Writing—original draft: I.P., T.B., and R.B. Writing—review and editing: S.G., R.K., T.B., R.B., and I.P. Validation: S.G., I.P., and F.S. Visualization: I.P., S.G., and T.B. **Competing interests:** The authors declare that they have no competing interests. **Data and materials availability:** All data needed to evaluate the conclusions in the paper are present in the paper and/or the Supplementary Materials. The cryo-EM data as well as models generated and presented in this study have been deposited in the Electron Microscopy Data Bank and Worldwide PDB under the following accession codes: EMD-51681 for the ER-RQC state 3 composite map (PDB accession code: 9gy4); EMD-51682, EMD-51683, and EMD-51684 for ER-RQC state 3 focused refinements (60*S* body, $E3^{UFM1}$ and NEMF, and LTN1, respectively); EMD-51685 for the ER-RQC state 3 consensus refinement map; EMD-51686 for ER-RQC state 4; EMD-51687 for ER-RQC state 2; and EMD-51688 for ER-RQC state 1.

Submitted 2 December 2024
Accepted 27 March 2025
Published 2 May 2025
10.1126/sciadv.adv0435

Abbreviations

3D three-dimensional

A-site aminoacyl-tRNA binding site

aa-tRNA aminoacyl-tRNA

ANKZF1 Ankyrin repeat and zinc finger domain-containing protein 1

CAT C-terminal alanyl and threonyl

CCD Charge-coupled device

Cdc48 Cell division control protein 48

cryo-EM cryo-electron microscopy

CTF contrast transfer function

DED direct electron detector

DQE Detective Quantum Efficiency

EF elongation factor

EJC exon-junction complex

ER endoplasmic reticulum

ER-RQC endoplasmic reticulum specific ribosome quality control

ERAD ER-associated protein decay

ES expansion segment

FEG field emission gun

FSC Fourier Shell Correlation

GTP guanosine-triphosphate

HEAT Huntingtin, elongation factor 3 , protein phosphatase 2A , and TOR1

IC initiation complex

IF initiation factor

ISR integrated stress response

LSU large ribosomal subunit

LTN1 Listerin

MAPK1 Mitogen activated protein kinase 1

MDa Megadalton

Met-tRNA$_i$ initiator methionine-tRNA

MLE maximum likelihood estimation

MPT multi-pass translocon

mRNA messenger RNA

MTF Modulation Transfer Function

NEMF Nuclear export mediation factor

NGD no-go decay

NMD nonsense-mediated decay

NSD non-stop decay

OST olygosaccharyltransferase

P-site peptidyl-tRNA binding site

p97/VCP Valosin-containing protein

PIC pre-initiation complex

PTC peptidyl-transferase center

pWH pseudo-winged helix

RF release factor

RQC ribosome quality control

Rqc1 Ribosome quality control complex subunit 1

Rqc2 Ribosome quality control complex subunit 2

RQT RQC trigger

RSR ribotoxic stress response

S Svedberg

SGD stochastic gradient descent

SNR singal-to-noise ratio

SPA single particle analysis

SRL sarcin-ricin loop

SSU small ribosomal subunit

SURF SMG1-Upf1-eRF1-eRF3

TC ternary complex

TCF25 Transcription factor 25

TEM Transmission-electron microscopy

TLT templateless translation

tRNA transfer RNA

UBL Ubiquitin-like protein

UFL1 E3 UFM1-protein ligase 1

UFM1 Ubiquitin-fold modifier 1

UPR unfolded protein response

ZNF598 Zinc finger protein 598

References

Hon., Abbe (1882). "The Relation of Aperture and Power in the Microscope (continued)." In: *Journal of the Royal Microscopical Society* 2.4, pp. 460–473. DOI: https://doi.org/10.1111/j.1365-2818.1882.tb04805.x. eprint: https://onlinelibrary.wiley.com/doi/pdf/10.1111/j.1365-2818.1882.tb04805.x. URL: https://onlinelibrary.wiley.com/doi/abs/10.1111/j.1365-2818.1882.tb04805.x.

Orlova, E. V. and H. R. Saibil (2011). "Structural Analysis of Macromolecular Assemblies by Electron Microscopy". In: *Chemical Reviews* 111.12. PMID: 21919528, pp. 7710–7748. DOI: 10.1021/cr100353t. eprint: https://doi.org/10.1021/cr100353t. URL: https://doi.org/10.1021/cr100353t.

Glaeser, RM (1971). "Low temperature electron microscopy-radiation damage in crystalline biological materials". In: *JOURNAL DE MICROSCOPIE* 12.1, pp. 133–+.

Knapek, E and J Dubochet (1980). "Beam damage to organic material is considerably reduced in cryo-electron microscopy". In: *Journal of molecular biology* 141.2, pp. 147–161.

Dubochet, J and AW McDowall (1981). "Vitrification of pure water for electron microscopy". In: *Journal of microscopy* 124.3, pp. 3–4.

Dubochet, Jacques et al. (1988). "Cryo-electron microscopy of vitrified specimens". In: *Quarterly reviews of biophysics* 21.2, pp. 129–228.

Zhu, Jun et al. (1997). "Three-dimensional reconstruction with contrast transfer function correction from energy-filtered cryoelectron micrographs: procedure and application to the 70sescherichia coliribosome". In: *Journal of structural biology* 118.3, pp. 197–219.

Erickson, HP and Aaron Klug (1971). "Measurement and compensation of defocusing and aberrations by Fourier processing of electron micrographs". In: *Philosophical Transactions of the Royal Society of London. B, Biological Sciences* 261.837, pp. 105–118.

Adrian, Marc et al. (1984). "Cryo-electron microscopy of viruses". In: *Nature* 308.5954, pp. 32–36.

Wade, RH (1992). "A brief look at imaging and contrast transfer". In: *Ultramicroscopy* 46.1-4, pp. 145–156.

Henderson, Richard (1992). "Image contrast in high-resolution electron microscopy of biological macromolecules: TMV in ice". In: *Ultramicroscopy* 46.1-4, pp. 1–18.

Thon, F (1966). "Zur Defokussierungsabhängigkeit des Phasenkontrastes bei der elektronenmikroskopischen Abbildung". In: *Zeitschrift für Naturforschung A* 21.4, pp. 476–478.

Mindell, Joseph A and Nikolaus Grigorieff (2003). "Accurate determination of local defocus and specimen tilt in electron microscopy". In: *Journal of structural biology* 142.3, pp. 334–347.

Crewe, AV et al. (1968). "Electron gun using a field emission source". In: *Review of Scientific Instruments* 39.4, pp. 576–583.

Zhou, Zheng Hong and Wah Chiu (1993). "Prospects for using an IVEM with a FEG for imaging macromolecules towards atomic resolution". In: *Ultramicroscopy* 49.1-4, pp. 407–416.

McMullan, G., A.R. Faruqi, and R. Henderson (2016). "Chapter One - Direct Electron Detectors". In: *The Resolution Revolution: Recent Advances In cryoEM*. Ed. by R.A. Crowther. Vol. 579. Methods in Enzymology. Academic Press, pp. 1–17. DOI: https://doi.org/10.1016/bs.mie.2016.05.056. URL: https://www.sciencedirect.com/science/article/pii/S0076687916300921.

Mochel, ME and JM Mochel (1986). "A CCD imaging and analysis system for the VG HB5 STEM". In: *Proc. of the 44 th Ann. Meet. EMSA*, pp. 616–617.

McMullan, G et al. (2009). "Detective quantum efficiency of electron area detectors in electron microscopy". In: *Ultramicroscopy* 109.9, pp. 1126–1143.

Milazzo, Anna-Clare et al. (2010). "Characterization of a direct detection device imaging camera for transmission electron microscopy". In: *Ultramicroscopy* 110.7, pp. 741–744.

Bammes, Benjamin E et al. (2012). "Direct electron detection yields cryo-EM reconstructions at resolutions beyond 3/4 Nyquist frequency". In: *Journal of structural biology* 177.3, pp. 589–601.

Bai, Xiao-chen et al. (2013). "Ribosome structures to near-atomic resolution from thirty thousand cryo-EM particles". In: *elife* 2, e00461.

Li, Xueming et al. (2013). "Electron counting and beam-induced motion correction enable near-atomic-resolution single-particle cryo-EM". In: *Nature methods* 10.6, pp. 584–590.

Zhang, Kaiming et al. (2020). "Resolving individual atoms of protein complex by cryo-electron microscopy". In: *Cell research* 30.12, pp. 1136–1139.

Yip, Ka Man et al. (2020). "Atomic-resolution protein structure determination by cryo-EM". In: *Nature* 587.7832, pp. 157–161.

Markham, Roy et al. (1964). "The anatomy of the tobacco mosaic virus". In: *Virology* 22.3, pp. 342–359.

Frank, Joachim, Adriana Verschoor, and Miloslav Boublik (1981). "Computer averaging of electron micrographs of 40 S ribosomal subunits". In: *Science* 214.4527, pp. 1353–1355.

Brilot, Axel F et al. (2012). "Beam-induced motion of vitrified specimen on holey carbon film". In: *Journal of structural biology* 177.3, pp. 630–637.

Zheng, Shawn Q et al. (2017). "MotionCor2: anisotropic correction of beam-induced motion for improved cryo-electron microscopy". In: *Nature methods* 14.4, pp. 331–332.

Scheres, Sjors HW (2014). "Beam-induced motion correction for sub-megadalton cryo-EM particles". In: *elife* 3, e03665.

Rohou, Alexis and Nikolaus Grigorieff (2015). "CTFFIND4: Fast and accurate defocus estimation from electron micrographs". In: *Journal of structural biology* 192.2, pp. 216–221.

Zhang, Kai (2016). "Gctf: Real-time CTF determination and correction". In: *Journal of structural biology* 193.1, pp. 1–12.

Zhu, Yuanxin et al. (2004). "Automatic particle selection: results of a comparative study". In: *Journal of structural biology* 145.1-2, pp. 3–14.

Tang, Guang et al. (2007). "EMAN2: an extensible image processing suite for electron microscopy". In: *Journal of structural biology* 157.1, pp. 38–46.

Scheres, Sjors HW (2015). "Semi-automated selection of cryo-EM particles in RELION-1.3". In: *Journal of structural biology* 189.2, pp. 114–122.

Zivanov, Jasenko et al. (2018). "New tools for automated high-resolution cryo-EM structure determination in RELION-3". In: *eLife* 7. Ed. by Edward H Egelman and John Kuriyan, e42166. ISSN: 2050-084X. DOI: 10.7554/eLife.42166. URL: https://doi.org/10.7554/eLife.42166.

Wagner, Thorsten et al. (2019). "SPHIRE-crYOLO is a fast and accurate fully automated particle picker for cryo-EM". In: *Communications biology* 2.1, p. 218.

Bepler, Tristan et al. (2019). "Positive-unlabeled convolutional neural networks for particle picking in cryo-electron micrographs". In: *Nature methods* 16.11, pp. 1153–1160.

Tegunov, Dimitry and Patrick Cramer (2019). "Real-time cryo-electron microscopy data preprocessing with Warp". In: *Nature methods* 16.11, pp. 1146–1152.

Dhakal, Ashwin et al. (2025). "Artificial intelligence in cryo-EM protein particle picking: recent advances and remaining challenges". In: *Briefings in Bioinformatics* 26.1, bbaf011.

Scheres, Sjors HW (2012). "RELION: implementation of a Bayesian approach to cryo-EM structure determination". In: *Journal of structural biology* 180.3, pp. 519–530.

Punjani, Ali et al. (2017). "cryoSPARC: algorithms for rapid unsupervised cryo-EM structure determination". In: *Nature methods* 14.3, pp. 290–296.

De Rosier, DJ and Aaron Klug (1968). "Reconstruction of three dimensional structures from electron micrographs". In: *Nature* 217.5124, pp. 130–134.

Zhong, Ellen D et al. (2021b). "Cryodrgn2: Ab initio neural reconstruction of 3d protein structures from real cryo-em images". In: *Proceedings of the IEEE/CVF International Conference on Computer Vision*, pp. 4066–4075.

Sigworth, Fred J et al. (2010). "An introduction to maximum-likelihood methods in cryo-EM". In: *Methods in enzymology*. Vol. 482. Elsevier, pp. 263–294.

Zivanov, Jasenko, Takanori Nakane, and Sjors HW Scheres (2020). "Estimation of high-order aberrations and anisotropic magnification from cryo-EM data sets in RELION-3.1". In: *IUCrJ* 7.2, pp. 253–267.

Penczek, Pawel A (2010). "Resolution measures in molecular electron microscopy". In: *Methods in enzymology*. Vol. 482. Elsevier, pp. 73–100.

Rosenthal, Peter B and Richard Henderson (2003). "Optimal determination of particle orientation, absolute hand, and contrast loss in single-particle electron cryomicroscopy". In: *Journal of molecular biology* 333.4, pp. 721–745.

Kucukelbir, Alp, Fred J Sigworth, and Hemant D Tagare (2014). "Quantifying the local resolution of cryo-EM density maps". In: *Nature methods* 11.1, pp. 63–65.

Vilas, Jose Luis et al. (2018). “MonoRes: automatic and accurate estimation of local resolution for electron microscopy maps”. In: *Structure* 26.2, pp. 337–344.
Vilas, JL et al. (2020). “Local resolution estimates of cryoEM reconstructions”. In: *Current opinion in structural biology* 64, pp. 74–78.
Scheres, Sjors HW (2016). “Processing of structurally heterogeneous cryo-EM data in RELION”. In: *Methods in enzymology* 579, pp. 125–157.
Punjani, Ali and David J Fleet (2021). “3D variability analysis: Resolving continuous flexibility and discrete heterogeneity from single particle cryo-EM”. In: *Journal of structural biology* 213.2, p. 107702.
Zhong, Ellen D et al. (2021a). “CryoDRGN: reconstruction of heterogeneous cryo-EM structures using neural networks”. In: *Nature methods* 18.2, pp. 176–185.
Punjani, Ali and David J Fleet (2023). “3DFlex: determining structure and motion of flexible proteins from cryo-EM”. In: *Nature Methods* 20.6, pp. 860–870.
Schwab, Johannes et al. (2024). “DynaMight: estimating molecular motions with improved reconstruction from cryo-EM images”. In: *Nature Methods* 21.10, pp. 1855–1862.
Herreros, David et al. (2023). “Estimating conformational landscapes from Cryo-EM particles by 3D Zernike polynomials”. In: *Nature Communications* 14.1, p. 154.
Kelley, Lawrence A and Michael JE Sternberg (2009). “Protein structure prediction on the Web: a case study using the Phyre server”. In: *Nature protocols* 4.3, pp. 363–371.
Schwede, Torsten et al. (2003). “SWISS-MODEL: an automated protein homology-modeling server”. In: *Nucleic acids research* 31.13, pp. 3381–3385.
Jumper, John et al. (2021). “Highly accurate protein structure prediction with AlphaFold”. In: *nature* 596.7873, pp. 583–589.
Krishna, Rohith et al. (2024). “Generalized biomolecular modeling and design with RoseTTAFold All-Atom”. In: *Science* 384.6693, eadl2528.
Abramson, Josh et al. (2024). “Accurate structure prediction of biomolecular interactions with AlphaFold 3”. In: *Nature*, pp. 1–3.
Terwilliger, Thomas C et al. (2018). “A fully automatic method yielding initial models from high-resolution cryo-electron microscopy maps”. In: *Nature methods* 15.11, pp. 905–908.
He, Jiahua et al. (2022). “Model building of protein complexes from intermediate-resolution cryo-EM maps with deep learning-guided automatic assembly”. In: *Nature Communications* 13.1, p. 4066.
Jamali, Kiarash et al. (2024). “Automated model building and protein identification in cryo-EM maps”. In: *Nature* 628.8007, pp. 450–457.
Su, Baoquan et al. (2024). “Improved automated model building for cryo-EM maps using CryFold”. In: *bioRxiv*, pp. 2024–11.
Melnikov, Sergey et al. (2012). “One core, two shells: bacterial and eukaryotic ribosomes”. In: *Nature structural & molecular biology* 19.6, pp. 560–567.
Wilson, Daniel N and Jamie H Doudna Cate (2012). “The structure and function of the eukaryotic ribosome”. In: *Cold Spring Harbor perspectives in biology* 4.5, a011536.
Anger, Andreas M et al. (2013). “Structures of the human and Drosophila 80S ribosome”. In: *Nature* 497.7447, pp. 80–85.

Hariharan, Nivedita, Sumana Ghosh, and Dasaradhi Palakodeti (2023). "The story of rRNA expansion segments: finding functionality amidst diversity". In: *Wiley Interdisciplinary Reviews: RNA* 14.1, e1732.

Rodnina, Marina V (2018). "Translation in prokaryotes". In: *Cold Spring Harbor perspectives in biology* 10.9, a032664.

Merrick, William C and Graham D Pavitt (2018). "Protein synthesis initiation in eukaryotic cells". In: *Cold Spring Harbor perspectives in biology* 10.12, a033092.

Hashem, Yaser and Joachim Frank (2018). "The jigsaw puzzle of mRNA translation initiation in eukaryotes: a decade of structures unraveling the mechanics of the process". In: *Annual review of biophysics* 47.1, pp. 125–151.

Brito Querido, Jailson, Irene Díaz-López, and V Ramakrishnan (2024). "The molecular basis of translation initiation and its regulation in eukaryotes". In: *Nature Reviews Molecular Cell Biology* 25.3, pp. 168–186.

Dreher, Theo W, Olke C Uhlenbeck, and Karen S Browning (1999). "Quantitative assessment of EF-1$\alpha \cdot$ GTP binding to aminoacyl-tRNAs, aminoacyl-viral RNA, and tRNA shows close correspondence to the RNA binding properties of EF-Tu". In: *Journal of Biological Chemistry* 274.2, pp. 666–672.

Browne, Gareth J and Christopher G Proud (2002). "Regulation of peptide-chain elongation in mammalian cells". In: *European journal of biochemistry* 269.22, pp. 5360–5368.

Budkevich, Tatyana V et al. (2014). "Regulation of the mammalian elongation cycle by subunit rolling: a eukaryotic-specific ribosome rearrangement". In: *Cell* 158.1, pp. 121–131.

Ratje, Andreas H et al. (2010). "Head swivel on the ribosome facilitates translocation by means of intra-subunit tRNA hybrid sites". In: *Nature* 468.7324, pp. 713–716.

Moazed, Danesh and Harry F Noller (1989). "Intermediate states in the movement of transfer RNA in the ribosome". In: *Nature* 342.6246, pp. 142–148.

Ferguson, Angelica et al. (2015). "Functional dynamics within the human ribosome regulate the rate of active protein synthesis". In: *Molecular cell* 60.3, pp. 475–486.

Milicevic, Nemanja et al. (2024). "mRNA reading frame maintenance during eukaryotic ribosome translocation". In: *Nature* 625.7994, pp. 393–400.

Behrmann, Elmar et al. (2015). "Structural snapshots of actively translating human ribosomes". In: *Cell* 161.4, pp. 845–857.

Flis, Julia et al. (2018). "tRNA translocation by the eukaryotic 80S ribosome and the impact of GTP hydrolysis". In: *Cell reports* 25.10, pp. 2676–2688.

Hoffmann, Patrick C et al. (2022). "Structures of the eukaryotic ribosome and its translational states in situ". In: *Nature communications* 13.1, p. 7435.

Gemmer, Max et al. (2023). "Visualization of translation and protein biogenesis at the ER membrane". In: *Nature* 614.7946, pp. 160–167.

Rickgauer, J Peter et al. (2024). "Structural dynamics of human ribosomes in situ reconstructed by exhaustive high-resolution template matching". In: *Molecular Cell* 84.24, pp. 4912–4928.

Cheng, Jing et al. (2025). “Capturing eukaryotic ribosome dynamics in situ at high resolution”. In: *Nature Structural & Molecular Biology*, pp. 1–11.

Zhouravleva, G et al. (1995). “Termination of translation in eukaryotes is governed by two interacting polypeptide chain release factors, eRF1 and eRF3.” In: *The EMBO journal* 14.16, pp. 4065–4072.

Preis, Anne et al. (2014). “Cryoelectron microscopic structures of eukaryotic translation termination complexes containing eRF1-eRF3 or eRF1-ABCE1”. In: *Cell reports* 8.1, pp. 59–65.

Alkalaeva, Elena Z et al. (2006). “In vitro reconstitution of eukaryotic translation reveals cooperativity between release factors eRF1 and eRF3”. In: *Cell* 125.6, pp. 1125–1136.

Matheisl, Sarah et al. (2015). “Structure of a human translation termination complex”. In: *Nucleic acids research* 43.18, pp. 8615–8626.

Brown, Alan et al. (2015). “Structural basis for stop codon recognition in eukaryotes”. In: *Nature* 524.7566, pp. 493–496.

Pisarev, Andrey V et al. (2010). “The role of ABCE1 in eukaryotic posttermination ribosomal recycling”. In: *Molecular cell* 37.2, pp. 196–210.

Shoemaker, Christopher J and Rachel Green (2011). “Kinetic analysis reveals the ordered coupling of translation termination and ribosome recycling in yeast”. In: *Proceedings of the National Academy of Sciences* 108.51, E1392–E1398.

Young, David J et al. (2015). “Rli1/ABCE1 recycles terminating ribosomes and controls translation reinitiation in 3 ′ UTRs in vivo”. In: *Cell* 162.4, pp. 872–884.

Heuer, André et al. (2017). “Structure of the 40S–ABCE1 post-splitting complex in ribosome recycling and translation initiation”. In: *Nature structural & molecular biology* 24.5, pp. 453–460.

Kratzat, Hanna et al. (2021). “A structural inventory of native ribosomal ABCE1-43S pre-initiation complexes”. In: *The EMBO journal* 40.1, e105179.

Le Hir, Hervé et al. (2001). “The exon–exon junction complex provides a binding platform for factors involved in mRNA export and nonsense-mediated mRNA decay”. In: *The EMBO journal*.

Kashima, Isao et al. (2006). “Binding of a novel SMG-1–Upf1–eRF1–eRF3 complex (SURF) to the exon junction complex triggers Upf1 phosphorylation and nonsense-mediated mRNA decay”. In: *Genes & development* 20.3, pp. 355–367.

Chamieh, Hala et al. (2008). “NMD factors UPF2 and UPF3 bridge UPF1 to the exon junction complex and stimulate its RNA helicase activity”. In: *Nature structural & molecular biology* 15.1, pp. 85–93.

Huntzinger, Eric et al. (2008). “SMG6 is the catalytic endonuclease that cleaves mRNAs containing nonsense codons in metazoan”. In: *Rna* 14.12, pp. 2609–2617.

Loh, Belinda, Stefanie Jonas, and Elisa Izaurralde (2013). “The SMG5–SMG7 heterodimer directly recruits the CCR4–NOT deadenylase complex to mRNAs containing nonsense codons via interaction with POP2”. In: *Genes & development* 27.19, pp. 2125–2138.

Kuroha, Kazushige, Tsuyako Tatematsu, and Toshifumi Inada (2009). “Upf1 stimulates degradation of the product derived from aberrant messenger RNA containing a specific nonsense mutation by the proteasome”. In: *EMBO reports* 10.11, pp. 1265–1271.

Udy, Dylan B and Robert K Bradley (2022). "Nonsense-mediated mRNA decay uses complementary mechanisms to suppress mRNA and protein accumulation". In: *Life science alliance* 5.3.

Inglis, Alison J et al. (2023). "Coupled protein quality control during nonsense-mediated mRNA decay". In: *Journal of Cell Science* 136.10, jcs261216.

Doma, Meenakshi K and Roy Parker (2006). "Endonucleolytic cleavage of eukaryotic mRNAs with stalls in translation elongation". In: *Nature* 440.7083, pp. 561–564.

Pisareva, Vera P et al. (2011). "Dissociation by Pelota, Hbs1 and ABCE1 of mammalian vacant 80S ribosomes and stalled elongation complexes". In: *The EMBO journal* 30.9, pp. 1804–1817.

Tsuboi, Tatsuhisa et al. (2012). "Dom34: hbs1 plays a general role in quality-control systems by dissociation of a stalled ribosome at the 3′ end of aberrant mRNA". In: *Molecular cell* 46.4, pp. 518–529.

Becker, Thomas et al. (2012). "Structural basis of highly conserved ribosome recycling in eukaryotes and archaea". In: *Nature* 482.7386, pp. 501–506.

Shao, Sichen et al. (2016). "Decoding mammalian ribosome-mRNA states by translational GTPase complexes". In: *Cell* 167.5, pp. 1229–1240.

Simms, Carrie L, Liewei L Yan, and Hani S Zaher (2017). "Ribosome collision is critical for quality control during no-go decay". In: *Molecular cell* 68.2, pp. 361–373.

Sundaramoorthy, Elayanambi et al. (2017). "ZNF598 and RACK1 regulate mammalian ribosome-associated quality control function by mediating regulatory 40S ribosomal ubiquitylation". In: *Molecular cell* 65.4, pp. 751–760.

Matsuo, Yoshitaka et al. (2017). "Ubiquitination of stalled ribosome triggers ribosome-associated quality control". In: *Nature communications* 8.1, p. 159.

Juszkiewicz, Szymon et al. (2018). "ZNF598 is a quality control sensor of collided ribosomes". In: *Molecular cell* 72.3, pp. 469–481.

Garzia, Aitor et al. (2017). "The E3 ubiquitin ligase and RNA-binding protein ZNF598 orchestrates ribosome quality control of premature polyadenylated mRNAs". In: *Nature communications* 8.1, p. 16056.

Ikeuchi, Ken et al. (2019). "Collided ribosomes form a unique structural interface to induce Hel2-driven quality control pathways". In: *The EMBO journal* 38.5, e100276.

Hashimoto, Satoshi et al. (2020). "Identification of a novel trigger complex that facilitates ribosome-associated quality control in mammalian cells". In: *Scientific reports* 10.1, p. 3422.

Juszkiewicz, Szymon et al. (2020). "The ASC-1 complex disassembles collided ribosomes". In: *Molecular cell* 79.4, pp. 603–614.

Best, Katharina et al. (2023). "Structural basis for clearing of ribosome collisions by the RQT complex". In: *Nature Communications* 14.1, p. 921.

D'Orazio, Karole N et al. (2019). "The endonuclease Cue2 cleaves mRNAs at stalled ribosomes during No Go Decay". In: *Elife* 8, e49117.

Tomomatsu, Shota et al. (2023). "Two modes of Cue2-mediated mRNA cleavage with distinct substrate recognition initiate no-go decay". In: *Nucleic acids research* 51.1, pp. 253–270.

Glover, Marissa L et al. (2020). "NONU-1 encodes a conserved endonuclease required for mRNA translation surveillance". In: *Cell Reports* 30.13, pp. 4321–4331.

Burroughs, A Maxwell and L Aravind (2014). "A highly conserved family of domains related to the DNA-glycosylase fold helps predict multiple novel pathways for RNA modifications". In: *RNA biology* 11.4, pp. 360–372.

Filbeck, Sebastian et al. (2022). "Ribosome-associated quality-control mechanisms from bacteria to humans". In: *Molecular cell* 82.8, pp. 1451–1466.

Brandman, Onn et al. (2012). "A ribosome-bound quality control complex triggers degradation of nascent peptides and signals translation stress". In: *Cell* 151.5, pp. 1042–1054.

Defenouillère, Quentin et al. (2013). "Cdc48-associated complex bound to 60S particles is required for the clearance of aberrant translation products". In: *Proceedings of the National Academy of Sciences* 110.13, pp. 5046–5051.

Lyumkis, Dmitry et al. (2014). "Structural basis for translational surveillance by the large ribosomal subunit-associated protein quality control complex". In: *Proceedings of the National Academy of Sciences* 111.45, pp. 15981–15986.

Shen, Peter S et al. (2015). "Rqc2p and 60 S ribosomal subunits mediate mRNA-independent elongation of nascent chains". In: *Science* 347.6217, pp. 75–78.

Shao, Sichen et al. (2015). "Structure and assembly pathway of the ribosome quality control complex". In: *Molecular cell* 57.3, pp. 433–444.

Lytvynenko, Iryna et al. (2019). "Alanine tails signal proteolysis in bacterial ribosome-associated quality control". In: *Cell* 178.1, pp. 76–90.

Thrun, Anna et al. (2021). "Convergence of mammalian RQC and C-end rule proteolytic pathways via alanine tailing". In: *Molecular cell* 81.10, pp. 2112–2122.

Crowe-McAuliffe, Caillan et al. (2021). "Structural basis for bacterial ribosome-associated quality control by RqcH and RqcP". In: *Molecular Cell* 81.1, pp. 115–126.

Tesina, Petr et al. (2023). "Molecular basis of eIF5A-dependent CAT tailing in eukaryotic ribosome-associated quality control". In: *Molecular Cell* 83.4, pp. 607–621.

Izawa, Toshiaki et al. (2017). "Cytosolic protein Vms1 links ribosome quality control to mitochondrial and cellular homeostasis". In: *Cell* 171.4, pp. 890–903.

Kuroha, Kazushige et al. (2018). "Release of ubiquitinated and non-ubiquitinated nascent chains from stalled mammalian ribosomal complexes by ANKZF1 and Ptrh1". In: *Molecular Cell* 72.2, pp. 286–302.

Verma, Rati et al. (2018). "Vms1 and ANKZF1 peptidyl-tRNA hydrolases release nascent chains from stalled ribosomes". In: *Nature* 557.7705, pp. 446–451.

Zurita Rendón, Olga et al. (2018). "Vms1p is a release factor for the ribosome-associated quality control complex". In: *Nature Communications* 9.1, p. 2197.

Wilson, Marenda A, Stacie Meaux, and Ambro Van Hoof (2007). "A genomic screen in yeast reveals novel aspects of nonstop mRNA metabolism". In: *Genetics* 177.2, pp. 773–784.

Chu, Jessie et al. (2009). "A mouse forward genetics screen identifies LISTERIN as an E3 ubiquitin ligase involved in neurodegeneration". In: *Proceedings of the National Academy of Sciences* 106.7, pp. 2097–2103.

Bengtson, Mario H and Claudio AP Joazeiro (2010). "Role of a ribosome-associated E3 ubiquitin ligase in protein quality control". In: *nature* 467.7314, pp. 470–473.

Shao, Sichen, Karina Von der Malsburg, and Ramanujan S Hegde (2013). "Listerin-dependent nascent protein ubiquitination relies on ribosome subunit dissociation". In: *Molecular cell* 50.5, pp. 637–648.

Kostova, Kamena K et al. (2017). "CAT-tailing as a fail-safe mechanism for efficient degradation of stalled nascent polypeptides". In: *Science* 357.6349, pp. 414–417.

Defenouillère, Quentin et al. (2016). "Rqc1 and Ltn1 prevent C-terminal alanine-threonine tail (CAT-tail)-induced protein aggregation by efficient recruitment of Cdc48 on stalled 60S subunits". In: *Journal of Biological Chemistry* 291.23, pp. 12245–12253.

Verma, Rati et al. (2013). "Cdc48/p97 promotes degradation of aberrant nascent polypeptides bound to the ribosome". In: *elife* 2, e00308.

Itskanov, Samuel and Eunyong Park (2023). "Mechanism of protein translocation by the Sec61 translocon complex". In: *Cold Spring Harbor Perspectives in Biology* 15.1, a041250.

Malsburg, Karina von der, Sichen Shao, and Ramanujan S Hegde (2015). "The ribosome quality control pathway can access nascent polypeptides stalled at the Sec61 translocon". In: *Molecular biology of the cell* 26.12, pp. 2168–2180.

Veen, Annemarthe G van der and Hidde L Ploegh (2012). "Ubiquitin-like proteins". In: *Annual review of biochemistry* 81.1, pp. 323–357.

Komatsu, Masaaki et al. (2004). "A novel protein-conjugating system for Ufm1, a ubiquitin-fold modifier". In: *The EMBO journal* 23.9, pp. 1977–1986.

Kang, Sung Hwan et al. (2007). "Two novel ubiquitin-fold modifier 1 (Ufm1)-specific proteases, UfSP1 and UfSP2". In: *Journal of Biological Chemistry* 282.8, pp. 5256–5262.

Tatsumi, Kanako et al. (2010). "A novel type of E3 ligase for the Ufm1 conjugation system". In: *Journal of Biological Chemistry* 285.8, pp. 5417–5427.

Wu, Jianchun et al. (2010). "A novel C53/LZAP-interacting protein regulates stability of C53/LZAP and DDRGK domain-containing Protein 1 (DDRGK1) and modulates NF-κB signaling". In: *Journal of Biological Chemistry* 285.20, pp. 15126–15136.

Kwon, Junhye et al. (2010). "A novel LZAP-binding protein, NLBP, inhibits cell invasion". In: *Journal of Biological Chemistry* 285.16, pp. 12232–12240.

Azfer, Asim et al. (2006). "Activation of endoplasmic reticulum stress response during the development of ischemic heart disease". In: *American Journal of Physiology-Heart and Circulatory Physiology* 291.3, H1411–H1420.

Martin, Dale DO et al. (2015). "Autophagy in Huntington disease and huntingtin in autophagy". In: *Trends in neurosciences* 38.1, pp. 26–35.

Hamilton, Eline MC et al. (2017). "UFM1 founder mutation in the Roma population causes recessive variant of H-ABC". In: *Neurology* 89.17, pp. 1821–1828.

Walczak, Christopher P et al. (2019). "Ribosomal protein RPL26 is the principal target of UFMylation". In: *Proceedings of the National Academy of Sciences* 116.4, pp. 1299–1308.

Wang, Lihui et al. (2020). "UFMylation of RPL26 links translocation-associated quality control to endoplasmic reticulum protein homeostasis". In: *Cell research* 30.1, pp. 5–20.

Scavone, Francesco et al. (2023). "RPL26/uL24 UFMylation is essential for ribosome-associated quality control at the endoplasmic reticulum". In: *Proceedings of the National Academy of Sciences* 120.16, e2220340120.

Peter, Joshua J et al. (2022). "A non-canonical scaffold-type E3 ligase complex mediates protein UFMylation". In: *The EMBO Journal* 41.21, e111015.

Palade, George E (1955). "A small particulate component of the cytoplasm". In: *The Journal of biophysical and biochemical cytology* 1.1, p. 59.

Blobel, Günter and David D Sabatini (1971). "Ribosome-membrane interaction in eukaryotic cells". In: *Biomembranes: Volume 2*. Springer, pp. 193–195.

Sabatini, DD, Y Tashiro, and GE Palade (1966). "On the attachment of ribosomes to microsomal membranes". In: *Journal of molecular biology* 19.2, 503–IN9.

Borgese, Nica et al. (1974). "Ribosomal-membrane interaction: in vitro binding of ribosomes to microsomal membranes". In: *Journal of molecular biology* 88.3, pp. 559–580.

Blobel, Günter (1976). "Extraction from free ribosomes of a factor mediating ribosome detachment from rough microsomes". In: *Biochemical and biophysical research communications* 68.1, pp. 1–7.

Weis, Félix et al. (2015). "Mechanism of eIF6 release from the nascent 60S ribosomal subunit". In: *Nature structural & molecular biology* 22.11, pp. 914–919.

DaRosa, Paul A et al. (2024). "UFM1 E3 ligase promotes recycling of 60S ribosomal subunits from the ER". In: *Nature* 627.8003, pp. 445–452.

Penchev, Ivan et al. (2025). "UFMylation orchestrates spatiotemporal coordination of RQC at the ER". In: *Science Advances* 11.18, eadv0435.

McGilvray, Philip T et al. (2020). "An ER translocon for multi-pass membrane protein biogenesis". In: *Elife* 9, e56889.

Sundaram, Arunkumar et al. (2022). "Substrate-driven assembly of a translocon for multipass membrane proteins". In: *Nature* 611.7934, pp. 167–172.

Smalinskaitė, Luka et al. (2022). "Mechanism of an intramembrane chaperone for multipass membrane proteins". In: *Nature* 611.7934, pp. 161–166.

Pfeffer, Stefan et al. (2014). "Structure of the mammalian oligosaccharyl-transferase complex in the native ER protein translocon". In: *Nature communications* 5.1, p. 3072.

Cai, Yafei et al. (2015). "UFBP1, a key component of the Ufm1 conjugation system, is essential for ufmylation-mediated regulation of erythroid development". In: *PLoS genetics* 11.11, e1005643.

Lemaire, Katleen et al. (2011). "Ubiquitin fold modifier 1 (UFM1) and its target UFBP1 protect pancreatic beta cells from ER stress-induced apoptosis". In: *PloS one* 6.4, e18517.

Zhang, Yinghua et al. (2012). "Transcriptional regulation of the Ufm1 conjugation system in response to disturbance of the endoplasmic reticulum homeostasis and inhibition of vesicle trafficking". In: *PloS one* 7.11, e48587.

Hwang, Jiwon and Ling Qi (2018). "Quality control in the endoplasmic reticulum: crosstalk between ERAD and UPR pathways". In: *Trends in biochemical sciences* 43.8, pp. 593–605.

Stephani, Madlen et al. (2020). “A cross-kingdom conserved ER-phagy receptor maintains endoplasmic reticulum homeostasis during stress”. In: *elife* 9, e58396.

Ha, Byung Hak et al. (2008). “Structural basis for Ufm1 processing by UfSP1”. In: *Journal of Biological Chemistry* 283.21, pp. 14893–14900.

Ha, Byung Hak et al. (2011). “Structure of ubiquitin-fold modifier 1-specific protease UfSP2”. In: *Journal of Biological Chemistry* 286.12, pp. 10248–10257.

Millrine, David et al. (2022). “Human UFSP1 is an active protease that regulates UFM1 maturation and UFMylation”. In: *Cell Reports* 40.5.

Chen, Changchun et al. (2014). “An ER complex of ODR-4 and ODR-8/Ufm1 specific protease 2 promotes GPCR maturation by a Ufm1-independent mechanism”. In: *PLoS genetics* 10.3, e1004082.